Title
Probing the Superconducting Order Parameter of High-Tc Superconductor Bi2Sr2CaCu2O8+δ by Scanning Josephson Tunneling Microscopy

Author
Kimura, Hikari

Publication Date
2009

Peer reviewed|Thesis/dissertation

Probing the Superconducting Order Parameter of High-T_C Superconductor $Bi_2Sr_2CaCu_2O_{8+\delta}$ by Scanning Josephson Tunneling Microscopy

by

Hikari Kimura

B. S. (Keio University) 1999
M. S. (The University of Chicago) 2000

A dissertation submitted in partial satisfaction of the

requirements for the degree of

Doctor of Philosophy

in

Physics

in the

Graduate Division

of the

University of California, Berkeley

Committee in charge:

Professor Robert C. Dynes, Chair

Professor Michael F. Crommie

Professor Yuri Suzuki

Fall 2009

Probing the Superconducting Order Parameter of High-T_C Superconductor $Bi_2Sr_2CaCu_2O_{8+\delta}$ by Scanning Josephson Tunneling Microscopy

by

Hikari Kimura

Abstract

Probing the Superconducting Order Parameter of High-T_C Superconductor

$Bi_2Sr_2CaCu_2O_{8+\delta}$ by Scanning Josephson Tunneling Microscopy

by

Hikari Kimura

Doctor of Philosophy in Physics

University of California, Berkeley

Professor Robert C. Dynes, Chair

The technique of scanning tunneling microscopy (STM) with a normal metal tip has recently been used to study the high transition temperature (T_C) superconducting cuprates and has revealed many fascinating and complex features of quasiparticle excited states of these materials. For conventional superconductors, the Bardeen-Cooper-Schrieffer theory connects the pair amplitude and the superconducting gap as measured from the quasiparticle excitation spectra, while for the high-T_C materials there is still no theory to connect these quantities. We are unable to make any quantitative analysis of the superconducting ground state from the quasiparticle data.

Josephson tunneling is the tunneling of the Cooper pairs between two superconductors and the Josephson current directly relates to the superconducting pair wave function amplitude. In this thesis, we have developed the superconducting STM as a local Josephson probe and carried out direct measurements of the superconducting pair amplitude of $Bi_2Sr_2CaCu_2O_{8+\delta}$ single crystals via the *c*-axis Josephson tunneling between $Bi_2Sr_2CaCu_2O_{8+\delta}$ and a conventional superconducting STM tip. Josephson measurements at different surface locations of overdoped $Bi_2Sr_2CaCu_2O_{8+\delta}$ yield local values for the

Josephson $I_C R_N$ product, indicating an inhomogeneous structure of the $I_C R_N$ product in overdoped $Bi_2Sr_2CaCu_2O_{8+\delta}$ on a nanometer length scale. The corresponding energy gap, Δ, was also measured at the same locations and an unexpected inverse correlation is observed between the local $I_C R_N$ product and the local energy gap Δ. Our interpretation of the $I_C R_N$ vs. Δ relation with the phase fluctuation model for the phase diagram of high-T_C superconducting cuprates will be presented.

A preliminary study of the high current density effect on the density of states of $Bi_2Sr_2CaCu_2O_{8+\delta}$ will also be reported.

The effect of cleaving the $Bi_2Sr_2CaCu_2O_{8+\delta}$ surface on its electronic structure is also discussed. This is motivated by the question that the gap inhomogeneity observed by STM is intrinsic property of this material or induced by the cleaving. Since the superconducting tunneling probes the depth of a coherence length into the sample surface and $Bi_2Sr_2CaCu_2O_{8+\delta}$ has a very short *c*-axis coherence length, it's important to address this question. I will present some preliminary results of the superconducting STM studies on chemically etched $Bi_2Sr_2CaCu_2O_{8+\delta}$ surfaces.

_____

Professor Robert C. Dynes
Dissertation Chair

This dissertation is dedicated to my mother

Mari Kimura

who always encourage me through this thesis work.

Contents

List of Figures

Acknowledgments

The path to my Ph.D. is probably different from that for other Ph.D. students. Years of my Ph.D. work overlapped with the time my advisor, Bob Dynes, was UC President. Moving his lab from San Diego to Berkeley, I have met so many people in both places who assisted me and made my research and life easier through these years. It is impossible to acknowledge all of them here.

Foremost I would like to acknowledge my advisor, Bob Dynes. Bob is a great advisor providing a perfect balance between independence and guidance with me. He is so patient that he waited for me until I realized what I should do experimentally, although I scared him sometimes by my way of doing experiments. I have been very fortunate to spend my Ph.D. years with him and to see his views and dedication towards physics. It is an invaluable experience for me.

I thank Rich Barber for helping and teaching me a lot of techniques and designs for low temperature experiments through his visits to Berkeley once a week. The quenched condensed STM construction could not be completed without him. I thank Ofer Naaman for being my first mentor in the Dynes lab, instructing me how to use the low temperature STM and fabricate superconducting STM tips.

Thanks to my supplementary advisor, Mike Crommie and his group for giving me valuable advice with regard to STM. Mike served on my thesis and candidacy committees, showed me a different area of STM research, and gave me useful advice for searching postdoc positions. It was also very fun to attend his group meetings and home parties.

I thank Yoichi Ando and Shimpei Ono for growing beautiful BSCCO samples. They answered all my questions about BSCCO single crystals and high-T_C cuprates.

I thank John Clarke and his group members, Paul Reichardt and Darin Kinion for their expertise of cryogenic microwave filter design. They were very open to share their knowledge with me and have given me a lot of suggestions for low noise circuitry. I thank Harald Hess for sharing his expertise of STM and his continued interest in my research. I also thank the Berkeley machine and electronics shops, especially Dave Murai for machining most of the quench condensed STM parts. I thank other members of the Dynes group that have supported me: Louisa Bokacheva, Shane Cybart, Ke Chen, Ed Wu. I thank the Physics offices of both UC Berkeley and San Diego, especially Anne Takizawa for helping me make a smooth transition from UCSD to Berkeley until my graduation.

I acknowledge the U.S. Department of Energy for supporting my thesis work through grant No. DE-FG02-05ER46194.

Finally, I thank the members of my family. I especially acknowledge my mother Mari Kimura. She was inspired by Leo Esaki's newspaper column "From New York" and urged me to become a physicist even though I did not like physics when I was in high school. She always encouraged me and provided advice based on her career as an opera singer, and shared her life with me throughout these very challenging years. Now I really appreciate that she pushed me to come over to the U.S. for physics.

Chapter 1 Introduction

1-1 Conventional Superconductors

The first discovery of superconductivity (mercury) was by Kammerling Onnes in 1911 (Onnes1911) after his success of liquefying helium. Since then many elements and alloys have exhibited superconductivity. Superconductivity of a material is determined by observing

(i) Zero electrical resistance

(ii) Perfect diamagnetism (Meissner-Ochsenfeld effect (Meissner1933))

below the superconducting transition temperature, T_C. A phenomenological theory of superconductivity was proposed by Ginzburg and Landau in 1950 asserting the existence of a macroscopic wave function, Ψ, in terms of the complex order parameter which has a form $\Psi = |\Psi|e^{i\varphi}$ where φ is a phase of the superconducting wave function and $|\Psi|$ is the amplitude (Ginzburg1950). A big step towards construction of the microscopic mechanism of superconductors was done by Cooper who showed an instability of the ground state electron system filled up to Fermi surface provided there is an attractive interaction between electrons (Cooper1956). Not long after this Bardeen, Cooper and Schrieffer (BCS) constructed a complete microscopic theory of superconductors in 1957 (BCS1957) for which they won the Nobel prize in Physics. The BCS theory describes that below T_C, electrons pair to form bound states (Cooper pairs) via the electron-phonon coupling and then condense into a ground state formed on the Fermi surface in a width of the superconducting energy gap, $2\Delta_{BCS}$. This ground state is described by a single wave

function Ψ whose amplitude is proportional to the superconducting energy gap, Δ_{BCS} and $2\Delta_{BCS}$ is equivalent to an energy to break up the pairs. Conventional superconductors are materials whose superconductivity is explained by the BCS theory and the superconducting phase φ in the order parameter is independent of the position on the Fermi surface. In other words, the order parameter has a rotational symmetry (*s* symmetry) in momentum (k) - space shown in Figure 1–1 (a) and is called an *s*-wave state.

1-2 Unconventional Superconductors

Copper oxide superconductors, originally discovered by Bednorz and Müller in 1986 (Bednorz1986) had a huge impact on the science community in that (i) the parent compounds are antiferromagnetic Mott insulators in which the electrons are localized due to strong electron-electron Coulomb repulsion, (ii) high transition temperature (high-T_C) superconductivity is created by doping this insulator with charge carriers and (iii) high-T_C superconductors are quasi-two dimensional systems of layers of CuO_2 in which CuO_2 planes are conducting and the pairing is formed in the plane (Dynes1994, Orenstein2000). An empirical relation between T_C and doped hole concentration, δ_h, is observed to be $T_C/T_C(\mathrm{Max}) = 1 - 82.6(\delta_h - 0.16)^2$ for Lanthanum (La), Bismuth (Bi) and Thallium (Tl) compound cuprates (Presland1991).

High-T_C superconducting cuprates are regarded as “unconventional” since the symmetry of the superconducting order parameter of these materials is not simple *s*-wave so that their superconducting properties do not have the form predicted by the BCS theory. Some experiments (Wollman1993, Tsuei1994) were performed to determine the

symmetry of the order parameter, and supported the proposal that the order parameter of high-T_C superconducting cuprates has d_{x2-y2}-wave symmetry. It was believed that this resulted from anitferromagnetic spin fluctuations (Monthoux1991), although observations of other groups clearly showed the symmetry of high-T_C superconducting cuprates is not pure d_{x2-y2}-wave (Sun1994a, Mößle1999). With d_{x2-y2}-wave symmetry, the order parameter changes sign through a 90° rotation and becomes zero along the diagonal (node) while it becomes maximum or minimum along k_X or k_Y direction (antinode). For Bi cuprates compound, the antinodal direction is parallel to Cu - O bond which is 45° from the crystallographic a(b)-axis (Figure 1-1(b)), while La, Y (Yttrium) and Nd (Neodymium) compounds, the lobe is along the a(b)-axis. Early tunneling studies of Pb/insulator/$YBa_2Cu_3O_{7-\delta}$ planar junctions showed the quasiparticle density of states with coherence peaks and large zero bias conductance (Valles1991). Also identified was the possible indication of electron-phonon coupling in the dI/dV spectrum of $YBa_2Cu_3O_{7-\delta}$ although the calculated T_C was much lower than the measured transport T_C (Dynes1992). Angle-resolved photoemission spectroscopy (ARPES) has shown the anisotropy of the energy gap Δ, *i.e.*,

$$\Delta(k) \sim \Delta_0 \left[\cos(k_x a) - \cos(k_y a)\right] \tag{1-1}$$

where a is the lattice constant of CuO_2 plane (Ding1996a). Along the node directions quasiparticles can be excited with infinitesimally small energy, leading to a power law dependence of physical quantities such as penetration depth (Hardy1993). This is in contrast to conventional superconductors where the energy gap develops over all of the

Fermi surface so that the quasiparticle is activated above the gap and the physical quantity has exponential dependence of temperature as T goes to zero.

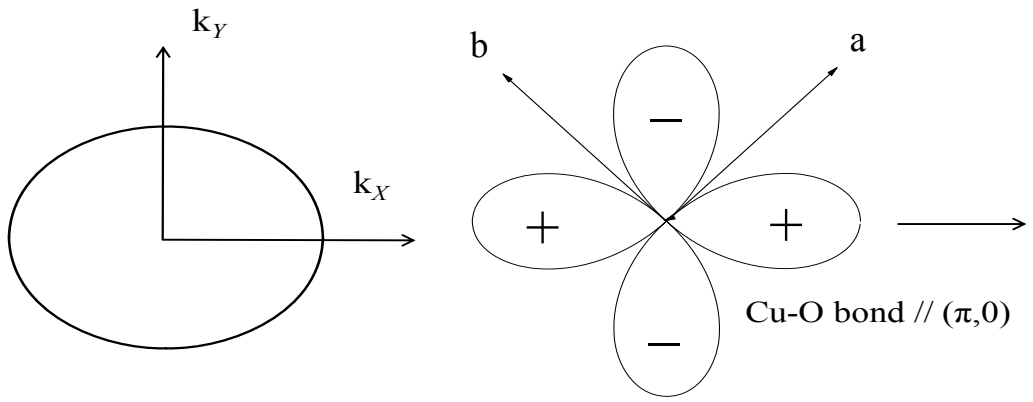

(a) *s*-wave order parameter

(b) d_{x2-y2} -wave order parameter for Bi-, Tl-, Hg- and Y- compounds

Figure 1-1 (a) Order parameter of conventional (*s*-wave) superconductors. (b) Order parameter with d_{x2-y2}-wave symmetry. Cu-O bond is parallel with (π,0) and 45° from the crystallographic *a*(*b*)-axis for $Bi_2Sr_2CaCu_2O_{8+\delta}$.

Other tests to examine the pairing symmetry are related to the effects of elastic scattering on superconductivity in the cuprates. In the *s*-wave superconductors where impurity scattering has a small effect on T_C (Anderson1959), it is observed that anisotropy of the energy gap is reduced as the elastic scattering rate, τ_E increases in many samples, for example, Pb_xBi_{1-x} (Campbell1966). On the other hand, the average energy gap Δ_{AVE} in the d_{x2-y2}-wave superconductors is zero all the time due to the pairing symmetry on the time scale of $\tau_E\Delta_{AVE} \sim \hbar$ (Radtke1993, Dynes1994). It was experimentally observed that impurity scattering did suppress T_C and the superconducting density of states with sharp quasiparticle coherence peaks in ion-damaged $YBa_2Cu_3O_{7-\delta}$

(Valles1989a) and Pr substituted $Y_{1-x}Pr_xBa_2Cu_3O_{7-\delta}$ (Sun1994b). T_C dependence on the residual resistivity, however, was much weaker than those expected from the pure d_{x2-y2}-wave symmetry in these samples. The effect of impurity scattering on the atomic scale in $Bi_2Sr_2CaCu_2O_{8+\delta}$ was also studied using a scanning tunneling microscope (STM) and showed the disappearance of sharp quasiparticle coherence peaks in the local density of states around an impurity (Yazdani1999, Hudson1999). Also the appearance of the impurity-induced bound states at the Fermi energy at the nonmagnetic impurity site suggested d_{x2-y2}-wave symmetry in $Bi_2Sr_2CaCu_2O_{8+\delta}$ (Yazdani1999, Hudson1999, Pan2000a).

Another property of the cuprates, a large gap in the normal state ($T > T_C$), the so-called pseudogap, was found in the antinodal region in underdoped materials by ARPES (Ding1996b) and by STM (Renner1998a). Although the origin of the pseudogap is still debated (Tallon2001, Hufner2008), recent ARPES measurements clearly observed two distinct energy gaps in different momentum directions, one closing at T_C in the nodal direction and another remaining finite above T_C along the antinodal direction (Lee2007). The latter is expected to relate to the pseudogap.

The STM with a normal metal tip has been utilized for nanometer scale studies of electronic structures on the surface of high-T_C superconducting cuprates, especially $Bi_2Sr_2CaCu_2O_{8-\delta}$, revealing electronic and structural inhomogeneities (Pan01, Howald2001, Lang2002). It is suspected that inhomogeneities will play a key role in understanding this strongly correlated electron system.

1-3 Disordered metallic thin film

Thermal evaporation of metals onto a cold substrate, (quenched condensed deposition), can grow disordered metallic thin films which show a 2-dimensional superconductor-insulator transition as the film thickness is changed (Dynes1978a). In spite of the tremendous amount of past work in this field, there still remain many questions regarding the nature of this transition (Goldman1998). A beauty of the quenched deposition technique is that we can achieve two distinct forms of this transition by slightly different deposition methods. The superconducting pair wave function is described as the complex order parameter, $\Psi = |\Psi|e^{i\varphi}$ as mentioned above and its superconductivity can be destroyed either by suppressing the amplitude $|\Psi|$ to zero (amplitude dominated regime) or by increasing the phase fluctuations to diminish long range phase coherence over a macroscopic distance (phase fluctuation dominated regime). Experimentally, the amplitude dominated regime is accessible by growing a uniform thickness film a few atomic layers thick onto a substrate with a pre-deposited seed layer. In this configuration the amplitude approaches zero as the film thickness is decreased (Valles1989b, Valles1992). On the other hand, the growth of a granular film corresponds to the phase fluctuation dominated region. In this case each grain of the film clearly shows superconductivity, but there is no phase coherence between the grains (Barber1994).

These configurations manifest two distinct superconductor-insulator transitions. In a granular film in which each grain has robust superconductivity, increasing the "average" film thickness results in more inter-granular coupling so that phase coherence length becomes less susceptible to phase fluctuations. This yields a rise of the T_C of the film with $R_{\square}$ (sheet resistance of the film) reduction, while the amplitude of each grain

remains unchanged through the superconductor-insulator transition. This occurs near $R_{\square} \approx h/4e^2 = 6.45$ kΩ where h is Planck's constant. Further increase of the film thickness reveals the competition between the phase locking and the phase fluctuations resulting in resistive tails below T_C. With more deposition the length scale of the phase coherence exceeds the film size and the phase is completely locked, yielding the highest T_C in this system. In the uniform film case, however, T_C is well defined (it has a sharper transition than granular film), and the superconducting amplitude (Δ) continuously decreases while keeping $2\Delta/k_B T_C$ constant as the film thickness is decreased (Valles1989b), indicating a quantum phase transition at $T_C \rightarrow 0$.

Combining these two distinct superconductor-insulator transitions in a single system, a phase diagram of T_C vs. film thickness is very analogous to the T_C vs. δ_h (doping concentration) phase diagram of high-T_C superconducting cuprates (Merchant2001) except for an ambiguity of the T_C determination in the intermediate region of granular films. These authors used the insulating granular Pb film followed by Ag deposition as a model system. It is useful to introduce two temperature scales determining T_C, T_θ^{max} and T_{MF}. T_θ^{max} is the phase fluctuation limiting T_C and T_{MF} is the amplitude limiting mean field T_C. Even in the insulating Pb film, each individual grain becomes superconducting near the T_C of bulk Pb while the film is an insulator, reminiscent of the pseudogap state which appears in the underdoped region of high-T_C superconducting cuprates and is observed as low energy excitations in the quasiparticle spectra. The deposition of Ag simply enhances the conductance of the film (decreasing $R_{\square}$), and strengthens the inter-granular coupling via superconductor/normal metal/superconductor junctions, resulting in a T_C increase (T_θ^{max} is an upper bound to T_C

in the fluctuation dominated regime). Further deposition of Ag, however, makes Δ and T_C reduce due to the proximity effect of the Ag on the Pb in the Cooper limit (Cooper1961). The pairing interaction of the Pb/Ag layer becomes smaller as the Ag thickness is increased (Deutscher69), resulting in T_C reduction, analogous to the overdoped region in the high-T_C cuprate systems (T_{MF} is an upper bound to T_C in the amplitude dominated regime). The maximum T_C is achieved in the crossover region between T_θ^{max} and T_{MF}.

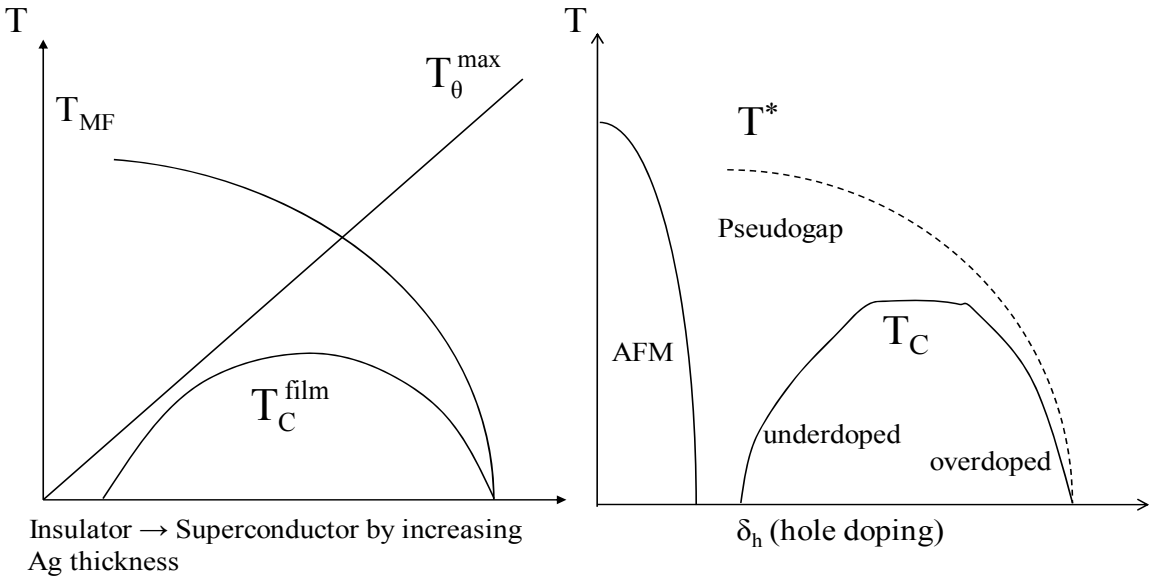

(a) 2-dimensional Superconductor-Insulator transition in granular Pb/Ag bilayer films

(b) High-T_C superconductor phase diagram

Figure 1-2 Phase diagrams of two different strongly correlated electron systems. (a) Phase diagram of the 2-dimensional disordered film. Tuning parameter of the insulator-superconductor transition is the Ag thickness. See the text for definitions of T_θ^{max} and T_{MF}. (b) Phase diagram of high-T_C superconducting cuprates. Tuning parameter is the hole doping, δ_h. AFM stands for antiferromagnetic insulator. T^* is the pseudogap temperature.

The similarity between these two strongly correlated electron systems is schematically shown in Figure 1-2. It is intriguing to ask (i) whether the pseudogap state of the underdoped regime of the high-T_C superconducting cuprates is similar to the

insulating side of the Pb/Ag granular film and (ii) whether the superconducting energy gap Δ and the amplitude of the superconducting pair amplitude $|\Psi|$ decrease continuously in ultrathin uniform film toward the superconductor-insulator transition. Construction of a new type of STM with a capability of quenched condensed deposition is described in a subsequent chapter and the experiment proposed there is intended on the basis of this similarity between these two systems.

1-4 Motivation of this Thesis work

High-T_C superconducting cuprates and highly disordered metallic thin films near the metal-insulator transition are both strongly correlated electron systems and share some similarities in their superconducting properties as pointed out in the previous section. Because of the inhomogeneities in both systems, STM as an atomic-scale resolution probe is expected to be a very powerful tool to study these systems.

The ability of STM, invented by Binnig and Rohrer (Binnig1982), was demonstrated by solving a long time problem of the 7×7 reconstruction on the Si(111) surface (Binnig1983). Later the STM was developed to manipulate Xe atoms on metallic surface (Eigler1990), and visualize the interference pattern of surface electron waves (Crommie1993a, Crommie1993b). Scanning tunneling spectroscopy (STS) as a local spectroscopic probe was utilized to directly image the Abrikosov flux lattices and observe the quasiparticle bound states inside vortex cores in $NbSe_2$ (Hess1989, Hess1990a).

During the past decade, STM/STS has been extensively used to study microscopic electronic structures of high-T_C superconducting cuprates, $YBa_2Cu_3O_{7-\delta}$ (YBCO) and $Bi_2Sr_2CaCu_2O_{8+\delta}$ (BSCCO) in both the superconducting and normal state. Vortex flux

lines were first imaged in YBCO (Maggio-Aprile1995) and in BSCCO later (Renner1998b, Pan2000b). Mapping of the integrated local density of states (LDOS) and the "gap" taken from the difference between two coherence peaks showed nanometer-scale inhomogeneities in BSCCO single crystals (Pan2001, Howald2001 and Lang2002) and in disordered BSCCO thin films (Cren2000). Moreover the Fourier-transform of the LDOS maps revealed periodic electronic structure along the Cu-O bond directions in the superconducting state (Hoffman2002b, Howald2003), inside vortex cores (Hoffman2002a) and even at temperatures above T_C where no long range phase coherence exists (Vershinin04). Further sophistication of STM instrumentation has made it possible to keep tracking the same region of the surface for "Gap map" determinations while increasing the temperature through T_C without losing atomic-scale registry. It is revealed that (i) the formation of gapped regions obtained from the dI/dV spectra actually started above T_C and there is a linear relation between Δ and the gap opening temperature, T^* (Gomes2007) and (ii) anticorrelation between the energy gap, Δ in the superconducting state and the normal state conductance at the Fermi energy (Pasupathy2008) in various dopings of BSCCO. Through their STM experiments, the measured dI/dV spectral lines were fitted with the d_{x2-y2}-wave pairing density of states (Gomes2007, Alldredge2008). The identification of Δ, however, becomes ambiguous in heavily underdoped BSCCO where the observed dI/dV curves no longer have well defined sharp coherence peaks (McElroy2005a, Alldredge2008). Two important issues raised by these complex results are (i) whether the superconducting order parameter of BSCCO has spatial variation, and (ii) how the superconducting ground state correlates with the quasiparticle excited states (Δ). Normal-metal STM studies reveal only the

quasiparticle excitation spectrum. These uncertainties motivated the subject of this thesis: a direct probe of the superconducting pair wave function using the Josephson effect (Josephson1962).

Josephson tunneling is Cooper pair tunneling between two superconductors separated by a thin barrier. The zero-voltage current flowing through the junction is given by $I = I_C \sin(\varphi_2 - \varphi_1)$, where I_C is the maximum supercurrent at zero temperature and $\varphi_{1(2)}$ is the phase of two superconducting electrodes. The maximum supercurrent is related to the amplitude of the superconducting pair wave function. An STM with a superconducting tip can be a local Josephson probe and can, in principle, access the superconducting pair wave function directly on a length scale smaller than or comparable to the superconducting coherence length, ξ.

Between conventional superconductors the Josephson $I_C R_N$ product (R_N is the normal state resistance of the junction) is a directly measurable quantity uniquely determined by the specific materials in the Josephson junction. This parameter, $I_C R_N$ is directly linked to both the superconducting order parameter amplitude and the energy gaps Δ_{BCS} of the superconductors through the BCS relationship. Josephson studies using a superconducting STM on the conventional superconductors have shown good agreement between the measured $I_C R_N$ and BCS theory (Naaman2001b, Naama2003). For high-T_C superconductors, on the other hand, there is no established theory to relate $I_C R_N$ with Δ derived from the quasiparticle excitation spectrum. An $I_C R_N$ measurement on BSCCO using a superconducting STM should, however, both prove the existence and yield the amplitude of the BSCCO pair wave function that couples to the conventional superconducting tip. Because of the spatial resolution of an STM, this measurement

could reveal useful new information regarding inhomogeneities in the superconductivity of BSCCO.

1-5 Organization of this Thesis

In this thesis, I will report on superconducting STM studies of BSCCO single crystals and describe what we learn about the superconducting pair wave function of BSCCO and how it reveals new physics about the superconducting cuprates that cannot be investigated by normal STM studies.

In chapter 2, I will give a brief theoretical and experimental background to understand this thesis work, electron tunneling and STM operation. I will then describe how to fabricate the superconducting STM tip which is made of Pb and Ag deposition onto Pt/Ir wire. A description of the importance of a cryogenic microwave filter and its design will be made. Since the STM is a local probe with atomic resolution, the resulting Josephson junction formed between the tip and the sample is an ultra-small Josephson junction with relatively high normal junction resistance. Thermal fluctuation effects on the ultra-small Josephson junction are explained with introduction of two parameters intrinsic to the junction, noise temperature, T_n, and environmental impedance, Z_{ENV}. Results of Pb/insulator/Pb (Pb/I/Pb) STM Josephson junctions are presented to demonstrate that we really observe the Josephson current in the fluctuation regime and how to determine T_n and Z_{ENV} using the phase diffusion model. Then I will talk about the observed data from Pb/I/$NbSe_2$ STM Josephson junctions to derive the I_CR_N product of $NbSe_2$ single crystal/Pb Josephson junction. If the high-T_C superconducting cuprates have d_{x2-y2}-wave symmetry, *c*-axis Josephson tunneling between *s*-wave and d_{x2-y2}-wave

superconductors should be zero because the matrix element between *s*-wave and d_{x2-y2}-wave symmetries will be zero. Nevertheless *c*-axis Josephson coupling was observed in Pb/I/YBCO (Sun1994a) and Pb (Nb)/I/BSCCO planar tunnel junctions (Mößle1999, Kawayama1999). I will review these previous results briefly.

In chapter 3, the local measurements of *c*-axis Josephson tunneling on optimally-doped and overdoped BSCCO single crystals are presented and show the spatial dependence of the $I_C R_N$ product and the energy gap Δ. A central result in this thesis is the inverse relation between $I_C R_N$ and Δ, which is consistent with Emery-Kivelson model for the phase diagram of high-T_C superconductors (Emery1995). All the data of the $I_C R_N$ products for BSCCO were obtained on cleaved surfaces of BSCCO. The effect of the cleaving on the surface electronic structure has not been investigated. I present preliminary result of superconducting STM study of chemically etched BSCCO single crystals.

In chapter 4, future projects based on the findings in this thesis work will be discussed. One future direction is local Josephson measurements on underdoped BSCCO single crystals to investigate how spatially the superconducting pair amplitudes vary and whether they correlate with the energy gaps as predicted by Emery-Kivelson model and our results (Kimura2008). Another future direction is local Josephson studies of metallic particles deposited onto BSCCO to see if the superconducting pair wave function induced in these particles from BSCCO via the proximity effect can be detected by superconducting STM and what it looks like. Furthermore we propose microscopic study of superconductor-insulator transition summarized in section 1-3. Unification of the quench condensed deposition technique and the superconducting STM is designed

and we have finished building a new kind of STM to accomplish this. I will show schematics of the quench condensed STM and talk about what we want to do using this microscope.

Chapter 2 Experimental Backgrounds

2-1 Electron Tunneling and Scanning Tunneling Microscope

The basis of my thesis work is concentrated on the works of Leo Esaki, Ivar Giaever and Brian Josephson sharing the Nobel Prize in Physics in 1973 for the first observations of electron tunneling in solids (Esaki1969, Giaever1969) and a theoretical prediction of Cooper pair tunneling (Josephson1962). Electron tunneling through an insulating barrier (or vacuum) results from the quantum mechanical nature of the electron wave function. Figure 2-1 shows a schematic of energy states of two electrodes separated by a potential barrier with a finite height. An electron wave function in the left electrode is exponentially decaying inside the barrier and transmits into the right electrode and *vice visa*. The barrier transmission probability $|t|^2$, defined as the ratio of the transmitted current j_T to the incident current j_I can be computed simply from solving the Schrödinger equation with matching condition of the wave functions and has a form

$$|t|^2 \equiv j_T/j_I \sim exp\left[-2\frac{\sqrt{2m\Phi}}{\hbar}s\right] = exp[-2\kappa s] \tag{2-1}$$

where m is mass of the electron, s the barrier width, $\hbar$ Planck's constant and Φ the integrated barrier height due to the insulator (vacuum) which is the required energy to remove an electron from a metal. For typical metal-vacuum-metal junctions, Φ may be of the order of a few electron volts (eV) while the applied voltage V is typically the order of

mVs up to fractions of a volt. κ is called the decay constant. Using eV as the unit of the work function and $Å^{-1}$ as the unit of the decay constant,

$$\kappa = 0.51\sqrt{\Phi[\mathrm{eV}]}\ [Å^{-1}] \tag{2-2}$$

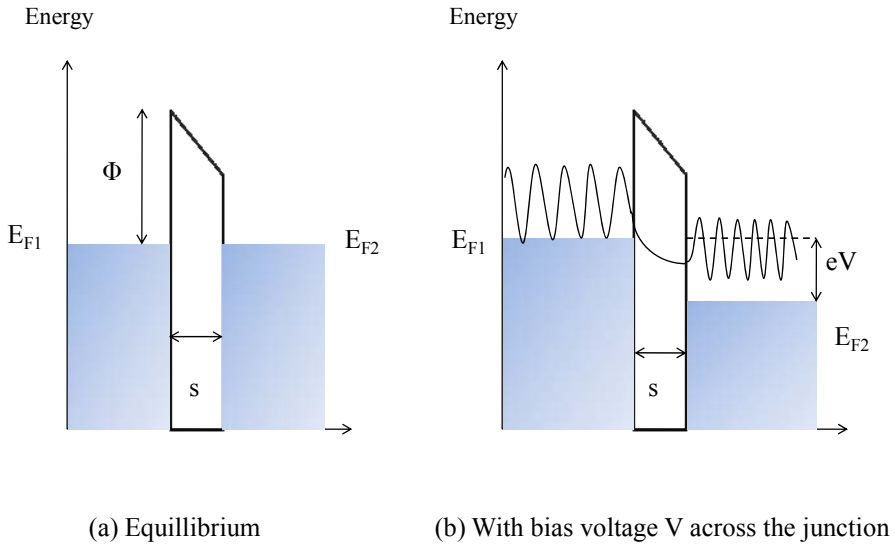

(a) Equillibrium (b) With bias voltage V across the junction

Figure 2-1 Electron tunneling through a barrier

A scanning tunneling microscope (STM) is simply a tunnel junction formed between two electrodes (a metallic tip and a sample) separated by several Angstroms of vacuum (Chen Book). By applying the bias voltage between the electrodes, a tunneling current can flow through the vacuum. I will use the tip and the sample as the two electrodes in a tunnel junction in the following discussion.

For a typical tunnel junction, the barrier transmission probability is around 10^{-6} ~ 10^{-10}. This led Bardeen to introduce an effective Hamiltonian for the tunneling (Bardeen1961). He regarded two electrodes forming the tunnel junction as two free

subsystems, which lightly overlap each other and the tunneling interaction can be treated as a perturbation due to the exponential decay in the barrier. He showed that the probability of electron transfer between the two electrodes depends on the tunneling matrix element $\boldsymbol{T}$, determined by overlap of the wave functions of two subsystems in the weak tunneling regime ($|\boldsymbol{T}|^2 << 1$). In this approximation, the total Hamiltonian describing the system is

$$H = H_A + H_B + H_T \tag{2-3}$$

where $H_{A(B)}$ is the full many-body Hamiltonian for the isolated system A (B), H_T, a one-body coupling term which transfers a single electron between A and B.

$$H_T = \sum_{p,k} \boldsymbol{T}_{pk}(C_{p\uparrow}^{+} C_{k\uparrow} + C_{-k\downarrow}^{+} C_{-p\downarrow}) + H.C. \tag{2-4}$$

where $C_{p\uparrow}^{+}$ ($C_{-p\downarrow}$) are the creation (annihilation) operators for the Bloch state p with spin index $\uparrow(\downarrow)$ in A and similarly for the Bloch state k in B. *H.C.* is the Hermitian conjugate. $\boldsymbol{T}_{pk}$ is the tunneling matrix element between the states p and k (Cohen1962).

Bardeen showed the tunneling probability w for tunneling from the state p to the state k is calculated by the Fermi's golden rule, yielding

$$w_{p\to k} = \frac{2\pi}{\hbar} \left|T_{pk}\right|^2 D(E_k) f_p (1 - f_k) \tag{2-5}$$

and similarly for that from the state k to the state p,

$$w_{k\to p} = \frac{2\pi}{\hbar}\left|T_{kp}\right|^2 D\left(E_p\right) f_k(1-f_p) \tag{2-6}$$

where $D(E_{p(k)})$ is the density of states of the state p and k, $f_{p(k)}$ is the Fermi distribution function of the state p and k, respectively: $f_{p(k)} = f\left(E_{p(k)}\right) = \left[1 + exp\left(E_{p(k)}/k_B T\right)\right]^{-1}$ and k_B is the Boltzmann constant.

For electron tunneling when energy is conserved (elastic tunneling) and with a bias voltage V at temperature T (Figure 2-2(a)), the tunneling current can be given by a summation of the electrons tunneling from the tip to the sample and the sample to the tip with the tunneling probability:

$$\begin{aligned} I &= \frac{4\pi e}{\hbar}\int_{-\infty}^{\infty} |\boldsymbol{T}|^2\, D_s(E-eV) D_t(E)\left\{f(E-eV)\left(1-f(E)\right) - f(E)\left(1-f(E-eV)\right)\right\}\mathrm{d}E \\ &= \frac{4\pi e}{\hbar}\int_{-\infty}^{\infty} |\boldsymbol{T}|^2\, D_s(E-eV) D_t(E)\{f(E-eV) - f(E)\}\mathrm{d}E \end{aligned} \tag{2-7}$$

where e is the electron charge, $D_{s(t)}$ stands for the density of states of the sample (the tip). The energy E is measured from the Fermi energy for both tip and sample. Thus the tunneling current depends on the convolution of the density of states of both the tip and the sample. It is also assumed that the tunneling matrix element does not depend on energy for the low energy (voltage) applied to the junction. Thus $|\boldsymbol{T}|^2$ can be taken outside of the integral and treated as a constant.

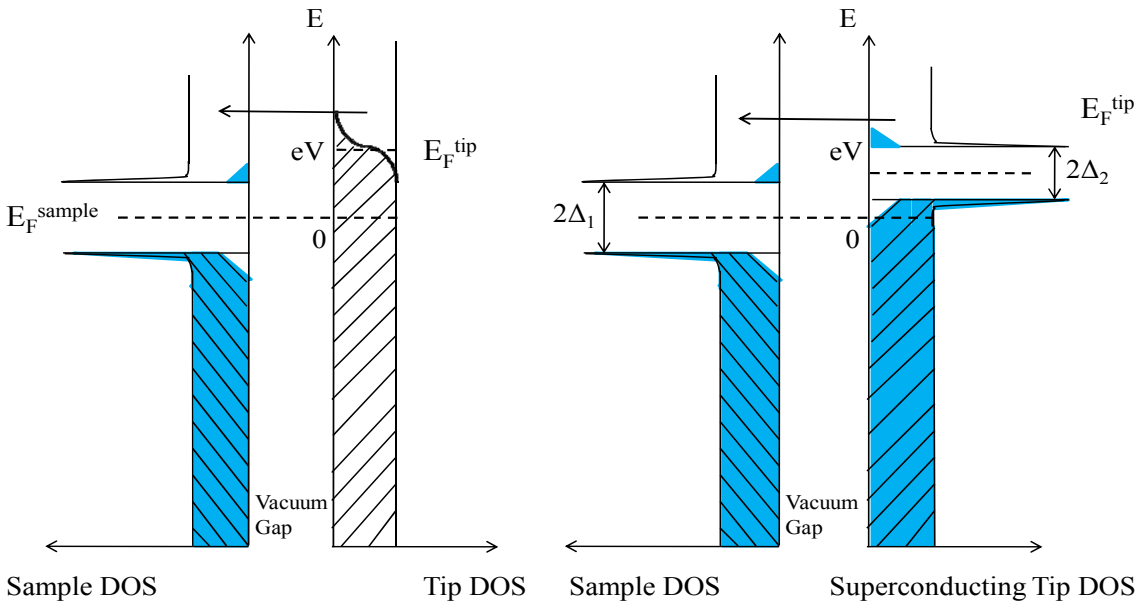

(a) Superconductor-vacuum-Normal metal (b) Superconductor-vacuum-Superconductor

Figure 2-2 (a) Electron tunneling from a metallic tip to a superconducting sample at a finite temperature T. A positive bias voltage is applied to the sample so that the Fermi level of the sample is lowered by eV with respect to that of the tip. Density of states for the metallic electrode is filled up to the Fermi level with thermal broadening of $2k_BT$. Some quasiparticles on the superconductor are thermally excited above the Fermi energy. In this configuration, electrons tunnel from the tip side to the sample side. (b) Electron tunneling between a superconducting tip and a superconducting sample.

So now let us think about what the difference between the barrier transmission probability $|t|^2$ and the tunneling matrix element $|\boldsymbol{T}|^2$ is. For the simple square barrier potential, we can explicitly compute both $|t|^2$ and $|\boldsymbol{T}|^2$, showing that $\left|\boldsymbol{T}_{pk}\right|^2 D(E_k)D(E_p) = |t|^2/4\pi$ (Kane1969). In general for the slowly changing barrier potential, we need to use the WKB approximation for the wave functions in the classically forbidden region, but it still gives the same barrier penetration factor (the exponentially decaying term),

$$\left|\boldsymbol{T}_{pk}\right|^2 D(E_k)D(E_p) \rightarrow \exp\left(-2\int dx \frac{\sqrt{2m(V(x)-E)}}{\hbar}\right) \sim exp[-2\kappa s] \qquad (2\text{-}8)$$

In fact, the barrier transmission probability $|t|^2$ is the dimensionless number, while the tunneling matrix element $|\boldsymbol{T}|^2$ has the dimension of energy and its physical meaning is the energy lowering due to the overlap of two wave functions of the electrodes (Chen Book). Thus this relation of (2-8) gives the exponential dependence of the tunneling current on the tip-sample distance *s*,

$$I \propto \frac{4\pi e}{\hbar} e^{-2\kappa s} \int_{-\infty}^{\infty} D_s\,(E-eV) D_t(E)\{f(E-eV)-f(E)\}\mathrm{d}E \qquad (2\text{-}9)$$

Now I describe the basic operation modes of the STM.

(i) Constant current topography

The most common mode for an STM to image the sample surface is that of constant current topography. As shown in Figure 2-3, the feedback circuit maintains a constant tunnel current during which the tip is raster scanning the surface driven by the scanner. Because of the very high (exponential) sensitivity to the tip-sample distance of the tunnel current, the feedback signal for the *z* component of the scan piezo taken at each pixel reflects surface corrugation, yielding an atomic resolution image.

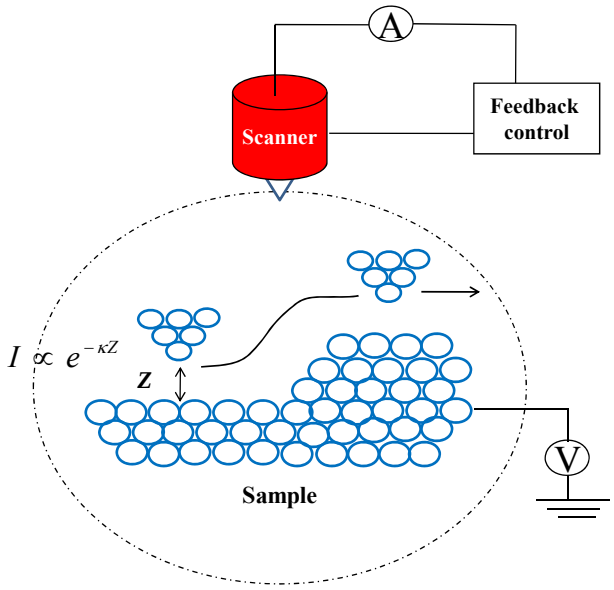

Figure 2-3 Schematic of STM operated in constant current mode

(ii) Scanning tunneling spectroscopy

Local spectroscopic measurements can be done by turning off the feedback loop so that the tip-sample distance is fixed and then measuring the tunnel current-voltage characteristics. If we use a metallic tip and assume a constant density of states, the differential tunneling conductance, $G(V) = dI/dV|_V$ is calculated by differentiating the equation (2-9) with respect to V,

$$\frac{dI}{dV}(V,\vec{r}) \propto D_t(0)\int_{-\infty}^{\infty} D_s(E)\frac{df(E-eV)}{dV}dE \qquad (2\text{-}10)$$

All the spectroscopic measurements reported in this thesis were performed at the experimental base temperature, T = 2.1 K. At finite temperature, $df(E-eV)/dV$ shows

a peak centered at eV with a width ~ 4 k_BT and this smears any feature observed by the tunneling spectroscopy[1]. As T goes to zero, $df(E-eV)/dV$ approaches the δ-function, and the equation (2-10) becomes

$$G(V,\vec{r})|_{T=0} = \frac{dI}{dV}(V,\vec{r})|_{T=0} \propto D_s(eV,\vec{r}) \tag{2-11}$$

indicating that the differential conductance is directly proportional to the sample's density of states at $E = eV$.

A low frequency ac method using a lock-in amplifier is commonly used to measure dI/dV. It is accomplished by modulating the bias voltage V by $\delta V \cos \omega t$, where ω is much higher than the bias sweep rate, and then measuring the resulting modulation current:

$$I(V + \delta V \cos \omega t) \approx I(V) + \left.\frac{dI}{dV}\right|_V \delta V \cos \omega t \tag{2-12}$$

The spectroscopic mode is also used for measuring the tunnel current as a function of tip-sample separation, s to check the exponential dependence of I on s (equation 2-9). In this case a small ac modulation is applied to the z piezoelectric to vary the tip-sample distance. Using equation (2-9), the work function Φ for the sample surface is measured from the tunneling current as a function of tip-sample distance,

[1] For a tunnel junction consisting of two normal metal electrodes, a width of the thermal broadening is 5.4 k_BT.

$$\Phi[\mathrm{eV}] = \frac{\hbar^2}{8m}\left(\frac{d\ln I}{ds}\right)^2 = 0.95\left(\frac{d\ln I}{ds[\text{Å}]}\right)^2 \tag{2-13}$$

if the tunnel junction is a clean vacuum junction. In other words, we can check the quality of the tunnel junction by plotting I as a function of s in a log-linear plot, where the current must be linear because of its exponential dependence of s. A typical value for the work function of a metallic surface is a few eVs so that only 1 Å increase of tip-sample separation causes a decrease of tunnel current by a factor of $e^2 \approx 7.4$.

(iii) Superconductive tunneling

The superconducting density of states for conventional superconductors is given by the BCS theory in the weak coupling limit as follows

$$D_{SC}(E) = D_N(0)\,\mathrm{Re}\left(\frac{|E|}{\sqrt{E^2 - \Delta^2}}\right) \tag{2-14}$$

where $D_N(0)$ is the normal state density of states at the Fermi energy, Δ the superconducting energy gap and $\mathrm{Re}(x)$ denotes the real part of x. (Tinkham Book). When a superconducting sample is scanned by a normal metal tip, the measured dI/dV spectrum is proportional to the superconducting density of states of the sample with a thermally broadening width ~ 2 k_BT at $E = eV$ as seen from the equation (2-10).

The density of states for conventional superconductors measured from dI/dV spectra showed excellent fits to the BCS form of the density of states using a broadening

term, Γ originally introduced by Dynes *et al*. to describe the quasiparticle lifetime broadening (Dynes1978a).

$$D_{SC}(E) = D_N(0)\mathrm{Re}\left(\frac{|E - i\Gamma|}{\sqrt{(E - i\Gamma)^2 - \Delta^2}}\right) \tag{2-15}$$

In fact, we can estimate the tunnel junction temperature by substituting this fitting form into the equation (2-9),

$$I(V, \vec{r}) \propto \mathrm{Re}\int_{-\infty}^{\infty}\left(\frac{|E - i\Gamma|}{\sqrt{(E - i\Gamma)^2 - \Delta^2}}\right)\{f(E - eV) - f(E)\}dE \tag{2-16}$$

We confirmed that it is very close to the sample temperature measured by a thermometer attached to the sample holder.

In the case of a superconducting tip and a superconducting sample as shown in Figure 2-2(b), the tunnel current and the local density of states at low temperature are, of course, convolutions of both $D_S(E)$ and $D_t(E)$, each of which has the form described by the equation (2-15). The tunnel current at low temperature is given by

$$I(V, \vec{r}) \propto \mathrm{Re}\int_{-\infty}^{\infty}\frac{|E - i\Gamma|}{\sqrt{(E - i\Gamma)^2 - \Delta_2^2}}\frac{|(E - i\Gamma) - eV|}{\sqrt{(E - i\Gamma - eV)^2 - \Delta_1^2}}\{f(E - eV) - f(E)\}dE \tag{2-17}$$

Superconductor/insulator/superconductor (SIS) tunnel junctions have better energy resolution than superconductor/insulator/normal metal (SIN) tunnel junction. It is

because the existence of the sharp coherence peaks in the density of states of both electrodes in the SIS junction suppresses the thermal smearing effect. This makes the SIS junction superior for determining the superconducting gap to the SIN junction where a normal metal has thermally broadened density of states near the Fermi energy.

(iv) Strong-coupling superconductors

Distinct deviations from the BCS density of states outside the superconducting energy gap were observed at energies comparable to the Debye energy for Pb (Giaever1962). It turned out that Pb is a strong electron-phonon coupling superconductor and the weak coupling approximation in the BCS theory is no longer valid in this material. We have to treat the effect of electron-phonon interactions more realistically. The measured dI/dV curve of Pb/I/Pb STM junctions will be presented in the next section, indicating the deviations from the BCS prediction of the density of states due to the strong phonon coupling at the energies corresponding to the longitudinal and transverse phonons.

For high-T_C superconducting cuprates of which the pairing mechanism is still under debate, attempts to extract the possible energy due to the strong electron-phonon coupling were done for $YBa_2Cu_3O_{7-\delta}$ although the authors cautioned that the "gap" observed in the normalized conductance data for $YBa_2Cu_3O_{7-\delta}$ is not of the BCS form. Nevertheless, T_C was calculated from the normal state parameters, $\alpha^2F(\omega)$ and λ derived from the observed dI/dV spectrum and found that it was 2/3 of the measured T_C of this material (Dynes1992). Recently microscopic studies of the phonon structure by STM were performed for $Bi_2Sr_2CaCu_2O_{8+\delta}$ (Lee2006) and electron-doped cuprate, $Pr_{0.88}LaCe_{0.12}CuO_4$ (Niestemski2007). They have, however, extracted the phonon

energies from positive peaks of d^2I/dV^2 spectra, with an assumption that the observed gap was equal to the superconducting gap, rather than following the procedure described above. Furthermore it has been suggested that their results could be interpreted as inelastic tunneling associating with an apical oxygen within the barrier (Pilgram2006, Scalapino2006). Electron tunneling from the STM tip can lose energy to an oxygen vibrational phonon mode inside the barrier, yielding a new tunneling channel and mimicking the results reported.

2-2 Superconducting STM tip and S/I/S STM tunnel junctions

A superconducting STM tip was originally proposed for spin polarized tunneling measurements (Meservey1988) and it was first fabricated by Pan *et al.* using mechanically sharpened Niobium (Nb) wire cleaned by field emission (Pan1998). They clearly observed the superconducting energy gap of the Nb tip over the Au sample although there was a large variation of the energy gap from tip to tip. This might be due to an existence of a remnant amount of NbO, one of Nb oxides on the tip. NbO is metallic at 4.2 K unlike insulating NbO_2 and Nb_2O_5, and any residue of this material on the tip becomes a proximity layer with unknown thickness, causing the gap decrease from the bulk value. A reproducible and stable superconducting tip fabrication method was developed in the Dynes group (Naaman2001a) and we used the same recipe for superconducting STM studies of $Bi_2Sr_2CaCu_2O_{8+\delta}$ (BSCCO). A $Pt_{0.8}/Ir_{0.2}$ tip is mechanically cut from a 0.25 mm diameter wire. Tips are then placed in the bell-jar evaporator where the tip apex is pointing to the evaporation sources. A 5500 Å thickness of lead (Pb) is deposited on the tips at a rate of ~ 40 Å/s followed by a 36 Å thickness of

silver (Ag) deposition at a rate of 1 Å/s without breaking vacuum. The thickness of the film is monitored with a 5 MHz quartz crystal with the associated oscillating circuit. The pressure during the deposition is ~ 5×10^{-6} Torr or lower. The thick layer of Pb was chosen such that at 2.1 K, well below transition temperature of Pb (T_C = 7.2 K), there would be bulk superconductivity in the tip (superconducting coherence length, ξ_0, of Pb is ξ_0 = 830 Å). The silver serves as a capping layer to protect the Pb layer from rapid oxidation upon exposure to the atmosphere. The thickness of the Ag layer is thin enough to proximity-couple to the Pb layer, resulting in our tip becoming a superconductor with T_C and Δ only slightly below that of bulk Pb. As a next step for our STM Josephson junctions, we deposited Pb/Ag layers onto a graphite substrate *in situ* to study superconductor/insulator/superconductor (S/I/S) vacuum tunnel junctions. The surface topography of the Pb/Ag film scanned by the superconducting tip at T = 2.1 K is shown in Figure 2-4, from which we can see the Pb grains, ~ 200 Å long and ~ 50 Å wide, piled up to form the thick Pb layer.

In order to see superconductivity of our superconducting tip, we performed the current-voltage (*I-V)* characteristic measurements on this surface at T = 2.1 K. Figure 2-5 shows normalized *I-V* curves obtained from these measurements done at both San Diego (symbols) and Berkeley (line), indicating reproducibility of the superconducting energy gap of our superconducting tips.

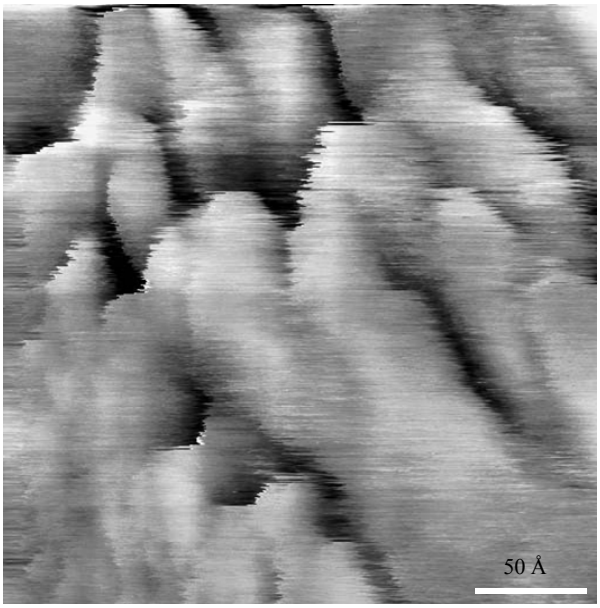

Figure 2-4 Topography of Pb/Ag film at T = 2.1 K. The superconducting tip and the film deposited *in situ* on a graphite substrate are forming the S/I/S tunnel junction.

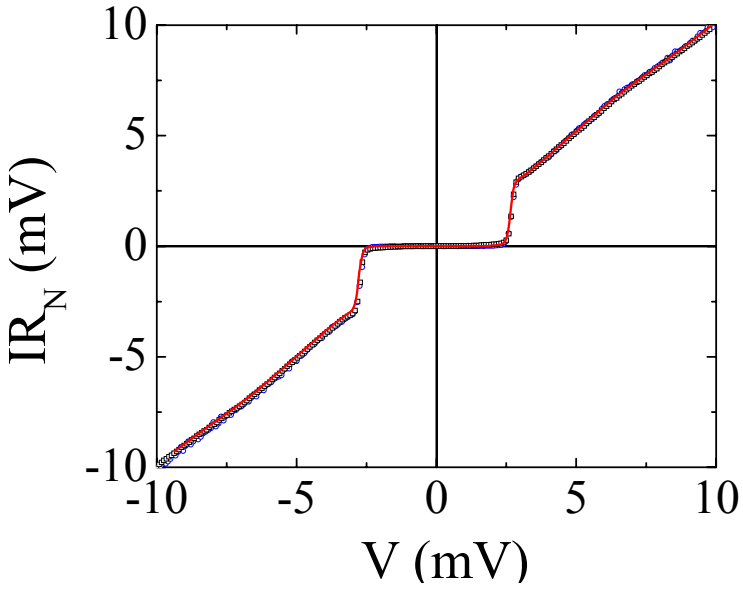

Figure 2-5 Normalized *I-V* characteristics at T = 2.1 K of S/I/S tunnel junction formed between Pb/Ag films and superconducting tip fabricated in different locations, San Diego (points) and Berkeley (line). The junction normal state resistance, R_N, is determined from a slope of each *I-V* curve between 4 meV and 10 meV. Note that our recipe for the superconducting tip shows good reproducibility.

dI/dV measurements of these Pb/I/Pb STM junctions are performed using standard lock-in techniques at the junction normal state resistance, R_N = 25 MΩ and small ac bias modulation is added (250 μV, f = 1.2 kHz) on the bias voltage. The tunnel junction parameters ($I_{setpoint}$ = 200 pA and V = 5 mV) are used for the feedback cycle between sweeps and R_N is determined from the slope of *I-V* characteristic for voltages above the Pb gap. The dI/dV represents the convolution of the density of states for both the tip and the sample as described in the preceding section. The spectrum shown in Figure 2-6 is a characteristic of S/I/S tunnel junctions: very sharp coherence peaks corresponding to $eV = \pm (\Delta_{tip}+\Delta_{sample})$, from which we obtained $\Delta_{tip} = \Delta_{sample}$ = 1.35 meV. Moreover, the deviations from the BCS density of states outside the Pb gap due to strong-coupling effects is clearly seen at energies corresponding to the transverse and longitudinal phonon energies, $eV_T - 2\Delta$ = 4.5 meV and $eV_L - 2\Delta$ = 8.5 meV, respectively. Figure 2-7 represents several *I-V* characteristics measured at different R_N by changing tip-sample distance sequentially. This is done by either increasing the setpoint tunnel current or decreasing the bias voltage. A voltage change near the gap causes a large conductance change due to the nonlinearity of the *I-V* characteristic so that the junction resistance could be varied dramatically with a small bias change near the gap compared to the linear region above the gap. The gap size remains unchanged as R_N is decreased. Low leakage current below the Pb gap and the observation of the phonon structure confirm high quality vacuum tunnel junctions.

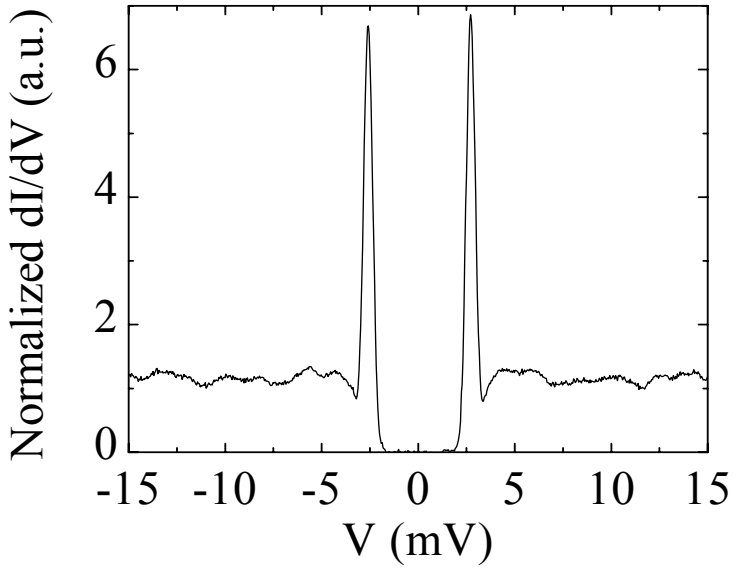

Figure 2-6 Normalized dI/dV spectrum of Pb/I/Pb STM junctions at T = 2.1 K. The Pb phonon structures are clearly seen at energies corresponding to the transverse and longitudinal phonon energies.

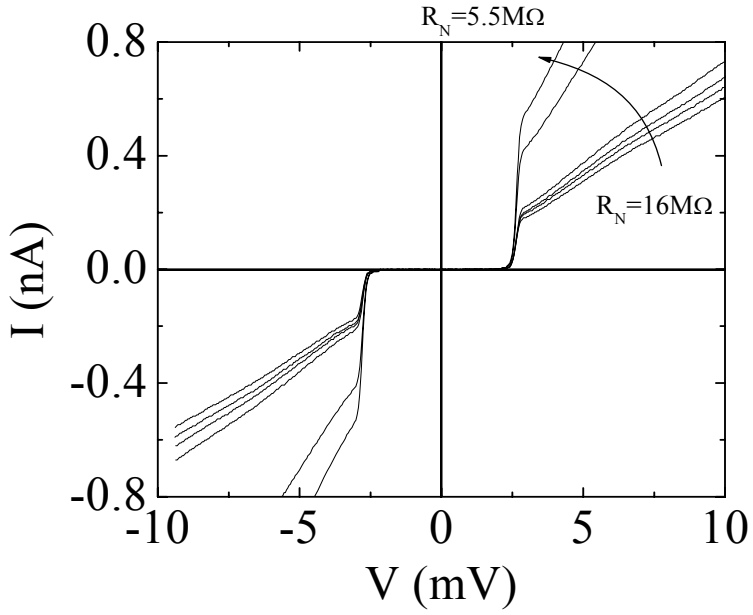

Figure 2-7 *I-V* characteristics of Pb/I/Pb STM junctions at T = 2.1 K. *I-V* curves are measured as the junction normal state resistance R_N is varied (z direction) with the tip position fixed (x,y fixed).

S/I/S STM junctions formed between the superconducting Pb tip and overdoped BSCCO single crystals show different features than those observed for the Pb/I/Pb STM junctions. Firstly, the energy gap of BSCCO is an order of magnitude larger than the Pb gap and secondly, the dI/dV spectrum for the BSCCO gap has a "gaplessness" – non zero conductance at the Fermi energy – with an asymmetric normal state background conductance. Figure 2-8(a) represents an *I-V* characteristic of Pb/I/overdoped BSCCO STM junctions at T = 2.1 K taken at R_N = 10 MΩ, clearly showing the Pb gap around 1.4 meV. The Pb gap edge does not have a sharp onset of tunnel current compared to that of Pb/I/Pb STM junctions because states exist all the way to the Fermi energy in the density of states of BSCCO. Quasiparticles can tunnel at the Fermi energy of BSCCO. The inset of Figure 2-8(a) shows a dI/dV spectrum in the region of the Pb gap. The conductance outside the Pb gap is affected by the large energy gap of BSCCO (Δ_{BSCCO} = 40 meV). Figure 2-8(b) represents a dI/dV spectrum taken with a large sweep range for the local density of states of BSCCO at the same location (R_N = 500 MΩ). The modulation amplitude added on the bias voltage is 2.5 mV_{RMS}. Valles *et al.* studied *I-V* characteristics and the dI/dV spectra of Pb/I/$YBa_2Cu_3O_{7-\delta}$ (YBCO) planar tunnel junctions (Valles1991) and our results for Pb/I/BSCCO STM junctions are similar to those. The *I-V* curve with the Pb gap is more asymmetric than those observed in Pb/I/YBCO planar tunnel junctions because the density of states of BSCCO has more asymmetry than that of YBCO. The background conductance of BSCCO has a linear voltage dependence with a negative slope, $-\alpha V$ where α is approximately constant (Gomes2007), while YBCO has a symmetric "V" shape background conductance (Valles1991). This results in distortions of the *I-V* (or dI/dV) curve near the Pb gap.

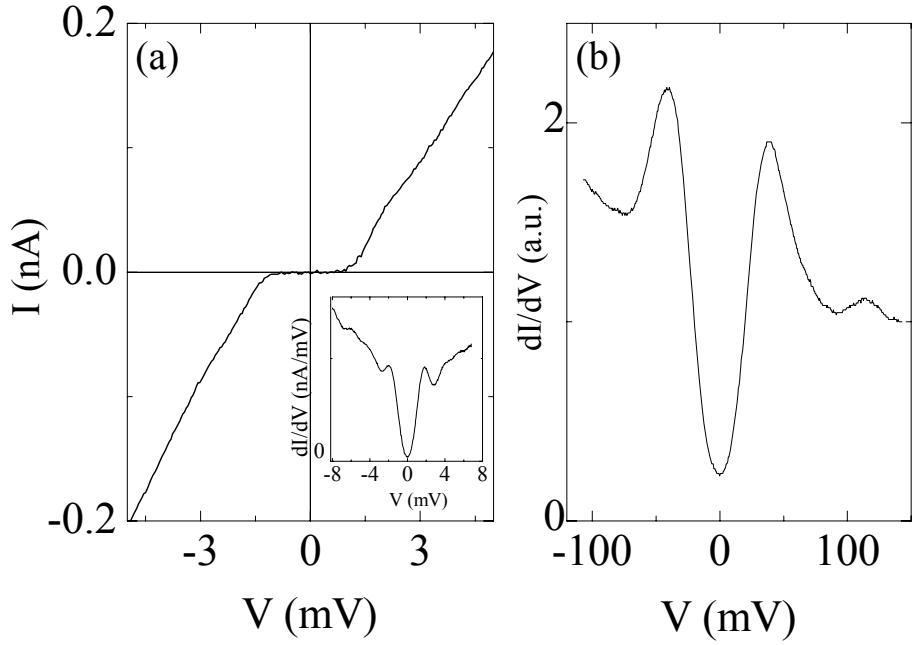

Figure 2-8 (a) *I-V* characteristic of Pb/I/overdoped BSCCO STM junctions at T = 2.1 K, clearly showing a Pb gap around 1.4 meV. Note the absence of leakage although the Pb gap edge is smeared compared to that of Pb/I/Pb STM junctions due to finite states all the way to the Fermi energy in the BSCCO density of states. Inset: dI/dV for the Pb gap taken at R_N = 10 MΩ. The conductance outside the Pb gap is affected by a relatively large energy gap of BSCCO (Δ_{BSCCO} = 40 meV). (b) dI/dV spectrum taken over a large voltage range for the BSCCO gap at the same location. R_N = 500 MΩ. The modulation amplitude added on the bias voltage is 2.5 mV_{RMS}.

As for the resolution of our superconducting tip, we also fabricated the superconducting tip with a 1100 - Å - thick Pb layer by using 10 Å of a Ge seed layer, however, atomic resolution images are not routinely obtained. It might be because we do not use any tip cleaning process such as field emission after transferring the tip to the STM chamber upon exposure to atmosphere. We avoid this because high voltage field emission may destroy the Pb layer. Baking the tip in high vacuum might help increase the tip resolution.

As a conclusion of this section we have developed a reproducible method to fabricate a superconducting tip which has been well characterized to show a reproducible gap. It will be shown later that this reproducibility will be crucial to carrying out the local Josephson measurements.

2-3 Josephson effect

2-3-1 General description

The Josephson effect is the tunneling of Cooper pairs through a barrier separating two superconductors (Josephson1962). Figure 2-9 is a schematic of the Josephson junction where two superconductors are separated by a thin insulating barrier. The macroscopic superconducting wave functions of the superconductor 1 and 2 are defined as $\Psi_0^{(1)}(\mathrm{N}_1)$ and $\Psi_0^{(2)}(\mathrm{N}_2)$ with ground state energy $\mathrm{E}_0^{(1)}(\mathrm{N}_1)$ and $\mathrm{E}_0^{(2)}(\mathrm{N}_2)$, respectively. N_1 and N_2 are the number of pairs in each superconductor. They are the eigenstates and eigenenergies of Hamiltonian H_1 and H_2 for each superconductor. Let us assume that no bias voltage is applied to the Josephson junction so that the Fermi energies of two superconductors are equal, $E_{F1} = E_{F2}$. The ground state of the combined system is

$$\Psi_0 = \Psi_0^{(1)}(\mathrm{N}_1)\Psi_0^{(2)}(\mathrm{N}_2) \tag{2-18}$$

$$\mathrm{E}_0 = \mathrm{E}_0^{(1)}(\mathrm{N}_1) + \mathrm{E}_0^{(2)}(\mathrm{N}_2) \tag{2-19}$$

The energy difference due to n pairs transfer is $\delta E_n = (2en)^2/2C$ where C is the capacitance of the Josephson junction. Since δE_n could be very small for the macroscopic-size tunnel junction, then the state with n pairs transferred is almost

degenerate with the initial state. As the barrier between two superconductors becomes sufficiently thin, the tunneling interaction dominates the electrostatic energy and the phase coherent state over two superconducting electrodes is formed.

We can treat the tunneling interaction as a perturbation as was done for electron tunneling and pair transfer in the Many-body problems (Anderson1964, Anderson1967, Scalapino1969). The Hamiltonian of the tunneling interaction has the same form as that of single particle electron tunneling as appeared in the equation (2-4),

$$H_T = \sum_{p,k} \boldsymbol{T}_{pk} (C_{p\uparrow}^{+} C_{k\uparrow} + C_{-k\downarrow}^{+} C_{-p\downarrow}) + H.C.$$

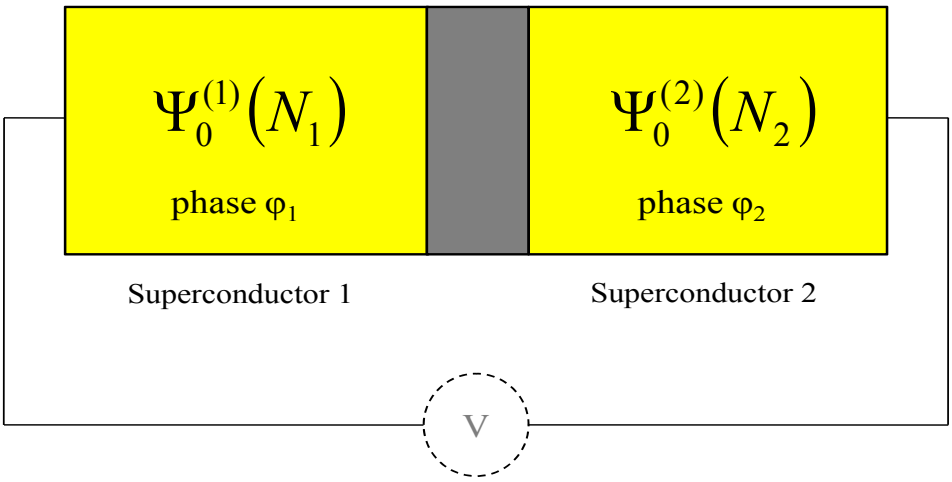

Figure 2-9 Superconductors separated by a gap forming the Josephson junction. Macroscopic wave functions of each superconductors are $\Psi_0^{(i)}(N_i)$ where i=1 and 2. Fermi energies of two superconductors, E_{F1} and E_{F2} are equal without an applied voltage to the junction.

Since H_T transfers only one electron, we need to consider the matrix element of the second order to lift the degeneracy. Assuming that the left (right) superconducting electrode has the superconducting energy gap, $\Delta_{1(2)}$ and the phase $\varphi_{1(2)}$, respectively, the perturbation calculation for the degenerate states yields the condensation energy at $T = 0$,

$$\delta E = -4\pi N(0)^2 |\boldsymbol{T}|^2 \frac{\Delta_1 \Delta_2}{\Delta_1 + \Delta_2} K\left(\frac{|\Delta_1 - \Delta_2|}{\Delta_1 + \Delta_2}\right) \cos(\varphi_2 - \varphi_1) = -E_J \cos\varphi \quad (2\text{-}20)$$

where $N(0)$ is quasiparticle density of states at the Fermi energy, $K(x)$ a complete elliptic integral of the first kind and $\varphi \equiv \varphi_2 - \varphi_1$, **the relative phase difference between the two superconductors** (Anderson1964). E_J is called the Josephson binding energy given by

$$E_J = \frac{\hbar}{e^2 R_N} \frac{\Delta_1 \Delta_2}{\Delta_1 + \Delta_2} K\left(\frac{|\Delta_1 - \Delta_2|}{\Delta_1 + \Delta_2}\right) \quad (2\text{-}21)$$

It is important to note that the condensation energy δE is a function of the phase difference of two superconductors.

Since the number of pairs, n and the phase φ are conjugate variables obeying the uncertainty relationship, $\delta n \delta\varphi \leq 2\pi$, we need to treat n and φ as operators, satisfying, $[\hat{n}, \hat{\varphi}] = -i$. Thus the pair current operator is

$$\hat{I} = 2e\frac{d\hat{n}}{dt} = \frac{2e}{i\hbar}\left[\hat{H}, \hat{n}\right] = \frac{2e}{\hbar}\frac{\partial H(\varphi)}{\partial \varphi} \quad (2\text{-}22)$$

Therefore the expectation value of the current is given by

$$I = -\frac{2e}{\hbar}\frac{\partial}{\partial\varphi}E_J\cos\varphi = I_C\sin\varphi \tag{2-23}$$

where the relation, $\left[\hat{n},\hat{H}\right] = -i\frac{\partial H}{\partial\varphi}$ is used. $I_C = 2eE_J/\hbar$ is called the maximum supercurrent of the Josephson junction. The equation (2-23) is **the first Josephson equation, describing the dc pair current flow through the barrier at zero voltage**.

For identical superconductors, Ambegaokar and Baratoff derived the temperature dependent binding energy (Ambegaokar1964),

$$E_J(T) = \frac{\hbar I_c}{2e} = \frac{\pi\hbar}{4e^2}\frac{\Delta(T)}{R_N}\tanh\left(\frac{\Delta(T)}{2k_BT}\right) \tag{2-24}$$

For $T \ll T_C$, $\tanh(\Delta/2k_BT) \approx \tanh(T_C/T) \approx 1$. Therefore the equation (2-24) is reduced to

$$E_J = \frac{\pi\hbar}{4e^2}\frac{\Delta(0)}{R_N} \tag{2-25}$$

It is easy to check that the equation (2-25) coincides with the zero temperature binding energy formula (equation 2-21) for $\Delta_1 = \Delta_2$ using $K(0) = \pi/2$. Since the supercurrent is a tunneling current of the Cooper pairs, so that it increases as R_N is decreased. It is also important to note that I_C is inversely proportional to R_N, but the product, I_CR_N is an

intrinsic quantity, which depends only on the superconducting order parameter of the materials.

Now let us consider a finite voltage is applied across the junction. In this case the Fermi energy of two superconducting electrodes are no longer equal and the difference of the Fermi levels of two electrodes is eV. Since the energy difference after n pairs transfer is $\delta E_n = 2n(E_{F2} - E_{F1})$, and using the relation,

$$\left[\hat{\varphi}, \hat{H}\right] = i\frac{\partial H}{\partial n}$$

Then

$$\frac{d\varphi}{dt} = \langle\frac{1}{i\hbar}\left[\hat{H}, \hat{\varphi}\right]\rangle = -\frac{1}{\hbar}\frac{\partial H}{\partial n} = \frac{2}{\hbar}(E_{F1} - E_{F2}) = \frac{2eV}{\hbar} \tag{2-26}$$

This is **the second Josephson equation for the ac Josephson effect**. The resulting pair current is oscillating at the frequency $2eV/\hbar$. The significance of the equation (2-26) that a time dependence of phase difference generates a voltage or that a voltage generates a time dependent (oscillatory) phase difference.

To analyze the behavior of the Josephson junction, it is useful to regard the equivalent circuit of a Josephson junction as a parallel combination of a resistor for dissipation in the finite voltage regime and a capacitor with shunting capacitance between two electrodes (Figure 2-10). '×' represents the Josephson element. The circuit equation is simply

$$I = I_c \sin\varphi + \frac{V}{R} + C\frac{dV}{dt} \tag{2-27}$$

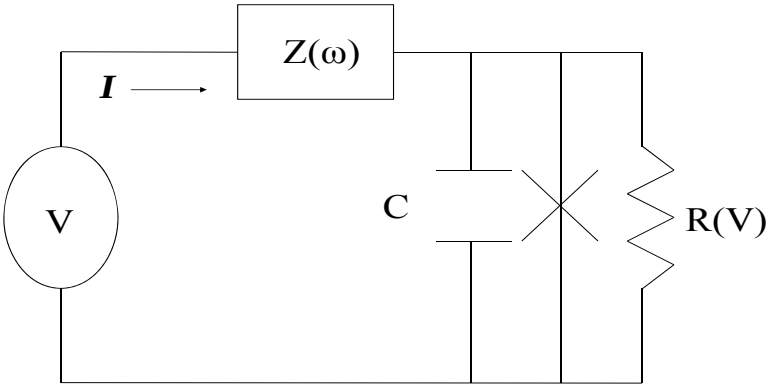

Figure 2-10 Equivalent circuit of a Josephson junction

Using the second Josephson equation (2-26) to eliminate V from (2-27), we obtain a differential equation for the phase :

$$\frac{d^2\varphi}{dt^2} + \frac{1}{RC}\frac{d\varphi}{dt} + \omega_P^2 \sin\varphi = \omega_P^2 \frac{I}{I_C} \tag{2-28}$$

This differential equation is the same as the equation of motion for a pendulum with a natural frequency ω_P with a damping term and a driving force. ω_P is referred to as the Josephson plasma frequency, defined as

$$\omega_P \equiv \sqrt{2eI_c/\hbar C}.$$

Dividing the equation (2-28) by $\omega_P{}^2$ yields a dimensionless differential equation for φ,

$$\frac{d^2\varphi}{d\tau^2} + \frac{1}{Q}\frac{d\varphi}{d\tau} + \sin\varphi = \frac{I}{I_c} \tag{2-29}$$

where $\tau = \omega_P t$ and $Q = \omega_P RC$. The equation (2-29) is also the same as that of a particle of mass $(\hbar / 2e)^2 C$ moving along the φ axis in an effective potential (Scott1969).

$$U(\varphi) = -E_J \cos\varphi - \left(\frac{\hbar I}{2e}\right)\varphi \tag{2-30}$$

The schematic of this potential is shown in Figure 2-11. E_J, the Josephson binding energy is the height of the potential barrier. The particle is moving in this potential subject to a viscous drag force $(\hbar/2e)^2(1/R)\, d\varphi/dt$. This phase-particle analogy is a convenient way to understand the Josephson junction behavior (Fulton1971).

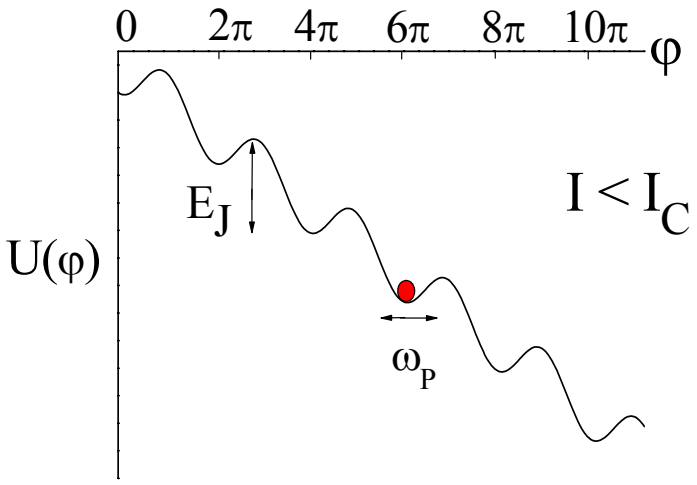

Figure 2-11 Washboard potential for the Josephson phase dynamics for $I < I_C$.

Stewart and McCumber introduced a damping parameter, $\beta_C = Q^2$. The Josephson junction behaves differently in the two limits of β_C (Stewart1968, McCumber1968). If $\beta_C \ll 1$ in the case of small capacitance or small shunt resistance of the junction, the Josephson junction is overdamped. In this limit the phase particle is locked in one of the potential minima until $I < I_C$. A larger Josephson binding energy, E_J, results in larger I_C (from Ambegaokar-Baratoff formula (equation 2-24)), but this can be easily understood from the washboard potential picture, *i.e.*, the larger E_J corresponds to a deeper potential well so that the phase remains locked for larger bias current. When I exceeds I_C, the particle starts rolling down the washboard potential, resulting in a voltage due to the second Josephson equation (2-26). In the overdamped case ($\beta_C \ll 1$), the first term of the dimensionless differential equation (2-29) can be neglected and the *I-V* characteristic in the voltage state can be calculated from integrating the resulting equation. Therefore the zero bias supercurrent ($I < I_C$) and the Ohmic region ($I > I_C$) is smoothly connected by

$$V = R\sqrt{(I^2 - I_c^2)} \tag{2-31}$$

shown in Figure 2-12(a). For $\beta_C \gg 1$, on the other hand, it is underdamped and the particle rolls on the potential with very little friction. Once the bias current exceeds I_C, the particle is steadily moving down the potential so that V jumps discontinuously up to $V \approx I_C R$ (running state). If the current is reduced below I_C, the junction remains in the running state due to the light damping until the retrapping current, I_{CR} is reached. The retrapping current is the current when energy dissipation of the particle from one maximum to the next on the washboard potential due to the damping is equal to the

energy fed in by the driving source. This gives $I_{CR} \approx 4I_C/\pi Q$ at which the particle is trapped into a well again. Therefore the *I-V* curve becomes hysteretic as shown in Figure 2–12(b) where the generic *I-V* curve is drawn (Van Duzer Book). For a tunnel junction, the returning current drops at the voltage corresponding to a sum of the energy gaps on the tunnel junction until it reaches the retrapping current.

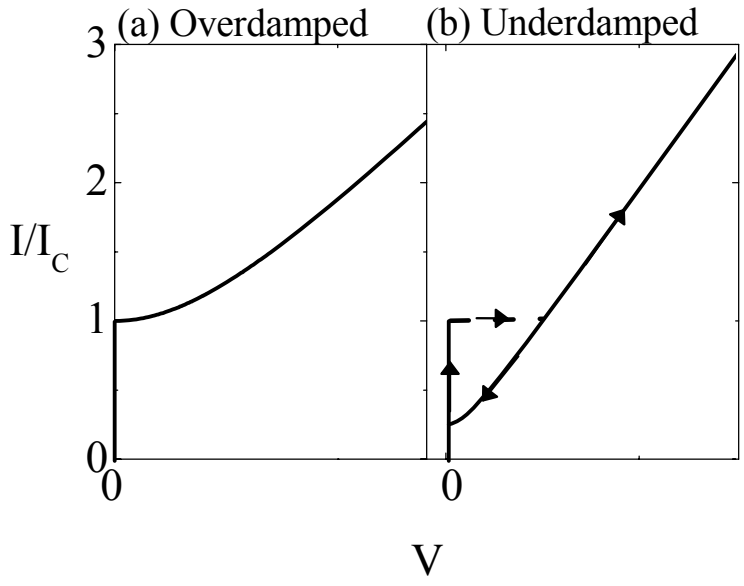

Figure 2-12 Calculated *I-V* characteristics for a Josephson junction that is (a) overdamped for $\beta_C << 1$ and (b) underdamped for $\beta_C >> 1$ at $T = 0$.

2-3-2 Ultra small Josephson junctions and phase fluctuations

The novel feature of the superconducting STM is a superconducting tip (Pb with a Ag capping layer) in close proximity to a superconducting sample to form a superconductor/insulator/superconductor (S/I/S) tunnel junction (Naaman2001a). The signature Josephson response of the superconducting STM differs from that of typical low R_N planar S/I/S devices. Because of the experimental base temperature (T = 2.1 K)

and large R_N associated with an STM, the Josephson binding energy, E_J, is smaller than k_BT for the Josephson STM in this thesis (see the R_N^{-1}dependence in the equation 2-24). For example with an STM resistance of 50 kΩ, E_J/k_B is roughly 1 K. Also for ultra-small tunnel junctions, the Coulomb charging energy, E_C can be large. We estimate the capacitance, C, of the STM junction formed between the conical tip apex and the sample surface to be about 1 fF. $E_C = e^2/2C$ is therefore of order 1K: comparable with E_J, but smaller than k_BT. The time-scale of an electron tunneling in the STM junction is much shorter than $\hbar/E_C$, so that the electron is swept away long before the charging effects become relevant. Because k_BT is the dominant energy, the phase difference of the two superconductors, φ, is not locked in a minimum of the sinusoidal E_J vs. φ washboard potential, but is thermally excited and diffusive (Figure 2-13). Near zero bias voltage the observed Josephson current is therefore dependent on the bias due to the dissipative phase motion (see the second Josephson equation 2-24).

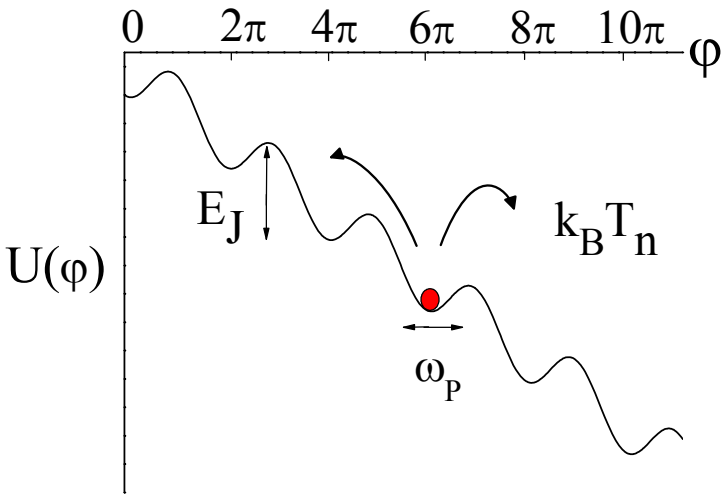

Figure 2-13 Josephson phase dynamics in classical thermal fluctuation regime

The phase diffusion model was first proposed by Ivanchenko and Zil'berman (Ivanchenko1968) and later by others (Ingold1994, Harada1996). In this model we can consider the thermal fluctuations as Johnson noise generated by a resistor Z_{ENV} at a noise temperature T_n; both parameters depend only on the experimental set-up. Ivanchenko and Zil'berman assumed that 2nd time derivative term can be neglected due to the small capacitance of the ultra-small junction and included the white noise source $U(t)$ in the circuit equation biased with an emf E (Ivanchenko1968).

$$\frac{1}{Z_{ENV}}\frac{d\varphi}{dt}+\frac{2e}{\hbar}I_c\sin\varphi=\frac{2e}{\hbar}\frac{(E+U(t))}{Z_{ENV}} \tag{2-32}$$

where $U(t)$ satisfies $\langle U(t)U(0)\rangle = 2k_BT_nZ_{ENV}\delta(t)$. Introducing the dimensionless variables, $\tau = 2eI_CZ_{ENV}/\hbar$, $\varepsilon = E/Z_{ENV}I_C$, $u = U/Z_{ENV}I_C$, and $\alpha = E_J/k_BT_n$ into the equation (2-32) yields

$$\frac{d\varphi}{d\tau}=(\varepsilon-\sin\varphi)+u(\tau) \tag{2-33}$$

and $\langle u(\tau)U(0)\rangle = (2/\alpha)\delta(\tau)$. We can regard the equation (2-33) as the Langevin equation of the Josephson phase and the corresponding Fokker-Planck equation is

$$\frac{\partial W}{\partial\tau}=\frac{1}{\alpha}\frac{\partial^2W}{\partial\varphi^2}+W\cos\varphi+(\sin\varphi-\varepsilon)\frac{\partial W}{\partial\varphi} \tag{2-34}$$

where $W = W(\varphi, \tau|\varphi_0, 0)$, is the density of the probability of finding a phase in the interval $\varphi + d\varphi$, at time τ if $\varphi = \varphi_0$ at $\tau = 0$. The equation for the Fourier transform of $W(\varphi, \tau|\varphi_0, 0)$, $x_n = \int_{-\infty}^{\infty} d\varphi e^{in\varphi} W(\varphi, \tau|\varphi_0, 0)$ becomes

$$\frac{\partial x_n}{\partial \tau} = -n\left[\left(\frac{n}{\alpha} - i\varepsilon\right) x_n(\tau) + \frac{x_{n+1}(\tau) - x_{n-1}(\tau)}{2}\right] \tag{2-35}$$

As $\tau \to \infty$, the system goes to equilibrium, resulting in $\partial x_n/\partial \tau = 0$. Thus we obtain the equation in finite difference for $x_n(\tau)$, which can be solved using the modified Bessel function, $I_\nu(z)$,

$$x_n(\infty) = \frac{I_{n-i\alpha\varepsilon}(\alpha)}{I_{-i\alpha\varepsilon}(\alpha)} \tag{2-36}$$

The dc Josephson current is obtained from the relation

$$I = I_c\langle \sin\varphi \rangle = I_c \lim_{\tau\to\infty} \int_{-\infty}^{\infty} d\varphi \sin\varphi W(\varphi, \tau|\varphi_0, 0) = I_c \frac{x_1(\infty) - x_{-1}(\infty)}{2i} \tag{2-37}$$

where we used the relation, $\sin\varphi = \left(e^{i\varphi} - e^{-i\varphi}\right)/2i$. Since the observed current must be real, *i.e.*, $I^* = I$. Therefore $x_n^* = x_{-n}$ and

$$I(E) = I_c \mathrm{Im}[x_1(\infty)] = I_c \mathrm{Im}\left[\frac{I_{1-i\frac{E}{V_P}}\left(E_J/k_B T_n\right)}{I_{-i\frac{E}{V_P}}\left(E_J/k_B T_n\right)}\right] \tag{2-38}$$

where $V_P = (2e/\hbar)Z_{ENV}k_BT_n$ and Im[x] denotes the imaginary part of x. Experimentally, however, we are interested in the pair current as a function of the voltage across the junction. That is given by averaging the equation (2-32),

$$V = \frac{\hbar}{2e}\frac{d}{dt}\langle\varphi\rangle = I_cZ_{ENV}\left(\frac{E}{I_cZ_{ENV}} - \frac{I(E)}{I_c}\right) = E - I(E)Z_{ENV} \tag{2-39}$$

In the limit of $\alpha = E_J/k_BT_n \ll 1$, the equation (2-38) has a simple analytic form for the *I-V* characteristics,

$$I(V) = \frac{I_c^2Z_{ENV}}{2}\frac{V}{V^2 + V_P^2} \tag{2-40}$$

As I described above, the relevant energy scale of our STM Josephson junctions is $\alpha = E_J/k_BT_n \leq 1$, so that the analytic form of the equation (2-40) is applicable to analyzing our data.

Now the pair current has a voltage dependence due to the diffusive phase motion. V_P, as a function of T_n and Z_{ENV}, is the voltage where the pair current becomes maximum and it will not change if T_n and Z_{ENV} are constant parameters intrinsic to the junction's environment, while I_C increases as R_N is decreased. Thus the thermally fluctuated Josephson current is characterized by three quantities, maximum supercurrent I_C, T_n and Z_{ENV}. T_n is an effective noise temperature for the ultra-small junction. This temperature can be elevated by noise from the room temperature electronics unless all the leads connecting to the junction are heavily filtered. Z_{ENV} is the impedance of the junction's environment or the electronic circuit where the junction is embedded. It is reported that

for ultra-small tunnel junctions, the Josephson phase dynamics is at very high frequency, characterized by the Josephson plasma frequency, ω_P or $E_J/\hbar$ (for STM Josephson junctions, it is of order of $10^{11} \sim 10^{12}$ Hz) and the frequency dependent damping at this frequency region is dominated by stray capacitance and inductance of the cables connecting the junction to the external circuit (Ono1987, Martinis1989, Kautz1990, Ingold1992). This impedance is represented as $Z(\omega)$ in Figure 2-10. The cables will load the junction with an impedance of the order of free space impedance, $Z_0 = \sqrt{\mu_0/\varepsilon_0} = 377\Omega$. The macroscopic Josephson junction has two distinct behaviors as shown in Figure 2-12 depending on the value β_C. The ultra-small Josephson junction will show that the phase dynamics at high frequency are characteristic of an overdamped junction due to the damping of Z_{ENV}, while the voltage state at low frequency (quasiparticle running state) is of an underdamped junction because the damping is dominated by large junction normal state resistance (Ono1987, Martinis1989, Kautz1990). Figure 2-14 shows the calculated pair current by the phase diffusion model (2-38) with various $\alpha = E_J/k_B T_n$, clearly indicating that the phase diffusion branch is enhanced with a peak at $V = V_P$. As the Josephson binding energy, E_J becomes larger (R_N is smaller in case of STM), the thermally fluctuated Josephson current increases. As the noise temperature T_n is decreased, V_P moves to zero bias. It is worth noting that for $\alpha \rightarrow \infty$, the zero bias supercurrent I_C is observable, while for $\alpha \rightarrow 0$, the thermally fluctuated Josephson current is completely smeared out by the thermal energy so that we can only see the quasiparticle tunnel current. It is also seen that the simple form of equation (2-40) could be a good approximate form for the exact solution (equation 2-38) in the range of $0 \leq \alpha \leq 1$ where our STM Josephson measurements are done. (Naaman thesis).

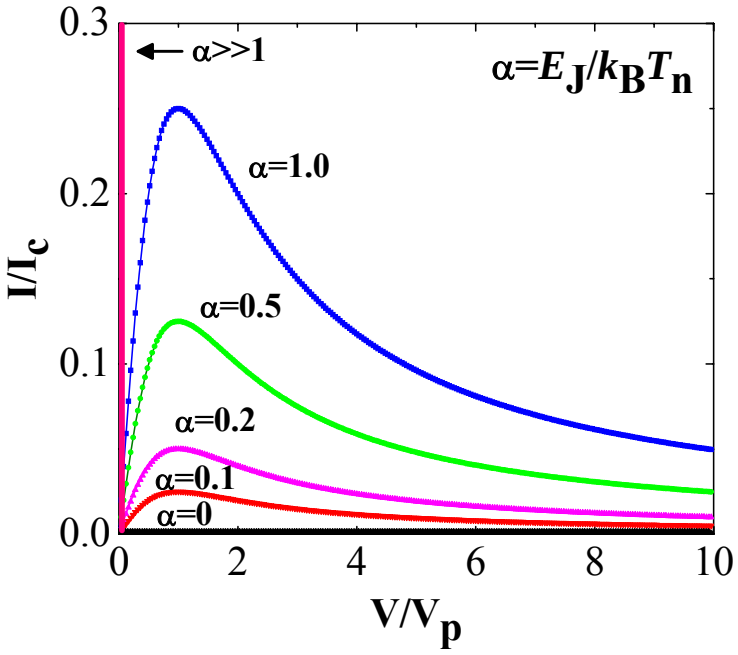

Figure 2-14 The calculated Josephson currents in the strong thermal fluctuation regime using phase diffusion model, equation (2-38) for various $\alpha = E_J/k_BT_n$. The pair current becomes maximum at V_P and the amplitude is increased as α (or E_J) becomes larger. In the limit of large α, the binding energy completely overcomes the thermal energy, resulting in reappearance of zero bias supercurrent. On the other hand, no pair current is observed for $\alpha = 0$ (or $k_BT_n >> E_J$) and only the quasiparticle *I-V* curve is observed.

Finally we have derived the form for the pair current due to the classical phase diffusion. In the ultra-small tunnel junction in general, however, the charging energy will become the same order of magnitude as the binding energy or larger so that a tunneling event is described as charge transfer between the junction and the junction's environment. From the uncertainty relationship $\delta n \delta\varphi \leq 2\pi$, δn could be very small with increasing E_C/E_J ratio, the quantum fluctuation of the phase is then increased. Thus the problem of ultra-small Josephson junction is needed to be treated "quantum mechanically". This picture requires that we regard the binding energy in the

Hamiltonian of the ultra-small Josephson junction as an operator, that is, $E_J cos\varphi = (E_J/2)exp(i\varphi)$ as the operator to transfer the Cooper pair between the environment and the junction in view of $exp(i\varphi)Qexp(-i\varphi) = Q - 2e$. For the quantum mechanical approach, $P(E)$ theory was proposed by Devoret *et al.* (Devoret1990) where $P(E)$ is the probability that a tunneling Cooper pair emits the energy *E* to the environment. Ingold *et al.* later studied the phase dynamics in the fluctuation regime to show that we would find the same result as the classical phase diffusion model in the limit of high temperature and low impedance in the quantum mechanical description (Ingold1994). Therefore I will use the classical phase diffusion model to interpret the results of our STM Josephson junctions.

2-3-3 STM Josephson junctions formed between conventional superconductors

(i) Pb/I/Pb STM junctions

Experimentally we are interested in determining the Josephson $I_C R_N$ product, an intrinsic quantity that depends only on the superconducting pair wave function of the material forming the Josephson junction and temperature as seen in the preceding section. If we observe the phase diffusion branches in our STM Josephson junctions, we can characterize them by identifying two parameters, T_n and Z_{ENV} and then we can directly derive $I_C R_N$ of the material of interest by comparing the observed data and fits to the phase diffusion model. The operation of this superconducting STM has been demonstrated with the observation of Josephson tunneling between the tip and superconducting Pb films at University of California, San Diego (Naaman2001b). We have repeated this experiment on the Berkeley campus. Figure 2-15 shows the observed *I-V* characteristics (lines) for STM Josephson junctions formed between a

superconducting tip made by a deposition of Pb (5500 Å)/Ag (36 Å) proximity bilayer onto mechanically cut Pt/Ir wire and a superconducting film made by a deposition of a Pb/Ag bilayer *in situ* onto a freshly cleaved graphite substrate. Surface morphology of the superconducting film is shown in Figure 2-4. Since the tunnel junction is biased through the voltage divider near the scanner, the voltage V across the tunnel junction is not identical to that measured outside the STM chamber, V_b and they are connected by $V = V_b \times R_2/(R_1 + R_2) - I \times R \,//\, R_2$, where R_1 and R_2 are resistors used in the voltage divider and R_1 = 9.85 kΩ and R_2 = 1.01 kΩ at T = 2.1 K measured by shorting the junction. The parallel combination of these resistors is ~ 1 kΩ and gives an actual loading to the STM junction. Later an additional voltage divider was installed outside the STM cryostat to increase the dynamic range of the potentiometer for changing the bias voltage on the STM controller (RHK Technology, SPM1000). The second voltage divider consists of R_3 = 9.07 kΩ and R_4 = 0.99 kΩ. The right panel of Figure 2-15 shows that the location of the gap does not change as R_N is lowered. The left panel is a close-up view of the *I-V* characteristics near zero bias, clearly showing that as R_N is decreased to enhance the Josephson binding energy, the peaked structures on the *I-V* curves near zero bias appear and the height of the peak becomes larger with further decreasing of R_N. They are very similar to the curves predicted by the phase diffusion model shown in the Figure 2-14. Therefore the observed *I-V* characteristics near zero bias with various R_N are fitted to the phase diffusion model (equation 2-38) with two parameters, V_P and I_C.

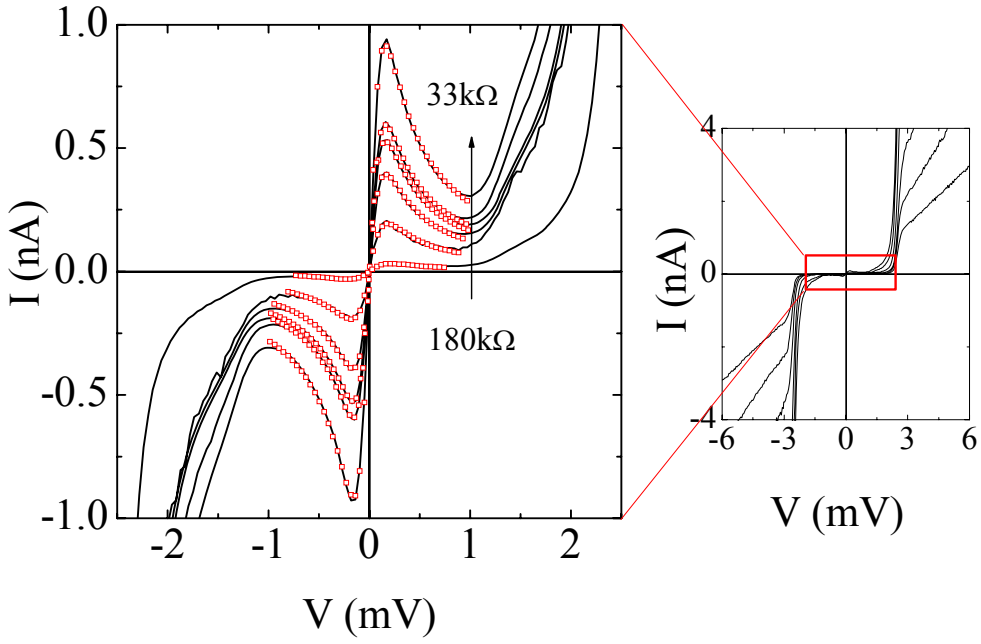

Figure 2-15 *I-V* characteristics of Pb/I/Pb STM junctions at T = 2.1 K. (Right panel) We can see both onset of the tunnel current at $V = 2\Delta$ and structures near zero bias inside a box. (Left) *I-V* characteristics zoomed near zero bias, showing thermally fluctuated Josephson current and the symbols represent two-parameter fits to the phase diffusion model.

In practice, the fitting function used is of the form:

$$I(V) = I_{\text{off}} + A \times \frac{V - V_{\text{off}}}{(V - V_{\text{off}})^2 + V_P^2} \tag{2-41}$$

where $A \equiv I_C^2 Z_{ENV}/2$ and $V_P = (2e/\hbar) Z_{ENV} k_B T_n$. I_{off} and V_{off} are used to account for constant dc offsets coming from instrumentation. These variables are independent of A and V_p so that after finding these values from the first fitting procedure, they are fixed during the subsequent fitting procedure and only A (or I_C) and V_P are allowed to vary.

The best fits to the phase diffusion model are represented by the red symbols in the left panel of Figure 2-15 and the quality of these fits convince us that we have observed the signature of pair tunneling. Noting that $\sqrt{(4e^2/\hbar)\,A/V_P} = I_C \times \sqrt{e/k_B T_n}$, this analysis yields a plot of $I_C \times \sqrt{e/k_B T_n}$ vs. $G_N = 1/R_N$, expected to be linear with zero intercept (no I_C at infinite R_N) and a slope equal to $I_C R_N \times \sqrt{e/k_B T_n}$, shown in Figure 2-16. We can calculate $I_C R_N$ of Pb from the Ambegaokar-Baratoff formula (Ambegaokar1964) or equation (2-24) using Δ = 1.35 meV at T = 2.1 K and including a factor of 0.788 due to strong electron-phonon coupling in Pb (Fulton1968). For T = 2.1 K and T_C (Pb) = 7.2 K, the hyperbolic tangent is very close to one and we get $I_C R_N$ (Pb/I/Pb) = 1.671 mV. Substituting this value into the slope of the linear data fit, we can determine T_n and Z_{ENV} for our STM Josephson junctions, which are intrinsic parameters depending only on the experimental set-up. Current values of these parameters for our apparatus are 15.9 ± 0.1 K and 279 ± 9 Ω, respectively. Slightly higher T_n than the base temperature can be explained by leakage of rf noise to the junction from room temperature electronics. Z_{ENV} is close to the value of the impedance of free space as described in the section 2-3-2. These quantities were measured using a preamplifier with 10^9 gain. We repeated the Josephson measurements to derive T_n and Z_{ENV} using other preamplifiers with lower gains (10^7 and 10^8) to cover the larger tunneling current range and the data are shown in Figure 2-17 only on the positive bias voltage side. All three data sets of the $I_C R_N$ plots in Figure 2-18 fall in a single line, convincing us that the Josephson coupling is enhanced as R_N is decreased and T_n and Z_{ENV} are constant parameters intrinsic to the experimental circumstatces and configuration. The lowest junction normal state resistance we studied was 4.6 kΩ, which is smaller than the quantum resistance of a single channel in the

ballistic regime, $R_Q = h/2e^2 = 12.9$ kΩ. Subharmonic gap structures observed in the Pb/I/Pb STM Josephson junctions indicates that the low resistance STM junction is not in the weak tunneling limit ($|\boldsymbol{T}|^2 = D = 10^{-6}$ or smaller), but somewhat higher transparency, $D \sim 0.1$ contributed from several conduction channels (Naaman2004).

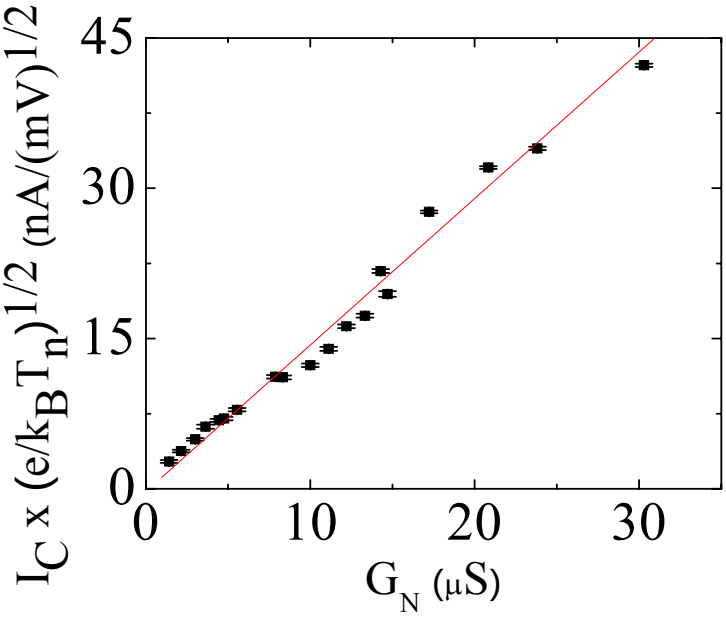

Figure 2-16 Plot of $I_C \times \sqrt{e/k_B T_n}$ vs. G_N of Pb/I/Pb STM junctions. The slope is equal to $I_C R_N \times \sqrt{e/k_B T_n}$. The line is a linear fit to the data. From the fitted slope and using the known value of $I_C R_N$ (Pb/I/Pb), T_n and Z_{ENV} are determined to be 15.9 ± 0.1 K and 279 ± 9 Ω, respectively.

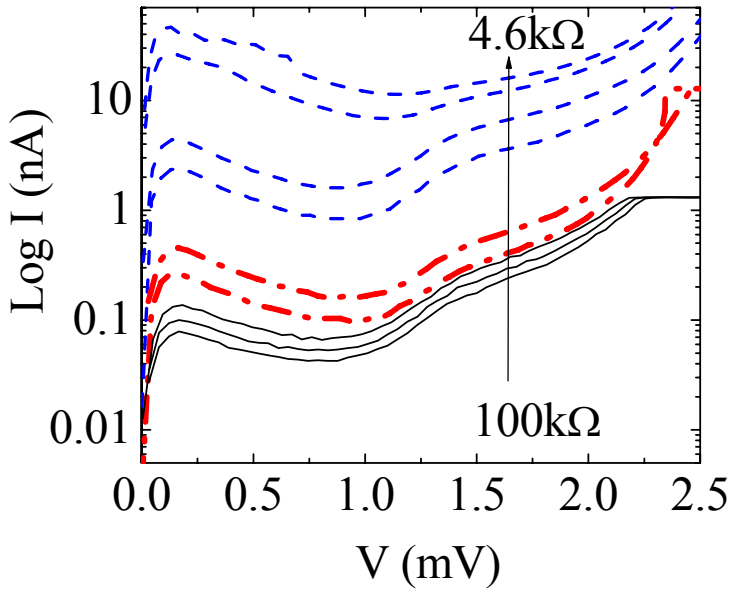

Figure 2-17 Phase diffusion branches for positive bias side of Pb/I/Pb STM junctions at T = 2.1 K. They are measured by three different gains of preamplifiers, 10^7 (dash), 10^8 (dash dot) and 10^9 (line). Note the tunnel current is plotted on a log scale and the amplitude of the thermally fluctuated Josephson current varies in nearly three orders of magnitude.

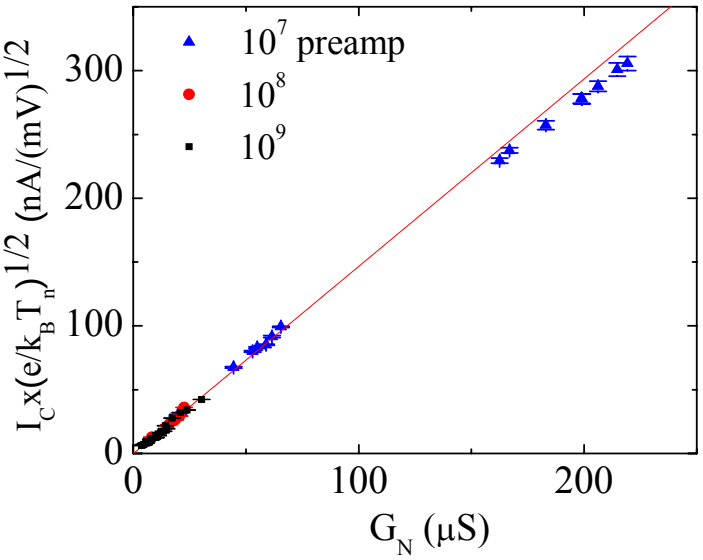

Figure 2-18 Plot of $I_C \times \sqrt{e/k_B T_n}$ vs. G_N obtained from the data represented in Figure 2-17 fitted to the phase diffusion model. All data fall into the single line, indicating T_n does not change by large current flowing through the tunnel junction.

(ii) Pb/I/$NbSe_2$ STM junctions

Once T_n and Z_{ENV} are determined from Pb/I/Pb STM Josephson junctions measurements, $I_C R_N$ for a new material can be obtained using the known values of T_n and Z_{ENV}. We choose 2*H*-$NbSe_2$ single crystal as a first target material and a surrogate to the high-T_C superconducting cuprates. 2*H*-$NbSe_2$, a family of layered transition-metal dichalcogenides, is a type-II conventional superconductor with T_C = 7.2 K and charge density wave (CDW) transition at T_{CDW} = 33 K, so the CDW state coexists with the superconducting state below T_C. This material also has short coherence lengths (ξ_a = 77 Å and ξ_c = 23 Å), an anisotropic *s*-wave gap varying from 0.7 to 1.4 meV across the Fermi Surface (Hess1991) and multiband superconductivity indicated from observations of momentum-dependent superconducting gap on the different Fermi surface sheet (Yokoya2001). Van der Waals bonding between Se layers is so weak that the crystal is easily cleaved to expose a fresh and inert surface for STM measurements. No Josephson tunneling measurements, however, have been reported before those of our group (Naaman2003), partly because it is difficult to grow a stable oxide layer for planar tunnel junctions. The data of Pb/I/$NbSe_2$ STM Josephson junctions are presented in Figure 2-19. The experimental data on the left panel (lines) are contributions from the thermally fluctuated Josephson currents after subtraction of the quasiparticle background due to thermally excited quasiparticles. The background is obtained from the *I-V* curves of high resistance junctions where no Josephson currents are observed. Figure 2-19 shows good agreement between the fits to the phase diffusion model (symbols) and the observed data. Since the slope value in Fig 2-20 is equal to $I_C R_N \times \sqrt{e/k_B T_n}$ along with the condition that T_n and Z_{ENV} remain constant, we can get a relation such as $\sqrt{k_B T_n/e}$ =

$I_C R_N$(Pb)/*slope*(Pb) = $I_C R_N$(Pb/$NbSe_2$)/*slope*(Pb/$NbSe_2$), where *slope*(Pb) is obtained from the linear-fit to the data in $I_C \times \sqrt{e/k_B T_n}$ vs. G_N plot of the Pb/I/Pb STM Josephson junctions shown in Figure 2-16. Substituting the known values, $I_C R_N$(Pb)/*slope*(Pb) and the measured *slope* (Pb/$NbSe_2$), we obtain $I_C R_N$(Pb/$NbSe_2$) = 1.39 ± 0.03 mV. Using the formula of the Josephson binding energy for different superconductors at T = 0 K and substituting $\Delta_1 = \Delta_{Pb}$ and Δ_2 for the smallest and average gap of $NbSe_2$, that is 0.7 and 1.1 meV respectively, into the equation (2-21) yields 1.34 meV < $I_C R_N$ (Pb/$NbSe_2$, T = 0 K) < 1.70 mV. Our result is in good agreement with the theoretical expectation.

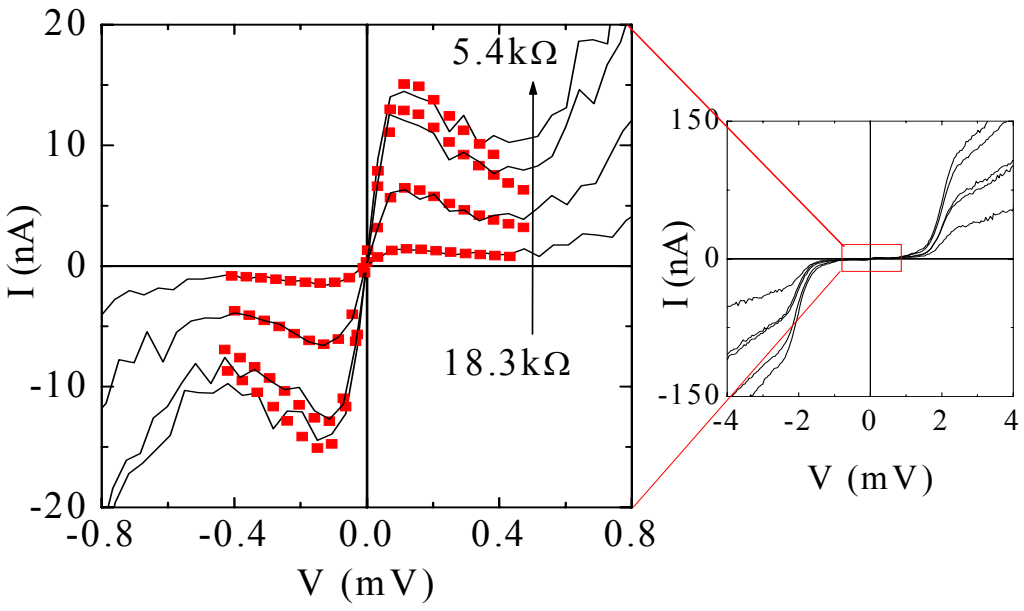

Figure 2-19 *I-V* characteristics of Pb/I/$NbSe_2$ STM junctions at T = 2.1 K. (Right panel) We can see a current rise at V = Δ_{Pb} + Δ_{NbSe2}. (Left) *I-V* characteristics zoomed near zero bias surrounded by a box in the right panel, showing thermally fluctuated Josephson current and the symbols represent two-parameter fits to the phase diffusion model.

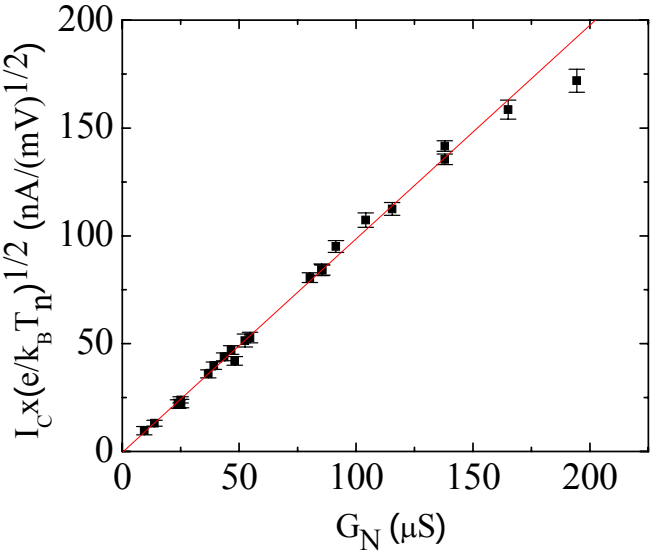

Figure 2-20 Plot of $I_C \times \sqrt{e/k_B T_n}$ vs. G_N of Pb/I/$NbSe_2$ STM junctions. The slope is equal to $I_C R_N \times \sqrt{e/k_B T_n}$. The line is a linear fit to the data. From the fitted slope and using the known value of T_n = 15.9 K, $I_C R_N$ (Pb/$NbSe_2$) is determined.

2-3-4 Pb (Nb)/I/$YBa_2Cu_3O_{7-\delta}$ ($Bi_2Sr_2CaCu_2O_{8+\delta}$) planar Josephson junctions (brief review)

The observation of strong *c*-axis Josephson coupling in planar Pb -$YBa_2Cu_3O_{7-\delta}$ (YBCO) single crystal Josephson junctions has been reported and was explained by an *s*-wave component in the order parameter of YBCO induced by an orthorhombic distortion (Sun1994a). Although the crystallographic symmetry of $Bi_2Sr_2CaCu_2O_{8+\delta}$ (BSCCO) makes *s*-and *d*-wave mixing less likely (Annett1990), Josephson couplings between conventional superconductors and BSCCO in planar junctions have been observed (Mößle1999, Kawayama1999). $I_C R_N$ values for these junctions (Nb - or Pb -BSCCO) ranged from 1 μV to 10 μV, indicating that the *s*-component is about three orders of magnitude smaller than the *d*-component. Because $I_C R_N$ was measured in macroscopic

junctions, any strong local inhomogeneities were obscured and meaningful comparisons with an inhomogeneous Δ could not be made. It is, therefore, very important to locally probe the order parameter in this strongly inhomogeneous material using Josephson tunneling.

2-4 Noise and cryogenic microwave copper powder filter

The original STM set-up for STM Josephson junctions had a very high noise temperature because high frequency noise from room temperature circuitry and pickup was unfiltered and thus propagated to the low temperature STM. From the *s*-wave/BSCCO planar Josephson junction measurements (Sun1994a, Mößle1999, Kawayama1999), the observed $I_C R_N$ were found to be around 10 μV. This raises serious challenges if we want to do local measurements on BSCCO. Assuming the phase diffusion branch observed in Pb/I/BSCCO STM Josephson junction is well fitted to the phase diffusion model, the thermally fluctuated pair current has a maximum at V_p and it is equal to $I(V_P) = (\hbar/8e)(I_C^2/k_B T_n)$. Using the minimum possible tunnel current resolved in our electronics being 5 pA and the typical lowest R_N ~ 30 kΩ, we can estimate the lowest $I_C R_N$ to be observable for a given noise temperature. From the simple calculation of $I_C R_N \geq R_N\sqrt{(8e/\hbar)k_B T_n I_{min}}$, for T_n = 15 K, $I_C R_N \geq$ 20 μV can be measured and for T_n = 10 K, $I_C R_N \geq$ 15 μV. Thus, we set as a goal a noise temperature T_n less than 10 K.

Several modifications of electronics have already been made (Naaman thesis). With the exception of the thermometer leads, all cables connecting the high vacuum feedthrough at the top of the cryostat (room temperature) to the STM stage (low temperature) were replaced by stainless steel miniature coaxial cables (Cooner wire

#CW3495). A special low noise coaxial cable (Endevco #26108) as well as a low noise rf miniature coaxial cable (Garg associates, India) were introduced for the tunnel current leads. Our STM has a design such that the tip is held at virtual ground while the bias voltage is applied to the sample connected to the chassis ground and the tunnel current is measured from the tip. This causes the tunnel current to be subject to noise from capacitive pick-up from, for example, the high and rapidly sweeping voltage on the scan piezo. Therefore it is necessary to use individually shielded coaxial cables to prevent capacitive cross talk and it is necessary to place a ground plate between the tip and the scan piezo. The stainless steel coaxial cables and a 10 : 1 voltage divider in parallel with a 10 nF capacitor mounted directly on the STM stage serve as effective low pass filters with a cutoff frequency of 100 kHz.

Furthermore two cryogenic copper powder filters were mounted near the STM stage inline with the bias and tunnel current leads (Naaman thesis), resulting in T_n reduction to 33 K. The copper powder filter on the bias voltage lead, however, did not have sealed connection so that electromagnetic leakage from exposed wire connections would elevate the noise temperature. The microwave filter design was modified at the bias voltage lead to use SMA connectors to minimize the radiation leakage. The powder filters originally invented by Martinis *et al.* (Martinis1987) are essentially a resistive coil embedded in an environment of closely packed copper (Cu) grains in an insulating matrix. The Cu powder function in two ways — first, they have very large surface area, so that skin effect damping becomes appreciable at frequencies where the skin depth in Cu is smaller than the grain size. Secondly, the packing of metallic particles around the

coil increases the capacitance between the coil and ground. The resistive coil thus also acts as a distributed RC line.

The coil core is made as follows: low viscosity clear epoxy, Stycast 1266 A/B is mixed with the mixing ratio 3 : 1 of parts A : B by volume. Cu powder of 50 μm diameter is mixed with a ratio of 2 : 1 of Cu : Stycast by weight. The mixture is placed in vacuum to remove air bubbles trapped during mixing. The mixture is then injected into a thin wall teflon tubing (AWG 14) and is left to cure overnight with tension applied to the tubing. The teflon tubing is removed to take the mixture out and cut into a core with 1.5" long. 3 ~ 4 feet of annealed manganin 290 resistive wire of 0.005" diameter with heavy formvar coating is wound around the core to form a resistive coil. These coils are then placed in filter housings to be potted with a fresh Cu/Stycast mixture. The filter body is machined 2" long OFHC copper rods with 0.5" side square cross section to make 3/8" bore drilled along the length. SMA connectors are soldered to the end of the coiled wire and attached to the filter housing securely to seal. Since the Cu powder is very weakly conductive even when compacted in the Stycast, we left the inner conductor of the SMA connector exposed. These filters are directly mounted on the STM stage so that any electromagnetic radiation or thermal noise from room temperature will be absorbed in the filter which is thermally anchored to the STM at the experimental base temperature. Their resistance is ~ 50 Ω and capacitance ~ 150 pF.

Figure 2-21 shows the transmission coefficient S_{21} of one of these Cu powder filters using a network analyzer (a courtesy of Clarke group). The signal is attenuated by 30 dB at 200 MHz, and ~ 100 dB at 2 GHz. Combining the cryogenic microwave filters

along with effective RC filters, the current value of T_n is lowered to be 15 K as derived in the preceding section.

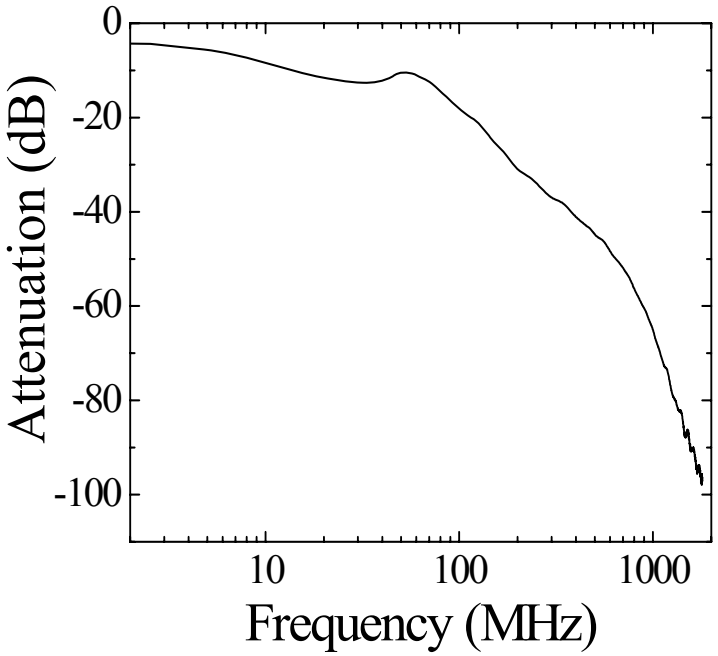

Figure 2-21 Transmission coefficient S_{21} of one of the Cu powder filters measured at room temperature.

Chapter 3 Experiments and Interpretations

3-1 Motivation

In the previous chapter we have shown that Pb/Ag coated STM tips can be reproducibly fabricated and Josephson coupled. Using a well-characterized superconducting STM, we could deduce the Josephson $I_C R_N$ products of the layered conventional superconductor, $NbSe_2$ with a Pb/Ag tip, and found it to be in good agreement with the theoretical prediction. It is worth noting again that the $I_C R_N$ product is related to the amplitude of the superconducting pair wave function, $|\Psi|$. For conventional superconductors we can calculate this quantity with a value of the energy gap obtained from quasiparticle tunneling measurements and using the Ambegaokar-Baratoff formula. For unconventional (including high-T_C materials) superconductors we do not have an established theory connecting the energy gap to $|\Psi|$. Moreover there is an ambiguity in the definition of the energy gap in the quasiparticle density of states (DOS) of high-T_C superconductors, especially for underdoped samples where there no longer exists sharp coherence peaks to determine the energy gap. The superconducting STM can probe the pair wave function amplitude directly on a length scale of nanometers, which makes it a very powerful tool to study the inhomogeneity of a material such as $Bi_2Sr_2CaCu_2O_{8+\delta}$ (BSCCO) which has a very short superconducting coherence length.

As addressed in the Introduction (chapter 1), there is still controversy about the symmetry of the order parameter of high-T_C superconducting cuprates and whether the pseudogap state observed in the underdoped region is a precursor to the coherent superconducting state. If the symmetry is strictly *d*-wave, there should exist no Josephson

coupling between high-T_C superconducting cuprates and the conventional superconducting tip. Thus Josephson measurements on BSCCO using a superconducting STM can tell us about the symmetry of the BSCCO order parameter as well. Correlations between $I_C R_N$ products from the Josephson effect and the energy gap Δ measured from the quasiparticle excitation spectra of BSCCO has never been studied. This study will help in the construction of a microscopic theory of the mechanism of high-T_C superconducting cuprates. Another issue arising from a previous study at high STM currents on BSCCO (Howald2001) is that there was a threshold current value above which the BSCCO morphology and spectroscopy were drastically and irreversibly changed. This occurred at around 500 pA. Care will be taken to sweep the bias of the STM junction such that the resulting tunneling current does not exceed this threshold and so avoid changing the BSCCO electronic structure. In order to carry out experiments along this outline, our experimental procedure is as follows:

3-2 $Bi_2Sr_2CaCu_2O_{8+\delta}$

BSCCO single crystal used in this thesis work were grown by the floating zone method (Ono2003) with the hole doping, δ_h, ranging between heavily underdoped (T_C = 64 K) and overdoped (T_C = 74 K) via optimally-doped samples (T_C = 94 K). T_C was determined by magnetic susceptibility measurements. Extensive Josephson measurements were done on overdoped samples with different dopings (T_C = 76, 79 K and 81 K). BSCCO samples which have a typical dimension of 1 mm × 1 mm and a few tens of μm thick are glued on to a copper plate by silver epoxy (Epoxy technology EE 129-4). The epoxy was baked at 100 degree C for 15 minutes to assure good electrical conductivity.

All the samples were cleaved in ultra high vacuum (~ 3×10^{-8} Torr) using Scotch electrical tape at room temperature. The cleaving method itself is very simple – the scotch tape 2 mm long is put on the crystal such that 1 mm of the tape remains unattached. Then a 0.005" Phosphor-bronze T-shaped slab with double-sided scotch tape was placed on the crystal and the unattached end of the tape was folded down to touch the double-sided scotch tape on the bronze "T". A schematic of the cleaving stage is shown in Figure 3-1. By hitting the bottom of the "T", the sample was cleaved to expose a fresh surface.

Figure 3-2 is the crystal structure of BSCCO where BiO-BiO planes are bonded by weak Van der Waals bonding so that it is most likely the cleavage plane (Pan1998), and the conducting CuO_2 surface is two layers below the BiO plane. Cleaved samples are then cooled to $T = 2.1$ K after being inserted into the STM. Since BSCCO has a layered structure and is flaky, we used a very slow tip approach to prevent the tip from picking up small flakes of BSCCO. Figure 3-3 is the atomic resolution image of optimally-doped BSCCO scanned by the superconducting STM tip at $T = 2.1$ K. We can clearly see Bi atoms. Because of the thick Pb layer used in our superconducting tip fabrication, it is difficult to obtain the atomic resolution images routinely. However we can easily locate step edges and isolate flat surfaces where all the present data were obtained.

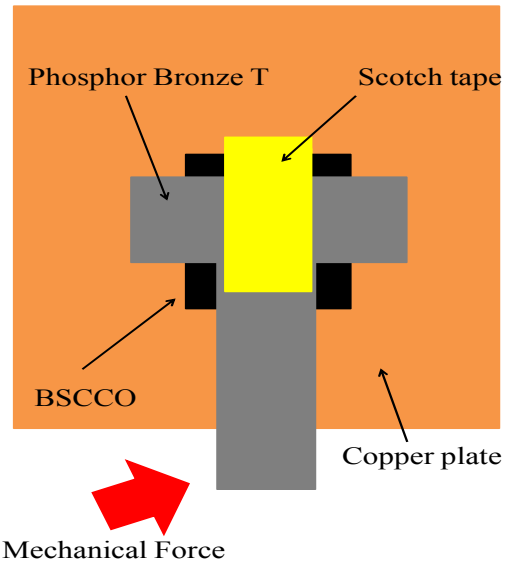

Figure 3-1 Schematic of cleaving BSCCO single crystal

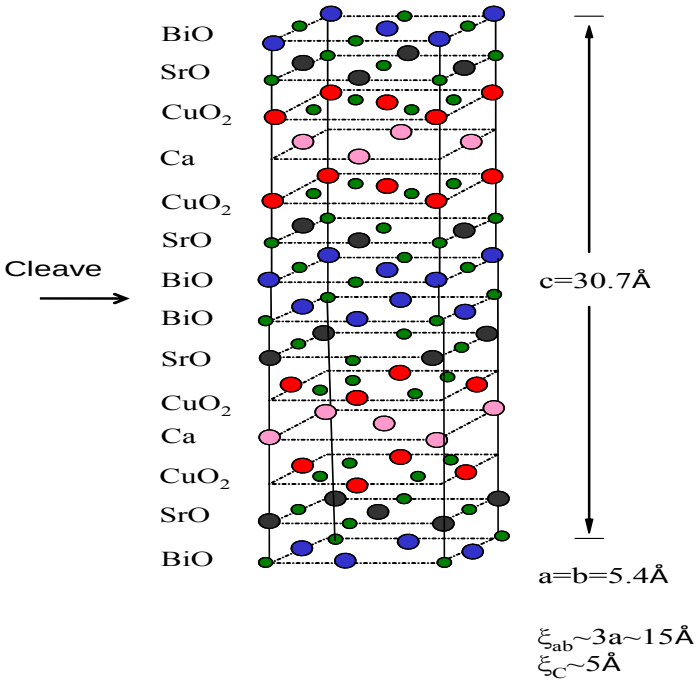

Figure 3-2 Crystal structure of BSCCO

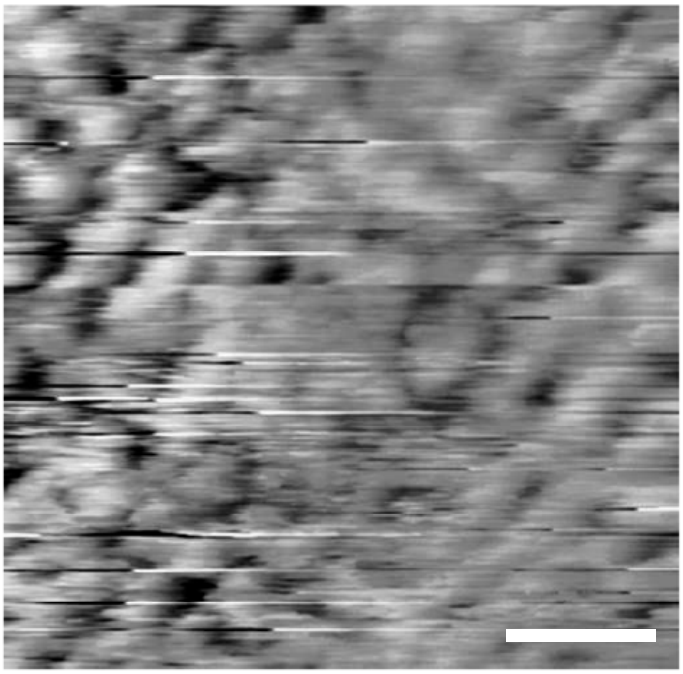

Figure 3-3 Optimally-doped BSCCO topography scanned by superconducting STM tip at T = 2.1 K. White bar is equal to 10 Å.

It is well known that dI/dV curves measured on the BiO surface show sharp coherence peaks with electron-hole asymmetry and finite tunneling conductance all the way to the Fermi energy (see Figure 2-8(b)). Previous work has shown dI/dV measurements on the CuO_2 plane which is rarely exposed. These measurements show a wider energy gap than those typically measured on the BiO plane, as well as a strong suppression of the density of states (DOS) within 10 meV of the Fermi energy, and a homogeneous gap distribution over the surface (Misra2002). It is claimed that this is probably due to oxygen escaping from the CuO_2 layer as it is not protected by BiO and SrO layers anymore. This causes the doping level on the exposed CuO_2 plane to be different from that of the bulk sample. Most of the dI/dV spectra measured for this thesis research showed sharp coherence peaks and we observed substantial inhomogeneity of

the energy gap over the surface. We have concluded that our local Josephson and spectroscopic measurements have been performed on the BiO plane.

3-3 *C*-axis Josephson coupling between a conventional superconducting STM tip and optimally-doped/overdoped $Bi_2Sr_2CaCu_2O_{8+\delta}$ single crystals

We first observe the dI/dV spectrum at a particular surface point on overdoped BSCCO (T_C = 79 K) to measure the energy gap Δ (black line in the inset of Figure 3-4). We use standard Lock-in techniques with 1 kHz modulation and the modulation voltage (2.5 mV_{RMS}) on the bias voltage and a junction normal resistance, R_N ~ 500 MΩ. Although it is clearly a simplification of a more complex structure, we use the same definition for Δ as in previous works (Fischer2007 and references therein) in order to make comparisons. We have to decrease R_N to enhance the Josephson binding energy, E_J in order to observe the pair tunnel current as we did in the Pb/I/Pb STM junctions. A difference is that we cannot go to very large current in BSCCO due to the current limits for BSCCO damage mentioned above. This is also true for determining R_N. Since the energy gap of BSCCO is much larger than that of Pb it is more difficult to measure R_N from the *I-V* curves because of the limits of current. Our procedure to determine this is to record several *I-V* curves by sweeping the bias voltage above the Pb gap. Then R_N is determined by making use of our knowledge that the junction normal resistance inside BSCCO gap (above the Pb gap) is 3 ~ 4 times larger than that outside the BSCCO gap determined from the dI/dV spectrum such as illustrated in the inset of Figure 3-4. For the lower junction resistance *I-V* curves, R_N was calculated from the factor required to scale the current so that it overlaps with already normalized $I(V)R_N$ vs. V curves with the

ratio of the conductance inside to that outside the BSCCO gap. A set of dI/dV for BSCCO gap and *I-V* curves taken with progressively lower junction resistances are necessary to calculate the $I_C R_N$ product every time the tip is moved to a new location.

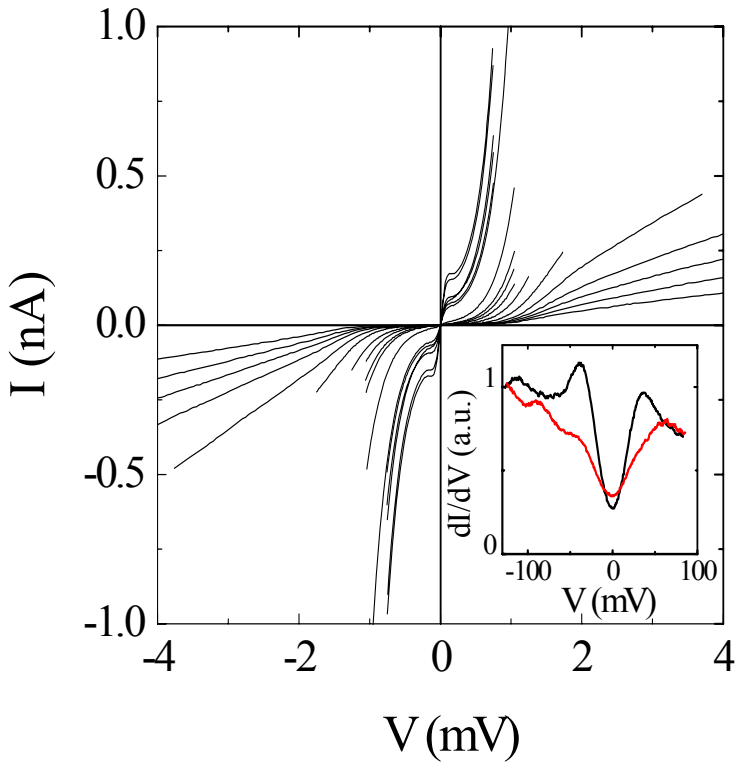

Figure 3-4 *I-V* characteristics of Pb/I/overdoped BSCCO (T_C = 79 K) STM Josephson junctions at T = 2.1 K. The Pb gap is clearly seen around V = 1.4 mV. Inset: dI/dV spectrum (black line) measured before low R_N measurements, showing sharp coherence peaks with Δ = 37 meV. dI/dV spectrum measured after low R_N measurements (red line) indicates an LDOS change due to high current density.

In the main frame of Figure 3-4 we plot the *I-V* characteristics at lower bias and lower R_N. A low leakage current below the Pb gap confirms the high quality of the vacuum tunnel junctions. Further decreasing R_N increases the quasiparticle tunneling probability and finally the contribution from the thermally fluctuated Josephson currents

is observed when E_J is comparable to $k_B T_n$ (Kimura2008). The quasiparticle background inside the Pb gap is much larger than that of Pb/I/Pb STM Josephson junctions because of the gaplessness of the local density of states (LDOS) of BSCCO, *i.e.,* the existence of quasiparticle states all the way down to the Fermi energy.

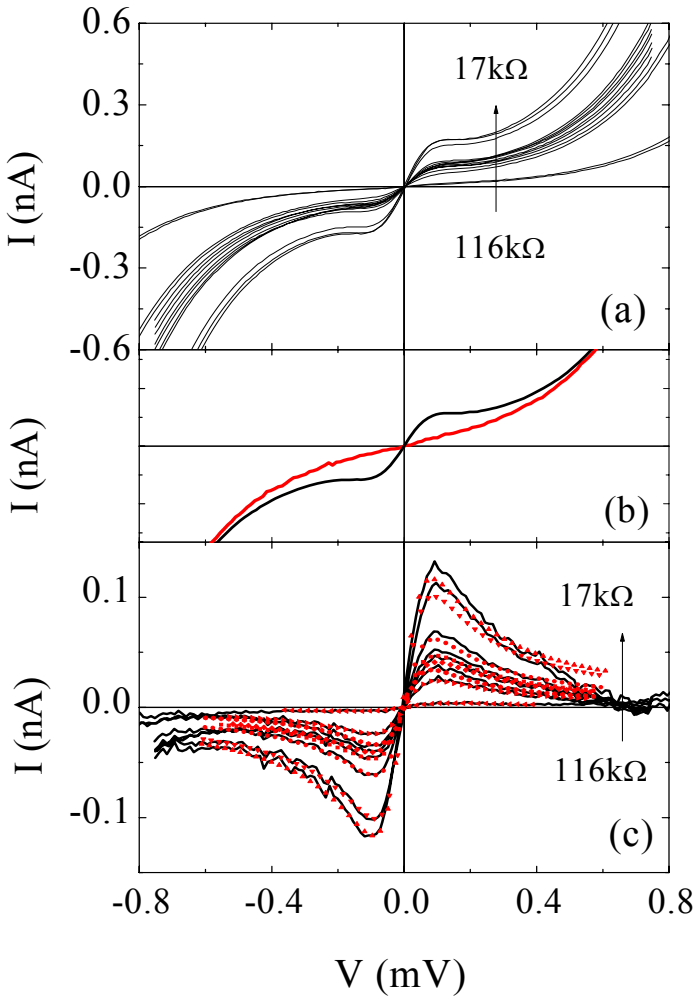

Figure 3-5 (a) Low bias *I-V* characteristics of Figure 3-4 for various junction resistances at $T = 2.1$ K. (b) Averaged *I-V* characteristic near zero bias for quasiparticle background (red line). One of the observed *I-V* curves is shown by the black line. (c) Thermally fluctuated Josephson currents peaked at V_P as derived by subtracting quasiparticle background (Figure 3-5b) from the *I-V* curves (Figure 3-5a). The data are represented by the lines and the symbols represent two-parameter fits to the phase diffusion model.

Figure 3-5(a) displays a close-up view of the *I-V* characteristics near zero bias, clearly showing that the superconducting Pb tip was Josephson coupled to the BSCCO. The quasiparticle background represented by the red line in Figure 3-5(b) is obtained from an average of several normalized *I-V* curves without the phase diffusion branches as described above. Figure 3-5(c) shows the contributions from the thermally fluctuated Josephson current after subtracting the quasiparticle background of Figure 3-5(b) from the *I-V* curves of Figure 3-5(a). The data in Figure 3-5(c) are shown as lines and the best fits to the equation (2-40) (Ivanchenko-Zil'berman formula described in chapter 2) are represented by the symbols. These good fits convince us that we have observed the pair current between a conventional (*s*-wave) superconducting Pb tip and overdoped BSCCO. This suggests that the BSCCO does not have a pure *d*-wave order parameter. In addition, the dI/dV spectrum represented by the red line in the inset of Figure 3-4 was observed after the low R_N measurements in Figure 3-5. The LDOS was changed significantly during the measurements; and the quasiparticle coherence peaks have disappeared, perhaps due to the high current density of the measurements at the highest conductance studied. This dI/dV curve resembles those previously observed in heavily underdoped BSCCO (McElroy2005a, Gomes2007, Aldredge2008), in the "pseudogap" state at temperatures above T_C (Renner1998a, Gomes2007) and, in strongly disordered BSCCO thin films (Cren2000). It is also similar to the dI/dV spectra observed by others on surfaces which were altered by scanning with large tunnel currents (Howald2001). It is important to note that LDOS changes were observed only when measurements were made with R_N below 30 kΩ and I above the threshold current around 500 pA. Moreover the Josephson current disappeared after these irreversible changes of the LDOS on

BSCCO occur. In order to avoid this effect, most of the data presented here were obtained with R_N ranging from 30 kΩ to 100 kΩ. This will be discussed in subsequent sections.

Each fit to the Josephson portion of the *I-V* curves in Figure 3-5(c) generates a single data point in the plot shown in Figure 3-6 in the similar way as described in Pb/I/Pb and Pb/I/$NbSe_2$ STM junctions results. As G_N is increased (R_N is reduced) the observed I_C increases (E_J increases). Using the previously determined T_n and Z_{ENV} for this experimental apparatus, and taking the slope of the linear fit shown in Figure 3-6, we find $I_C R_N$ at this surface point to be 335 μV.

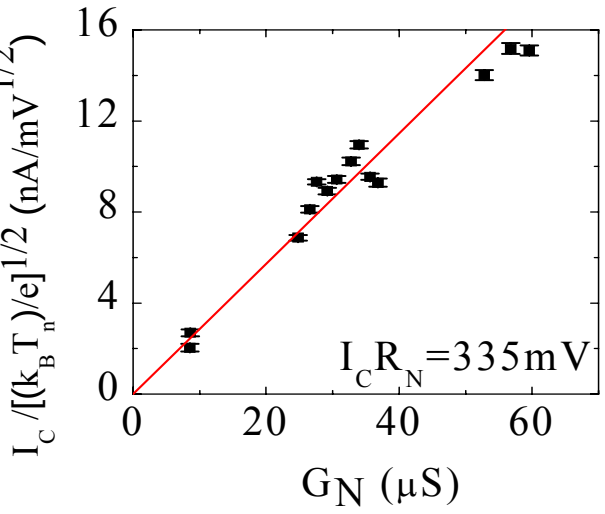

Figure 3-6 Plot of $I_C \times \sqrt{e/k_B T_n}$ vs. G_N of Pb/I/overdoped BSCCO (T_C = 79 K) STM Josephson junctions. The slope is equal to $I_C R_N \times \sqrt{e/k_B T_n}$. Using the fitted slope and substituting the previously determined T_n, the Josephson product at this surface point is found to be $I_C R_N$ = 335 μV.

The Josephson coupling was also observed on optimally-doped BSCCO (T_C = 94 K). Figure 3-7 clearly shows the Pb gap and the thermally fluctuated pair currents at

lower R_N. An I_CR_N was derived to be 33 μV (Figure 3-8). In the next section, spatial studies of I_CR_N and its relation with Δ for overdoped samples are described in detail.

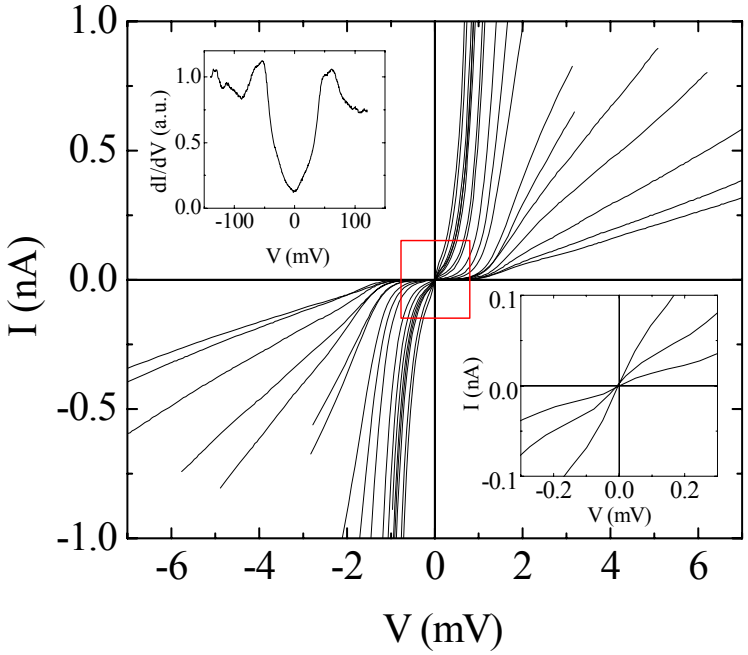

Figure 3-7 *I-V* characteristics of Pb/I/optimally-doped BSCCO (T_C = 94 K) STM Josephson junctions at T = 2.1 K. The Pb gap is also clearly seen around V = 1.4 mV. Inset: (upper left) typical dI/dV spectrum measured on this sample before low R_N measurements with Δ = 53 meV. (lower right) Several *I-V* characteristics near zero bias showing the pair current contribution.

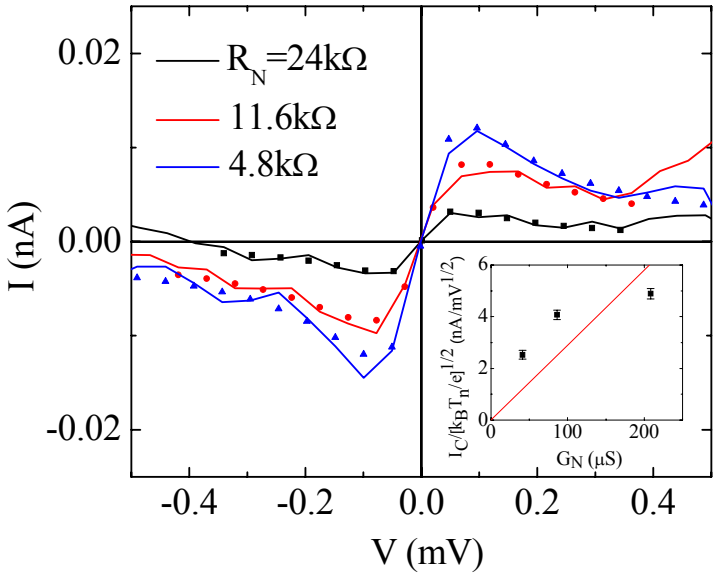

Figure 3-8 *I-V* characteristics of Pb/I/optimally-doped BSCCO (T_C = 94 K) STM Josephson junctions near zero bias. Inset: Lines represent pair currents subtracting quasiparticle background from *I-V* curves in lower right inset of Figure 3-7 and dots represent fits to Ivanchenko-Zil'berman formula. Inset: Plot of $I_C \times \sqrt{e/k_B T_n}$. $I_C R_N$ = 33 μV.

3-4 Scanning Josephson tunneling studies of overdoped $Bi_2Sr_2CaCu_2O_{8+\delta}$ single crystals

There are several normal metal STM studies of BSCCO aimed to develop a map of electronic quantities of this material. Several of these are referred to as "gap map" (Fischer2007). These images revealed inhomogeneous structure of the energy gap (Lang2002), periodic electronic modulation inside vortex cores (Hoffman2002a) and in the pseudogap state (Vershinin2004). They were, however, derived from quasiparticle excitation spectra, not probing the superconducting ground state itself. It is very natural to ask (i) whether the superconducting order parameter of BSCCO has spatial variation, and (ii) how the superconducting ground state correlates with the quasiparticle excited

states (Δ). Since high energy resolution spectroscopy was performed on overdoped BSCCO (T_C = 79 K) in Figure 3-5, we moved the tip to measure I_CR_N and Δ at a different location. For the spatial measurements of I_CR_N and Δ, the lowest junction resistance was kept above 30 kΩ because we have already seen the LDOS change for higher currents (in Figure 3-4). The result is presented in Figure 3-9. Unlike the case of Figure 3-4, the inset of Figure 3-9(a) shows the LDOS does not change after the *I-V* characteristic measurement at the lowest R_N and the energy gap, Δ derived from the coherence peaks remain the same as that observed before the low R_N measurements. We found Δ = 47 meV at this surface point. I_CR_N is also different from the previous location. It is observed that the LDOS change due to high current density also caused spatial degradation of the superconducting LDOS, therefore we have to make sure the BSCCO gap remains the same after the low R_N measurements at each point in order to carry out spatial studies of I_CR_N.

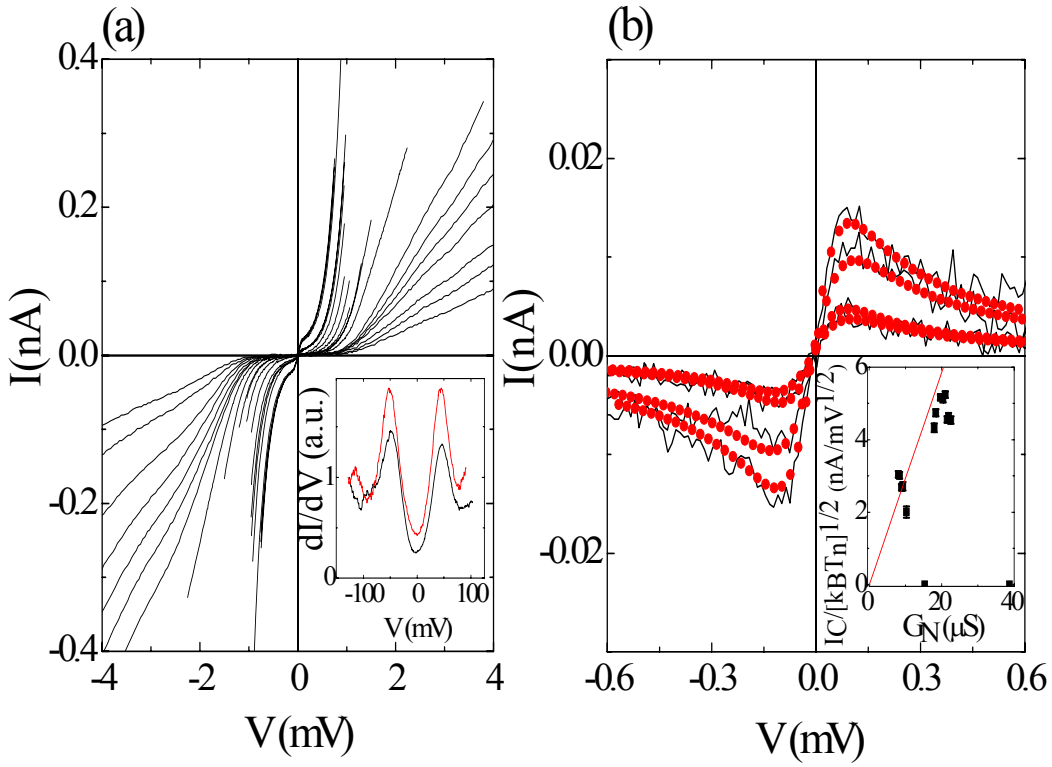

Figure 3-9 *I-V* characteristics of Pb/I/overdoped BSCCO (T_C = 79 K) STM Josephson junctions at different location from that in Figure 3-4. (a) *I-V* characteristics of Pb/I/overdoped BSCCO (T_C = 79 K) STM Josephson junctions at T =2.1 K. Inset: dI/dV measured before low R_N measurement (black line) and after it (red line). Note that energy gap is unchanged. (b) Thermally fluctuated Josephson currents (lines) and fits (dots) to the phase diffusion model. Inset: Plot of $I_C \times \sqrt{e/k_B T_n}$ vs. G_N. $I_C R_N$ = 279 μV. Two data points at G_N = 15 and 39 μS correspond to *I-V* characteristics without any pair current observed.

Before proceeding on studies of the spatial dependence of $I_C R_N$ and the energy gap Δ, we want to note two data points showing zero I_C appearing in the $I_C R_N$ plot of Figure 3-9(b). The disappearances of I_C are observed at G_N = 15 and 39 μS (*I-V* curves without any Josephson contributions). In order to check reproducibility of the pair current, we first repeated measuring the Josephson current at the same R_N when it was observed at a particular R_N. We also checked a linearly increasing of I_C with G_N as well as

the linearly decreasing of I_C when G_N is decreased. The reproducibility was observed, however, sometimes I_C disappeared. Figure 3-10 shows the I_CR_N plot of Pb/I/overdoped BSCCO (T_C = 76 K) measured at T = 2.1 K. We first measured the *I-V* characteristic for the BSCCO gap (solid line in Figure 3-10(a)). Then R_N was decreased to see the Josephson current on the *I-V* characteristics. In Figure 3-10(b), each Josephson measurement is labeled in the chronological order in which it was taken. The Josephson coupling increases as we decrease R_N (expected) but then unexpectedly disappears at a lower R_N (label 5)! Increasing R_N (decreasing G_N) results in the Josephson coupling returning (labels 6 and 7). This behavior is all unexpected. After the low R_N measurements the *I-V* curve with a large bias was taken to observe the BSCCO gap. The observed curve (red dots) in Figure 3-10(a) indicates that LDOS of the BSCCO and the energy gap remains the same before and after the low R_N measurements so that the disappearance of I_C was not caused by the LDOS change due to the high current density.

Although the origin of this disappearance is still under investigation, we observe that low R_N measurements (R_N below ~ 300 kΩ) on BSCCO, increases the low frequency noise on the tunnel current. This noise appears to be induced locally on the BSCCO and not from the environment or the electronics. We assured ourselves that we have not affected the tip during the measurements by verifying that the Pb gap is always reproduced and the exponential decrease of the tunnel current vs. the tip-sample distance is also observed after low R_N measurements.

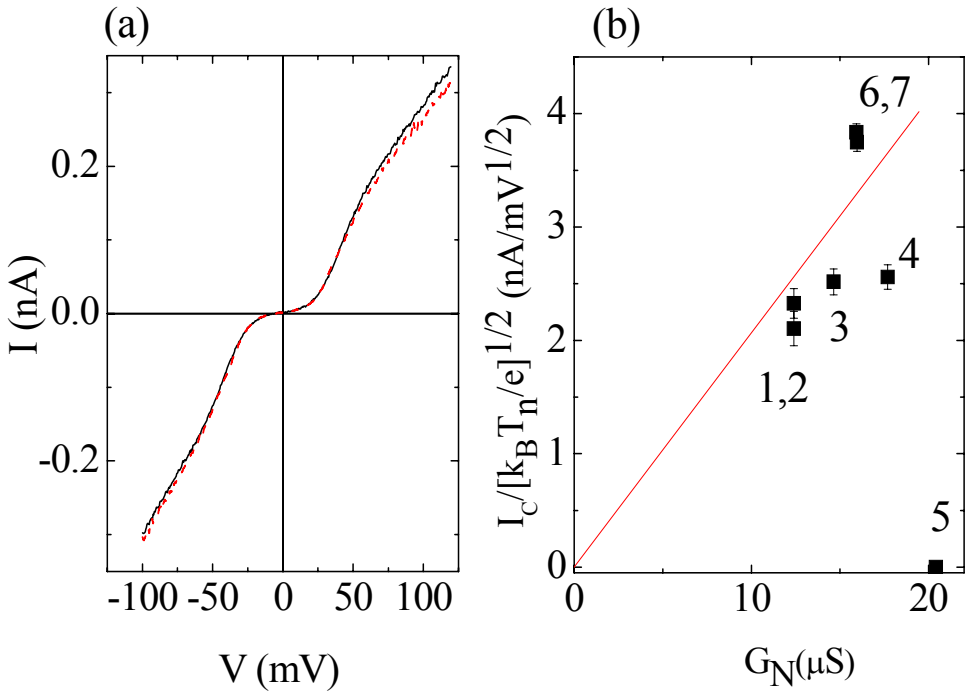

Figure 3-10 *I-V* characteristics and $I_C R_N$ plot of Pb/I/overdoped BSCCO (T_C = 76 K) STM Josephson junction for studying reproducibility of I_C. (a) *I-V* curve (black line) measured before low R_N measurements, showing Δ = 40 meV. *I-V* curve measured after low R_N measurements (red dots), indicating that the energy gap at this surface point remained the same. (b) Plot of $I_C \times \sqrt{e/k_B T_n}$ vs. G_N. The number labels represent the chronological order of the data sets. This order clearly shows the Josephson currents disappearing (5) and reappearing (6 and 7). Data points of (1,2) and (6,7) were measured repeatedly at R_N = 80 and 63 kΩ, respectively.

Keeping these facts in mind, we performed the local Josephson and spectroscopic measurements on the overdoped BSCCO surface. Figure 3-11 shows the spatial dependence of the energy gap and $I_C R_N$ measured simultaneously every 5 ~ 10 Å on a particular region on the surface. It clearly indicates that $I_C R_N$ and therefore the superconducting pair wave function of BSCCO changes on a nanometer-length scale on the surface. More interestingly, we can see an anticorrelation between Δ and $I_C R_N$ such that $I_C R_N$ tends to be reduced as Δ increases. The tendency was also observed in the data

taken along a line of 100 Å on another overdoped BSCCO (T_C = 76 K) sample. This relation can be seen more apparently when I_CR_N is plotted in the next section as a function of Δ for a variety of experiments.

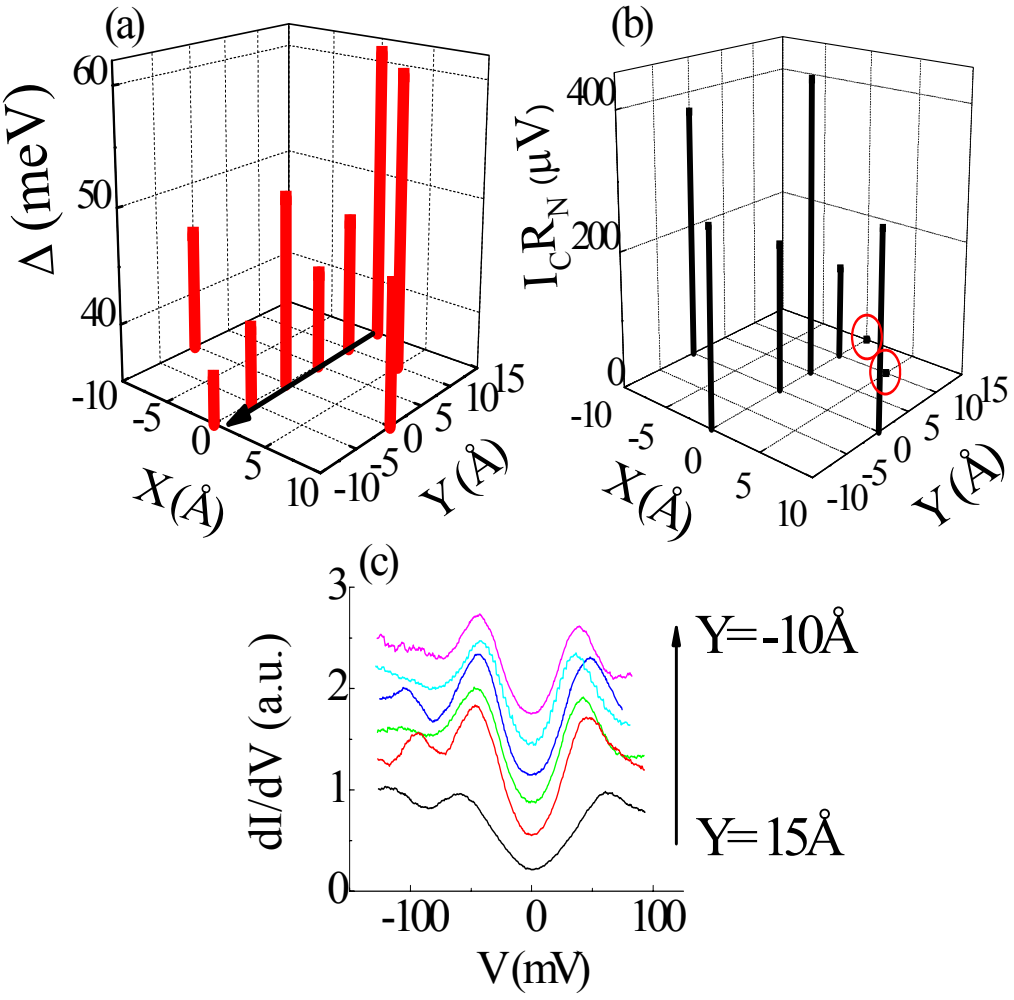

Figure 3-11 Spatial studies of Δ and I_CR_N on overdoped BSCCO (T_C = 79 K). I_CR_N in (b) changes spatially and seems to anticorrelate Δ. Note that no Josephson contributions on *I-V* characteristics were observed at the surface points denoted by red circles where the largest energy gaps were measured in this 20 Å × 25 Å region. (c) The line-cut of dI/dV spectra are measured along the arrow in (a), showing a well-known gap inhomogeneity (offset for clarity).

3-5 Inverse relation between I_CR_N and Δ of overdoped $Bi_2Sr_2CaCu_2O_{8+\delta}$ single crystals

Figure 3-12 summarizes our measurements of the Josephson I_CR_N product vs. Δ for five overdoped samples with each data point taken at locations roughly 5 ~ 10 Å apart (Kimura2008). Although there is scatter in the observed I_CR_N values for a given Δ, this figure clearly indicates the nanometer scale inhomogeneities in both I_CR_N and Δ. The reason for the scatter from experiment to experiment is under investigation. A surprising feature seen from this plot is that I_CR_N tends to be a maximum when Δ is between 40 and 45 meV, and the trend is for it to decrease or become zero as Δ increases or decreases from this maximal point. What does this relation, especially the inverse relation on the larger gap side mean? We will investigate the physics of this inverse relation next.

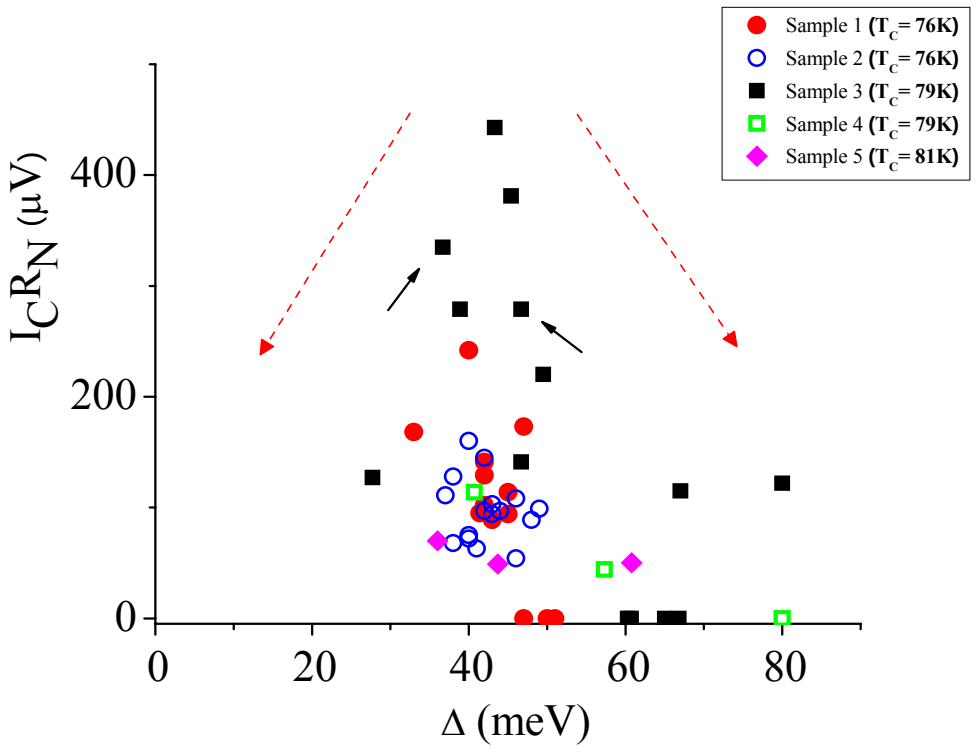

Figure 3-12 I_CR_N as a function of Δ. Each data point represents a separate measurement from a different location over 5 different samples. The I_CR_N values derived from Figure

3-6 and 3-9 are black square symbols denoted with line arrows. All other points are derived similarly. $I_C R_N$ appears to be a maximum for Δ between 40 and 45 meV, while it decreases for larger and smaller Δ. Dash arrows are guides to eye for this tendency.

3-6 Phase fluctuation model for phase diagram of high-T_C superconducting cuprates

We interpret these results within the framework of the phase diagram for high-T_C superconducting cuprates proposed by Emery and Kivelson (Emery1995). The following discussion uses Figure 3-13. High-T_C superconducting cuprates are doped Mott insulators with low superfluid density, n_S. Therefore, the phase stiffness which is the energy scale to twist the phase is small in these superconductors such that phase fluctuations could play an important role in determining T_C. There are two possible temperature scales that could affect the transition to superconductivity. T_θ is a temperature at which the phase ordering disappears. Another temperature scale, T^* is described as the temperature below which a gap on the quasiparticle spectrum appears. On the low doping side, a system could be divided into regions where the order parameter is well defined *locally* but not globally. This area becomes larger with increasing doping, resulting in stronger inter-granular coupling so that the phase coherence length becomes longer and less susceptible to phase fluctuations. T_θ is increased as the hole doping, δ_h increases, leading to a rise of the global T_C of the sample. Meantime, T^* continues to decrease as δ_h increases. At the optimal doping, T_θ and T^* cross over, so that the whole sample region is now phase coherent but the mean field value (energy gap) of the sample is suppressed by T^*. Thus T_θ and T^* are the upper-bounds to T_C. T_θ is more significant due to the phase fluctuations on the lower doping side (underdoped), while T^* is more important on the higher doping side (overdoped). Figure 3-13 plots T_C vs. hole doping, δ_h based on this Emery-Kivelson

model and the superconducting region forms a dome shape with the maximum T_C at $\delta_h \sim 0.16$ (optimally-doped). Decreasing or increasing δ_h from this value results in a T_C decrease.

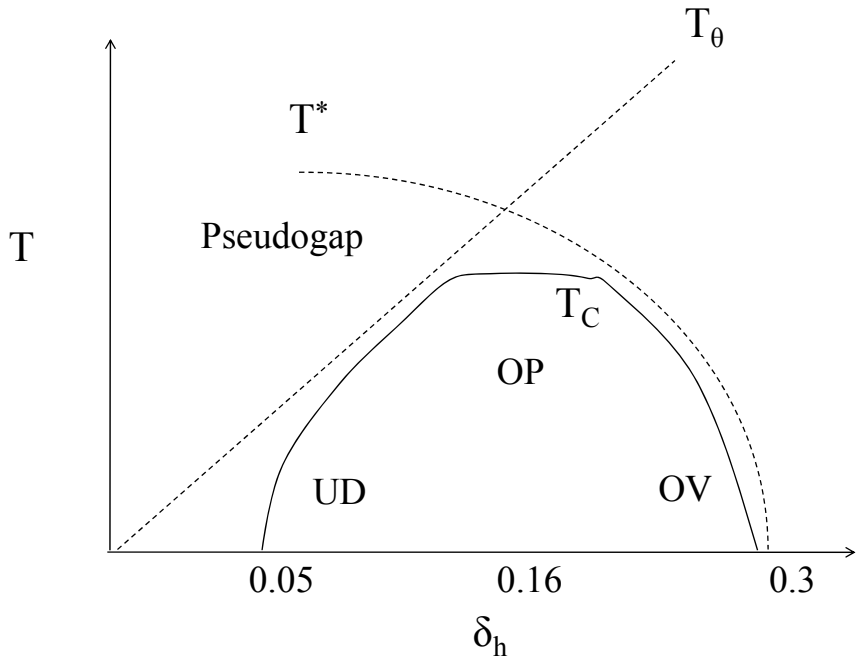

Figure 3-13 Phase diagram based on the phase fluctuation model of high-T_C superconductors as functions of temperature T and hole doping, δ_h proposed by Emery and Kivelson. Optimally-doped (OP) region is a cross over from underdoped (UD) to overdoped (OV) region. The phase ordering temperature, T_θ, and the mean field transition temperature, T^*, are defined in the text.

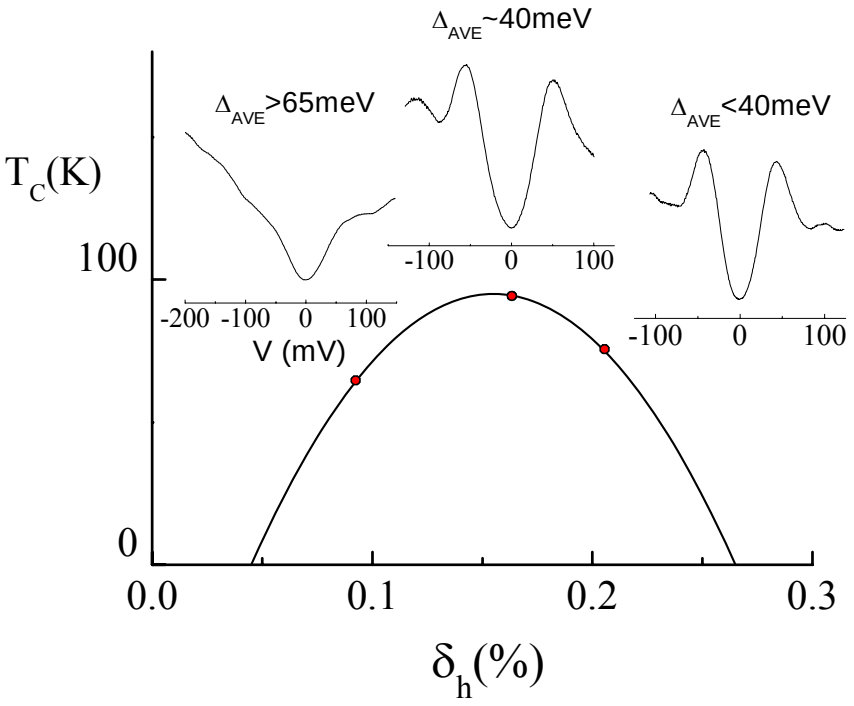

Figure 3-14 Typical dI/dV spectra and the corresponding averaged energy gaps, Δ_{AVE} at T = 2.1 K for BSCCO with three different dopings. They are underdoped (T_C = 64 K), optimally-doped (T_C = 94 K) and overdoped (T_C = 76 K) samples. Note that Δ_{AVE} monotonically decreases as δ_h is increased.

3-7 Interpretation of the inverse relation between $I_C R_N$ and Δ of "overdoped" $Bi_2Sr_2CaCu_2O_{8+\delta}$ single crystals

In order to interpret our results using the Emery-Kivelson model (T_C vs. δ_h), we make two assumptions in order to replace δ_h in their model by the energy gap, Δ which we actually measured in our experiments (Kimura08). First of all, T^* changes monotonically with δ_h and decreases as δ_h increases. Previous STM studies (McElroy2005a, Aldredge2008) reported the spatially averaged gap value monotonically increased from overdoped (the average $\Delta \leq 40$ meV) to underdoped (the average $\Delta \geq 60$ meV), and dI/dV with $\Delta \geq 65$ meV is often observed in heavily underdoped samples to no longer exhibit sharp coherence peaks. We also measured three different doping

samples, underdoped (T_C = 64 K), optimally-doped (T_C = 94 K) and overdoped (T_C = 76 K) and observed this tendency as shown in Figure 3-14, indicating that the average Δ, Δ_{AVE} seems to monotonically increase as δ_h is decreased. It was reported that the formation of gapped regions obtained from the dI/dV spectra actually started above T_C and there is a linear relation between Δ and the gap opening temperature, T^* for optimally-doped and overdoped BSCCO samples (Gomes2007). Combining with all these facts, we note that the δ_h-axis in the Emery-Kivelson model can be transformed into the Δ-axis, but now T^* monotonically increases with Δ_{AVE} as shown in Figure 3-15.

Second, McElroy *et al.* (McElroy2005a) reported that all the gap-map studies for different dopings, ranging from underdoped to overdoped, show not only strong gap inhomogeneity (observation of the larger gap in regions of the overdoped and that of the smaller gap in regions of the underdoped samples), but also the shape of the averaged dI/dV spectra for a given gap seems to be very similar, independent of whether the bulk sample is overdoped or underdoped. These lead us to make the second assumption that although the bulk (macroscopic) doping of each BSCCO sample is characterized by the transport T_C and the spatially averaged energy gap, Δ_{AVE}, local doping which will determine the local superconducting nature of the sample (the locally measured Δ, the pair amplitude, T_C) reflects the observed inhomogeneity. Putting it another way, the smaller gap region which is sparsely distributed on the underdoped sample behaves as "overdoped", while the larger gap region which is rarely observed in overdoped sample behaves as "underdoped". This assumption is also supported by the recent finding of local Fermi surface variations on BSCCO, indicating that local doping is not equivalent to the macroscopic doping of the sample (Wise2009).

Since we measure Δ, we choose to replot the Emery-Kivelson model illustrated in Figure 3-15. So we see the flipped T_C vs. δ_h relation in the Emery-Kivelson model as a T_C vs. Δ_{AVE} relation as shown in Figure 3-15. Thus, the region, where the smaller gap is measured, we regard as an "overdoped" region, while the region with larger gap is regarded as "underdoped" region, even though our local Josephson measurements are done on overdoped samples (T_C = 76, 79 K and 81 K). Now T^* monotonically increases and the dome-shaped region is simply flipped horizontally as shown when plotted vs. Δ. (Figure 3-15).

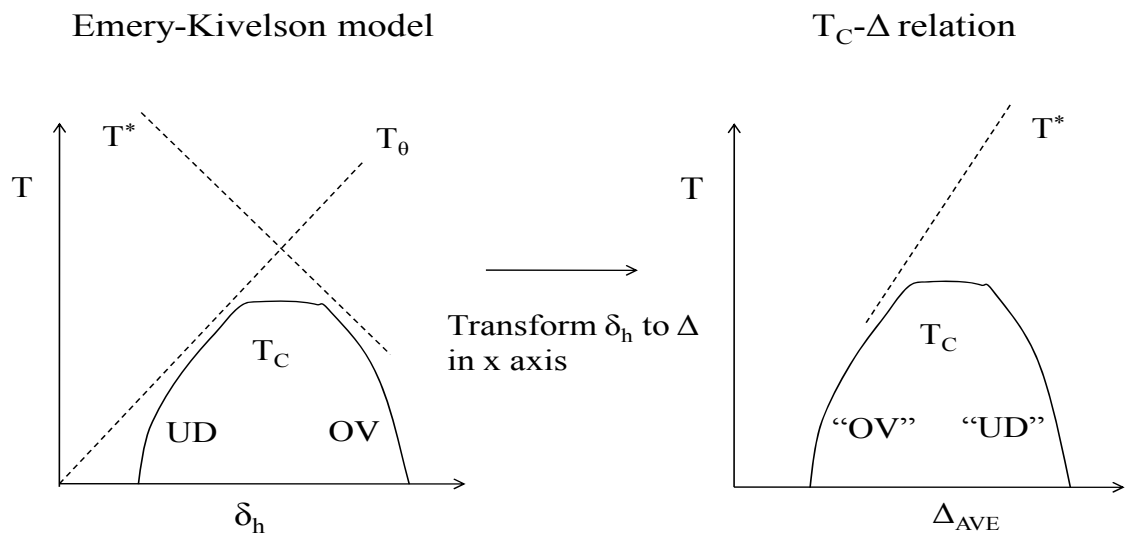

Figure 3-15 Modified Emery-Kivelson model which includes two assumptions, (1) the linear relation between Δ and $T^*$and, (2) a local doping variation on the BSCCO surface

Our results in Figure 3-12 show that I_CR_N is maximized at a gap value of 40 ~ 45 meV, the average Δ typically observed in optimally-doped BSCCO (corresponding to the highest T_C samples). I_CR_N decreases as Δ becomes larger. It also decreases as Δ becomes

smaller. The I_CR_N vs. Δ that we measure behaves in a similar way as T_C vs. δ_h (as δ_h changes towards zero from the critical doping ~ 0.3 at the end of the superconducting region), and it does not follow the behavior of Δ vs. T_C as predicted by the BCS theory. It is important to reiterate that for any given sample, we observed inhomogeneities both in Δ and I_CR_N values as a function of location. Using these assumptions we overlay the modified Emery-Kivelson model picture (Figure 3-15) onto our I_CR_N - Δ relation (Figure 3-12) and this is shown in Figure 3-16.

From our results we correlate the observed I_CR_N with the amplitude of the superconducting order parameter $|\Psi|$ as well as with the T_C of BSCCO via the Emery-Kivelson model phase diagram (Kimura2008). These three quantities (I_CR_N, $|\Psi|$ and T_C) decrease (smaller superfluid density) as Δ increases and anticorrelate with T^*. This inverse relation between I_CR_N and Δ in BSCCO is an unconventional result because in the BCS picture Δ_{BCS}, I_CR_N, $|\Psi|$ and T_C are all correlated. On the overdoped side of the phase diagram T_C decreases as δ_h is increased above 0.16 (Δ also becomes smaller in this doping region; a conventional result). Since the overdoped side is the amplitude dominated region, T^* closely relates to Δ and hence decreases as δ_h is increased. I_CR_N decreases as Δ is decreased from the value around 40 meV in Figure 3-16, indicating I_CR_N, $|\Psi|$, T_C, Δ and T^* behave similarly and conventionally as δ_h is increased towards the critical doping (δ_h ~ 0.3) where T_C vanishes.

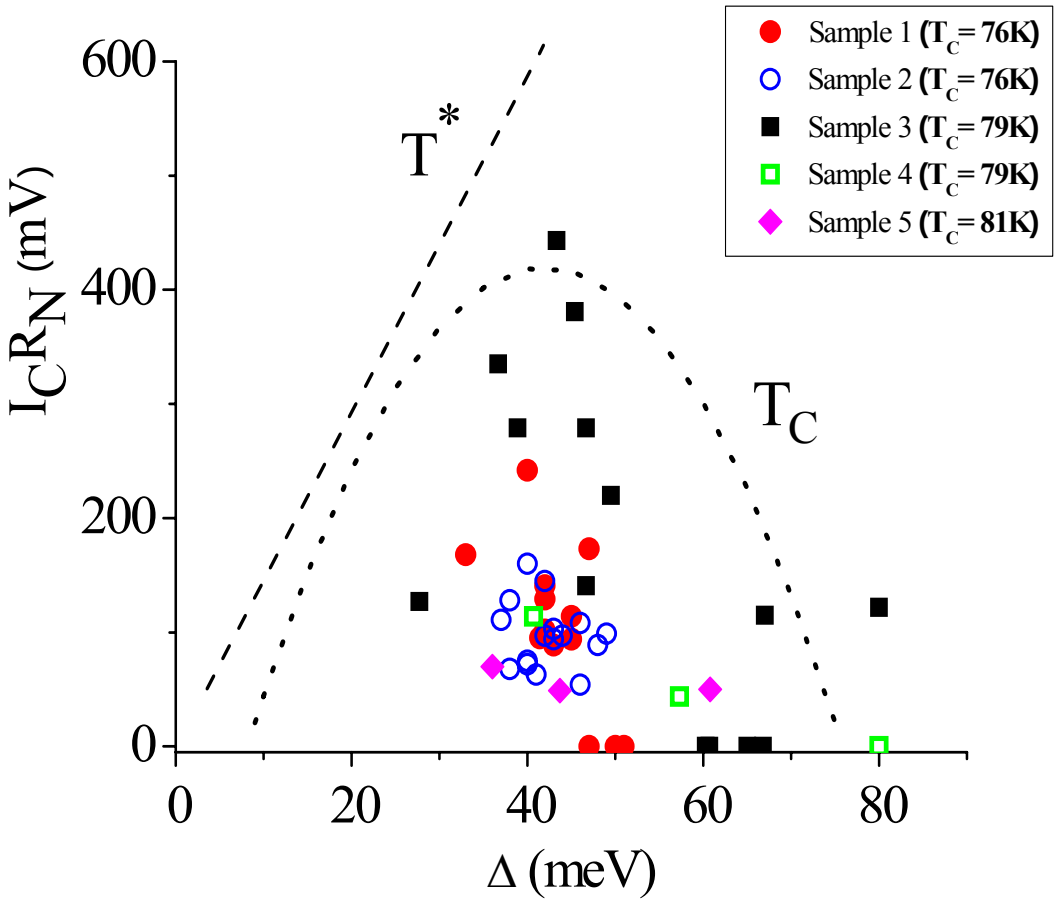

Figure 3-16 $I_C R_N$ vs. Δ with the Emery-Kivelson model. Sketches of T_C and T^* from the Emery-Kivelson model are shown by dotted and dashed lines, respectively. These are overlaid on our result of $I_C R_N$ vs. Δ shown in Figure 3-12. The vertical scale for the model curves is arbitrary.

Another possible framework for discussing our results is the two-gap scenario observed in recent ARPES measurements (Tanaka2006, Lee2007). In the underdoped regime in BSCCO samples, a smaller energy gap is observed and it becomes larger with increasing doping in the nodal region, distinct from the larger energy gap (pseudogap) in the antinodal region where no coherence peaks are observed. Moreover a temperature dependence of the nodal gap follows the BCS functional form very well, while the antinodal gap remains finite at T_C. The same trend of $\Delta(T)$ is also observed in overdoped

samples, but the gapless region above T_C expands on the Fermi surface with increasing doping (suppression of the pseudogap). It has also been reported that two gaps are observed in overdoped $(Bi_{1-y}Pb_y)_2Sr_2CuO_{6+x}$ using a variable temperature STM (Boyer2007). It was claimed that there are smaller, homogeneous energy gaps vanishing near T_C as measured from the dI/dV spectra normalized by normal state conductance, as well as the larger, inhomogeneous energy gaps, which have very weak temperature dependence. Although consistent with our I_CR_N measurements, we do not observe the second gap *directly*. To our knowledge, the momentum *k*-component of the tunneling electron parallel to the junction barrier is conserved in the tunnel process, but the very small confinement of the electron due to the STM tip might increase the uncertainty of momentum and relax the constraint for momentum conservation. Thus the tunneling current observed in the STM could possibly be averaged over a large fraction of the momentum space, therefore, making it difficult to resolve a momentum dependent gap by STM. Moreover the results in Figure 3-16 represent measurements of both I_CR_N and Δ averaged over momentum space, therefore we are unable to address this alternate model.

3-8 Effects of high current density on $Bi_2Sr_2CaCu_2O_{8+\delta}$ electronic structure

In this section the effect of high current density is discussed. Most of this discussion involves preliminary results and ongoing investigations and more studies are necessary to come to a quantitative conclusion. We have observed the LDOS change after low R_N (high current density) measurements. The effect is illustrated in the inset of Figure 3-4. Several questions arise: Does the LDOS change suddenly or continuously? In

the latter case when or at what R_N does it happen? How does LDOS change relate to the Josephson current? We performed "back and forth" measurements in which the BSCCO gap (high R_N measurements) was measured followed by low R_N measurements at the same location on the surface. Results are shown in Figure 3-17. We first measured dI/dV labeled 1, then measured *I-V* characteristics at lower voltages in the region of the Pb gap. R_N is lowered until it reaches that of the *I-V* curve labeled 7. The tip is backed up to increase R_N to measure dI/dV for the BSCCO gap labeled 8 and so on. It is interesting that the BSCCO gap remains almost unchanged after measuring the Pb gap at R_N = 68 kΩ, but a large LDOS change is observed (dI/dV labeled 20) after obtaining the *I-V* curve labeled 19 at R_N = 11 kΩ. The dI/dV curve labeled 20 indicates not only a disappearance of sharp coherence peaks but an apparent increase in the energy gap size. Further decreasing R_N to measure the Pb gap (*I-V* curve labeled 24) makes the LDOS change to a "V" shape (dI/dV labeled 25) where we can not define an energy gap anymore. From similar measurements, we have observed that the BSCCO gap and the shape of dI/dV rarely change by measuring the Pb gap until R_N is reduced to around 30 kΩ, but further decreasing R_N causes a deformation of LDOS. Howald *et al.* observed qualitatively similar dI/dV curves on the intentionally disordered surface by scanning with large tunnel current (Howald2001). Their tunnel condition, however, was at I = 500 pA with V = - 200 mV so the power dissipated from the tip was 10^{-10} W, while the typical tunnel condition used in these current measurements for the *I-V* curve at R_N = 30 kΩ, for example, is I = 500 pA with V = 1.2 mV so that the power dissipated from the superconducting tip is 100 times smaller than that used by Howald *et al.* although tip-sample distance in our STM junctions is smaller. In this configuration the current density,

i, could be calculated using the tunnel current I = 500 pA and the effective diameter of the superconducting tip, ~ 3 Å (for fcc structure of Ag, the nearest neighbor distance is 2.89 Å) over which electrons are being injected. Thus it yields $i \sim 10^6$ A/cm^2, a very high current density. It is still under investigation to answer what makes R_N ~ 30 kΩ the threshold resistance for the BSCCO's LDOS change.

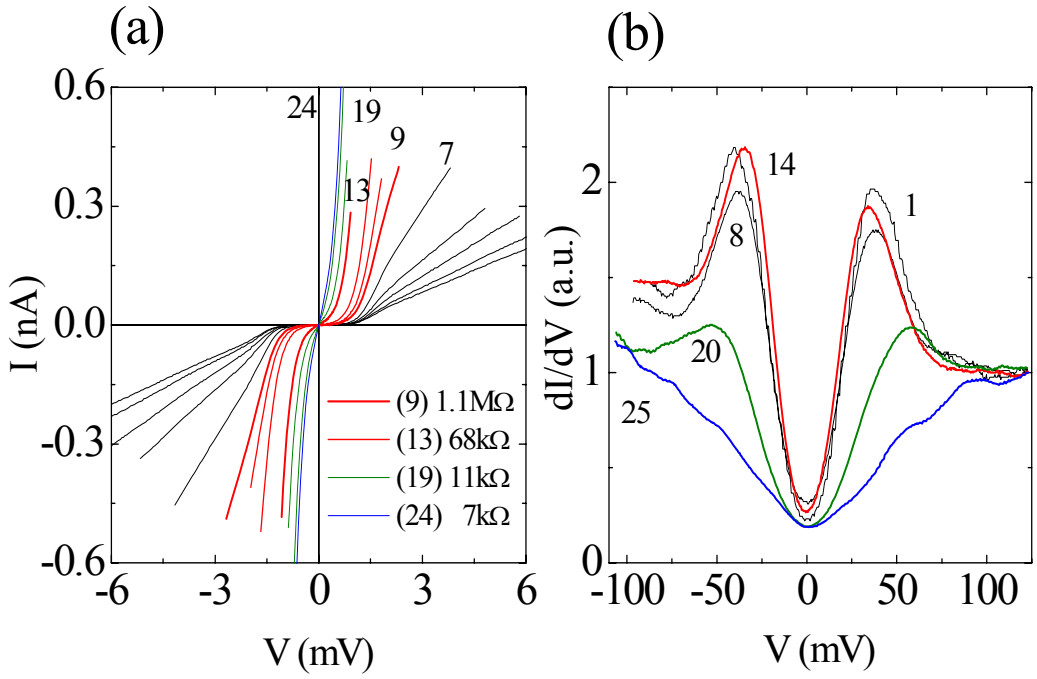

Figure 3-17 (a) I-V characteristics and (b) dI/dV spectra taken at the same surface point on overdoped BSCCO (T_C = 74 K) at T = 2.1 K. LDOS change of this sample is caused by low R_N measurements. The numbers labeled for I-V and dI/dV curves are measured in chronological order. For example, dI/dV spectrum (14) is taken right after I-V curve (13) was measured.

We have also measured how far spatially the high current density affects the density of states, by moving the tip away from the original damaged location to measure dI/dV curves a few nanometers away. Figure 3-18 shows the degraded LDOS is continuously changing, finally recovering to the superconducting LDOS as the tip was

moved away from the originally damaged point. The dI/dV spectrum with sharp coherence peaks is recovered at 13 nm away from the damaged point in opposite directions along a line. While Howald *et al.* "burned" the surface by scanning with a large tunnel current, we "burned" at a specific surface point by taking *I-V* characteristics at low R_N. It is interesting to note that spatial destruction of the BSCCO superconducting LDOS is similar for both experiments. Only qualitative studies of the high current density effect on BSCCO's electronic structure have been done so far, however, a relation between the thermally fluctuated Josephson current and LDOS change is still unknown. Further study is necessary to discuss this effect quantitatively.

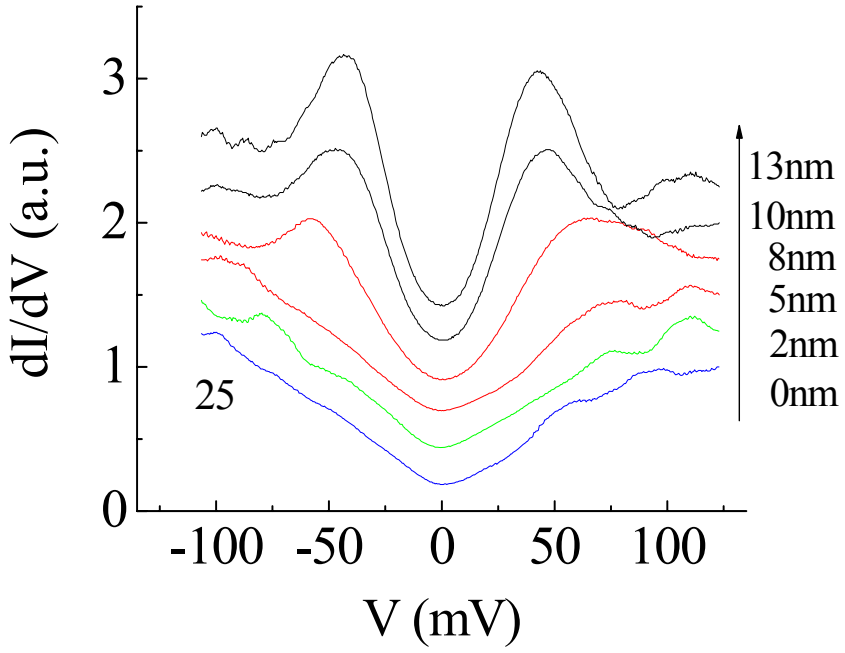

Figure 3-18 dI/dV spectra taken along a line from the originally damaged surface point (offset for clarity). The blue line is the dI/dV spectrum labeled 25 shown in Figure 3-17(b).

3-9 Superconducting STM studies of chemically etched $Bi_2Sr_2CaCu_2O_{8+\delta}$ single crystals

Cleaving the BSCCO to make an atomically flat surface exposed is widely used for STM studies of this material, however, no study of the effect of the cleaving on the electronic structure of BSCCO has been reported. The main question for this study is whether the gap inhomogeneity routinely observed on cleaved surfaces is intrinsic to BSCCO or a result of the cleave. It is well known that the superconducting tunneling probes the depth of a coherence length into the sample surface. Therefore it is important to address this question because the electronic degradation on the surface of BSCCO could affect its tunneling current due to the very short *c*-axis coherence length ($\xi_C \leq 1$ nm) of BSCCO compared with much longer ξ_C of conventional superconductors. Chemical etching is an alternate method to remove a degraded surface layer and possibly make a passivated layer. A chemical etching technique, originally reported by Vasquez *et al.* (Vasquez1988) was applied to Pb/I/YBCO tunnel junctions (Gurvitch1989, Valles1991) and Josephson junctions (Sun1994a). An STM study of etched YBCO single crystals (Sun1996, Truscott thesis) revealed that etching with 1 % Bromine (Br) by volume in 100 % methanol resulted in an etching rate of 250 Å/min. The etching proceeds layer by layer and results in large flat areas separated by steps with single unit cell depth (~ 12 Å). The etching also produced pits on the surface which expand radially, introducing a little surface roughness, but further etching removed layers without increasing roughness.

For BSCCO single crystals, however, it turned out that 1 % Br in methanol was strong enough to make the etched surface drastically rougher, causing the STM to tip-crash. An Atomic Force Microscope image of the etched surface by 0.1 % or higher

concentration of Br is shown in Figure 3-19. Note that the vertical range is almost 70 nm. It appears that BSCCO is more sensitive to the etching than YBCO and a higher concentration of Br increased the surface roughness as etching time becomes longer.

In order to optimize the etching condition, etching rate calibrations were performed as follows: The BSCCO single crystal as well as the silver epoxy around the crystal was coated with thinned rubber cement leaving a small region of exposed BSCCO. The reason for coating the silver epoxy is because the reaction of Br against the epoxy was unknown. This coating protected the epoxy so that it did not discolor with the Br etch. The etching solution consisting of 0.01 %, 0.05 % and 0.1 % Br in methanol were taken in a pipette and dropped on the BSCCO single crystal for 3 minutes. Since the etching solution was highly volatile, we kept adding it on the sample surface to be completely covered during the etching. We then rinsed the surface by dipping the sample in methanol in an ultrasound cleaner and then removed the cement with a sonication of toluene. We observed clear steps at various edges of the etched region of roughly 2000 Å for 0.01 % Br, 5000 Å for 0.05 % Br and 6000 Å for 0.1 % Br by using a commercial profiler. Therefore the etching rates for 0.01 %, 0.05 % and 0.1 % Br are ~ 650 Å/min, 1700 Å/min and 2000 Å/min, respectively.

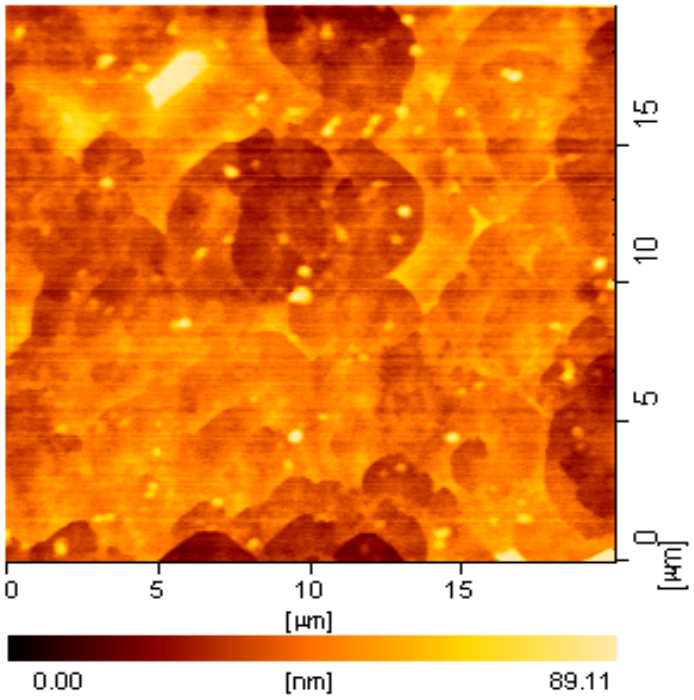

Figure 3-19 Atomic Force Microscope image of BSCCO single crystal etched by the Bromine concentration between 0.1 and 1 % at room temperature.

Etching the BSCCO surface using 0.01 % Br in methanol proceeds layer by layer and results in many flat areas separated by steps of fractions or multiples the BSCCO unit cell and this concentration gives reproducible etched surfaces with vertical corrugation smaller than 10 nm even if the etching time becomes longer than 3 minutes. Figure 3-20 shows a typical etched surface of overdoped BSCCO (T_C = 74 K) in 0.01 % Br for 5 minutes followed by rinsing in methanol and blowing nitrogen gas for drying. The etched surface consists of "pancakes" with lateral dimensions ~ 100 Å. These pancakes have

various step heights of not only a half unit cell in depth, 15 Å (Figure 3-21), but 5 Å, 10 Å or even single unit cell length, ~ 30 Å.

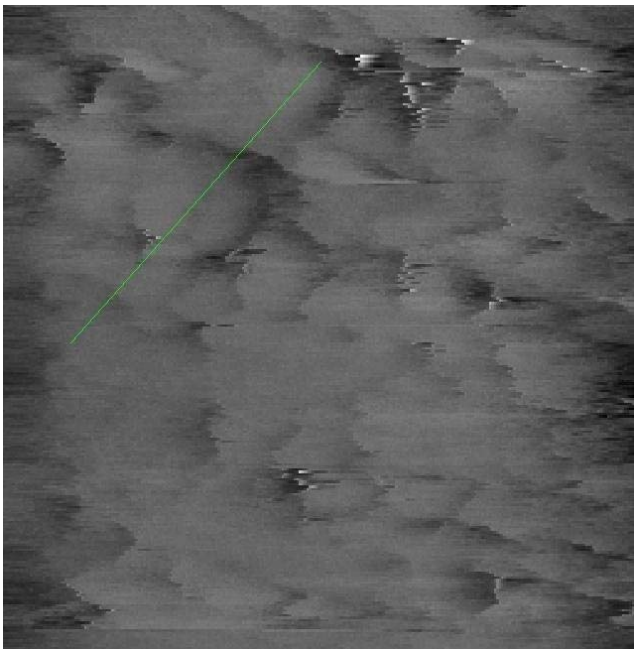

Figure 3-20 STM image of 0.01 % Bromine etched overdoped BSCCO (T_C = 74 K) at room temperature. Scan size is 900 Å × 900 Å.

The distribution of various step heights observed on the etched BSCCO surface is shown as a histogram in Figure 3-22, indicating that steps with 5 Å height are as common as 15 Å step heights. This result motivated us to investigate what the surface of a 5 Å step corrsponds to at the atomic layer of BSCCO single crystal by topography and tunneling spectroscopy.

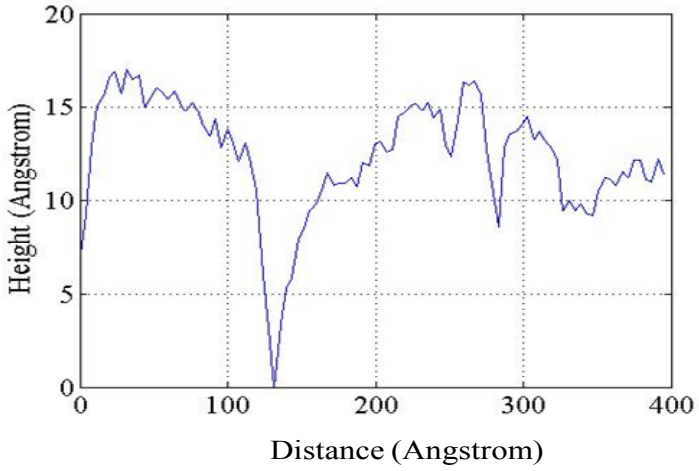

Figure 3-21 Cross section along the line shown in Figure 3-20.

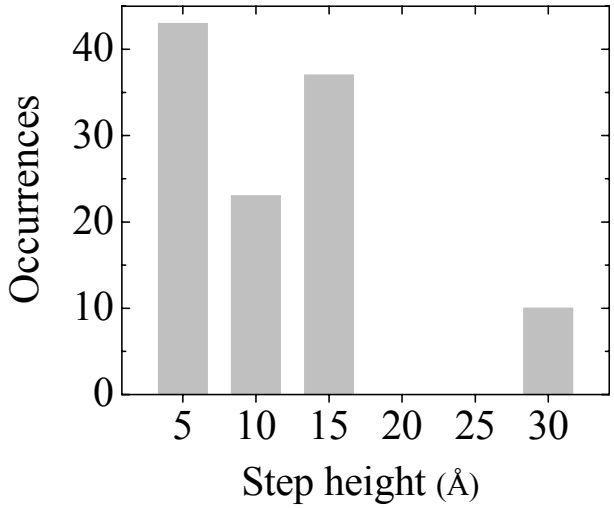

Figure 3-22 Histogram of step heights observed in Bromine etched uncleaved BSCCO single crystals.

Figure 3-23 shows the topography taken at T = 2.1 K of the same overdoped BSCCO sample as shown in Figure 3-20. It is worth noting that the topography such as Figure 3-23 is rarely observed at low temperature and we actually obtained noisy images

when the tip was moved to other surface areas, on the contrary to reproducible topography at room temperature. While we do not understand this, we nevertheless performed the spectroscopic measurements on the area shown in Figure 3-23. The pancake in the center of Figure 3-23 has a step height of 15 Å on which *I-V* and dI/dV measurements are performed simultaneously. The results are shown in Figure 3-24. The dI/dV spectrum shows a distorted LDOS typically observed on BiO surface, but one distiction is seen. The quasiparticle states are suppressed near the Fermi energy. This type of dI/dV curve riminds us of those observed on CuO_2 layer (Misra2002). Figure 3-25 shows the *I-V* characteristics measured on the etched surface of the different overdoped BSCCO samples at $T = 2.1$ K. Figure 3-25(a) shows an *I-V* characteristic measured with a large bias range, showing a similarity to that in Figure 3-24(b). Then R_N was decreased for the Pb gap measurement and it was observed at the same location on this sample as shown in Figure 3-25(b). So far we have only one sample etched by 0.01 % Br showing the Pb gap clearly.

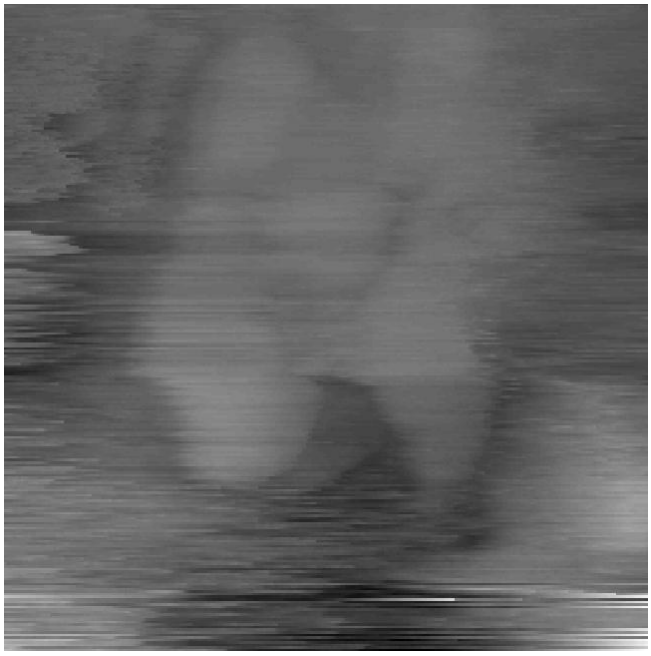

Figure 3-23 Topography of the same BSCCO sample in Figure 3-20 at T = 2.1 K. Step height of the pancake in the middle of the figure is 15 Å. Scan size is 200 Å × 200 Å.

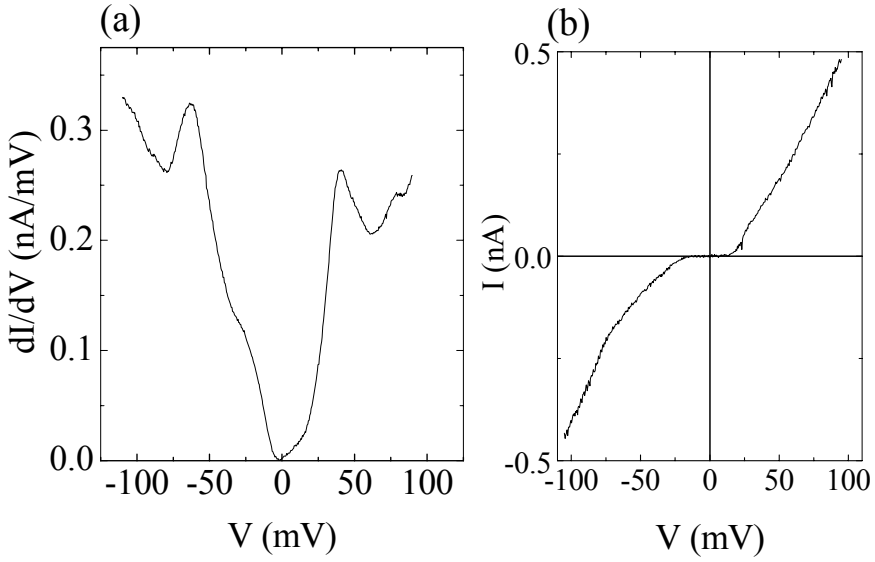

Figure 3-24 Spectroscopies measured simultaneously with a large bias at T = 2.1 K on the 0.01 % Bromine etched overdoped BSCCO. (a) dI/dV spectrum observed on the pancake at the center of Figure 3-26 (b) *I-V* characteristic measured simultaneously. Note that there is strong suppression of the quasiparticle states near the Fermi energy.

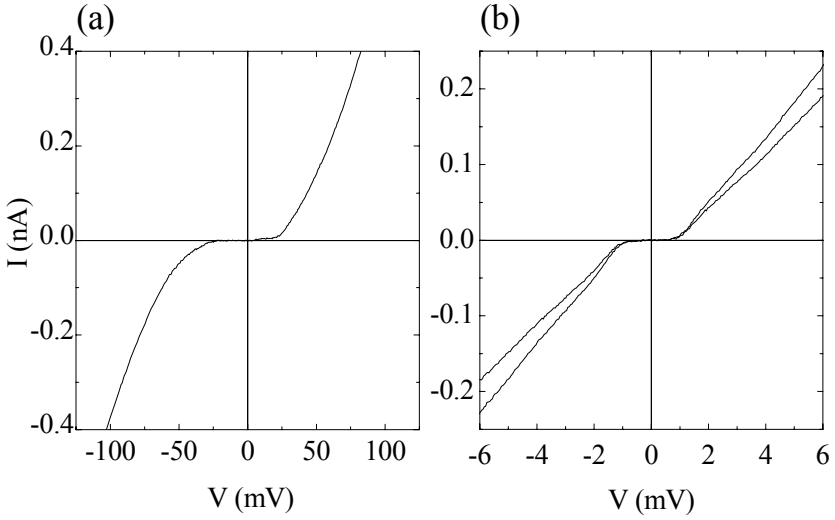

Figure 3-25 *I-V* characteristics taken at different R_N at the same surface point on the 0.01 % Bromine etched overdoped BSCCO at $T = 2.1$ K. (a) *I-V* characteristic measured with a large bias range (high R_N measurement). (b) *I-V* characteristic measured at lower R_N. The Pb gap is clearly seen around $V = 1.4$ mV.

From the 0.01 % Br etching on BSCCO results, there are problems for observing the Pb gap and good topographic images at low temperature. Since we obtained the image like Figure 3-20 by 0.01 % Br etching at room temperature, we assumed Bromine did etch BSCCO surface. But the difficulty in observing the Pb gap reproducibly raised a question such as: did 0.01 % Br etching proceed on BSCCO? To answer this question, we first scanned the BSCCO sample at room temperature without doing any cleaving or etching. Surprisingly we obtained the tunneling image which was very similar to those in Figure 3-20, indicating that we still do not know 0.01 % Br in methanol is enough to etch BSCCO surface to remove the dead layer. Currently we are using higher concentration of Bromine to see whether the etching proceeds on BSCCO without increasing the surface roughness.

Figure 3-26 shows a typical etched surface of overdoped BSCCO (T_C = 74 K) in 0.1 % Br in methanol for 3 minutes followed by rinsing in methanol and blowing nitrogen gas for drying. The etched surface consists of "pancakes" with lateral dimensions ~ a few hundred Å, larger than those made by 0.01 % Br etching. These pancakes have various step heights of not only a half unit cell in depth, 15 Å (Figure 3-27), but also 5 Å and 10 Å. Figure 3-28 shows a large area scan of the same sample as Figure 3-26. A vertical corrugation over this surface is less than 30 Å, indicating that the 0.1 % Br etching proceeds layer by layer.

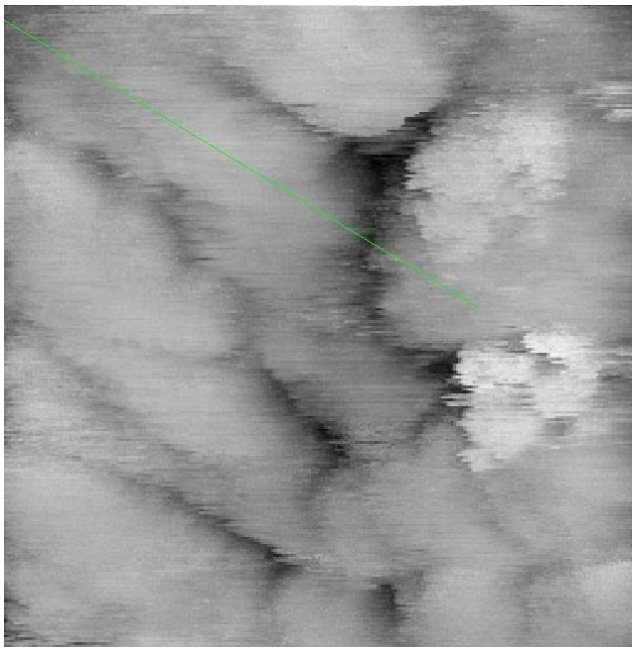

Figure 3-26 STM image of 0.1 % Bromine etched overdoped BSCCO (T_C = 74 K) at room temperature. Scan size is 800 Å × 800 Å.

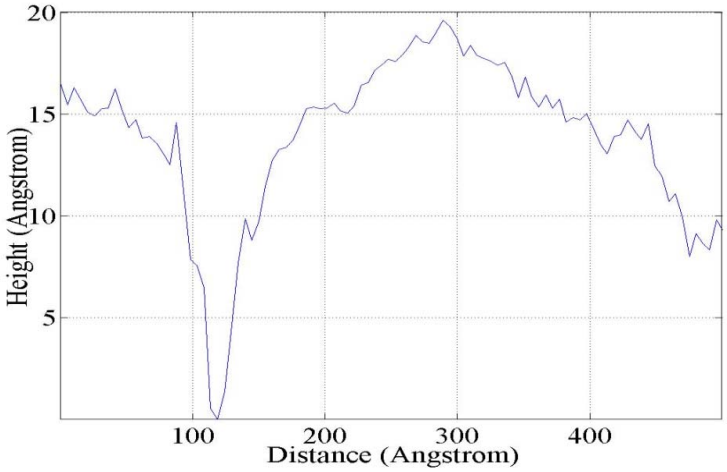

Figure 3-27 Cross section along the line shown in Figure 3-26.

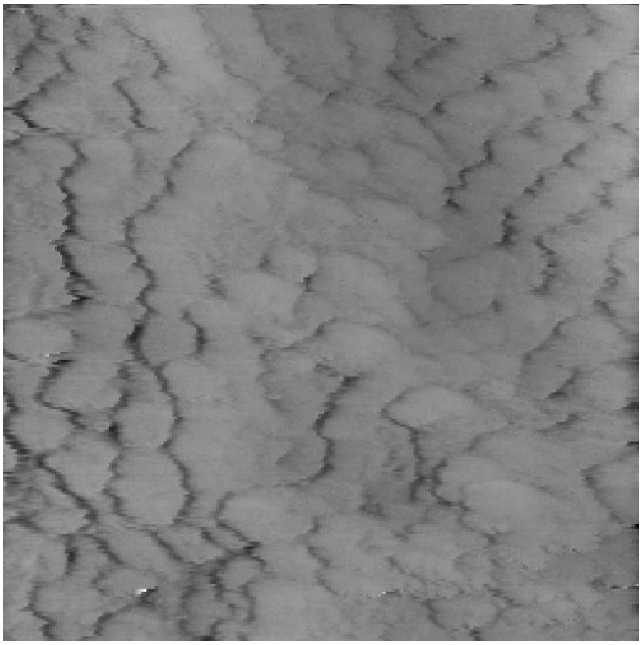

Figure 3-28 Room temperature STM image of the same surface in Figure 3-26 with larger scan area. Scan size is 3200 Å × 3200 Å.

Figure 3-29 shows the dI/dV spectra measured on the 0.1 % Br etched overdoped BSCCO sample at T = 4.2 K. Two dI/dV curves were taken 10 Å apart. It is noting that the spectral line shape looks very similar to that observed on the cleaved BSCCO sample except the asymmetry typically observed for the cleaved sample that the coherence peak below the Fermi energy is always larger than the other side. Nevertheless the result is reproducible and less noisy than those observed on the 0.01 % Br etched sample shown in Figure 3-24(a). We then cooled this sample to T = 2.1 K to measure the Pb gap. Figure 3-30 shows the *I-V* characteristic measured at a lower R_N. The Pb gap was clearly seen around V = 1.4 mV although the *I-V* curve was not taken at the same surface point as Figure 3-29. It is very interesting to study how dI/dV spectra and the Josephson $I_C R_N$ product vary over the etched surface.

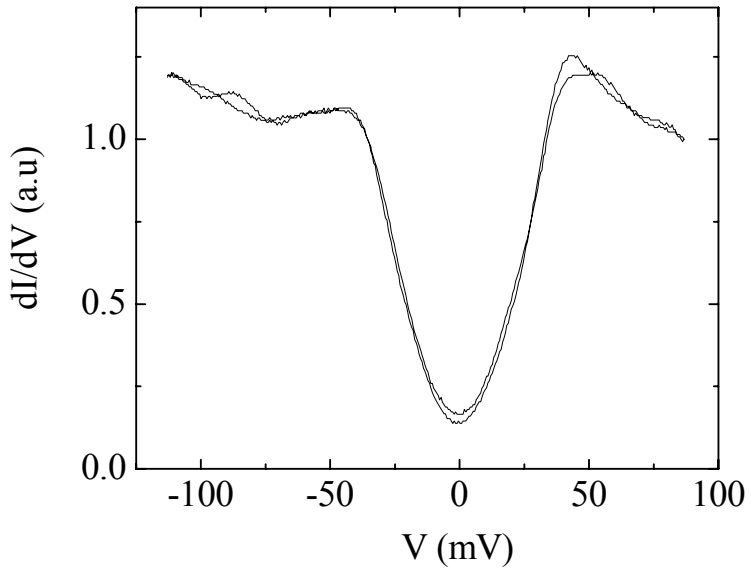

Figure 3-29 dI/dV spectra with a large bias measured on the 0.1 % Bromine etched overdoped BSCCO at T = 4.2 K. Two dI/dV spectra were measured 10 Å apart.

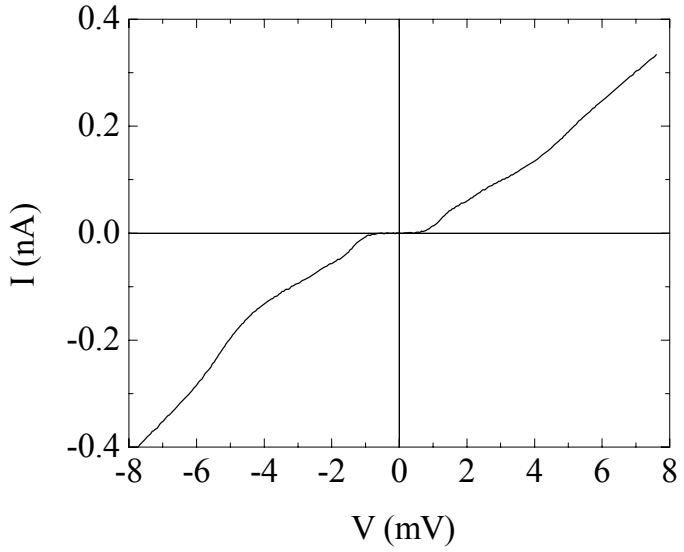

Figure 3-30 *I-V* characteristic measured at lower R_N on the 0.1 % Bromine etched overdoped BSCCO at $T = 2.1$ K. The Pb gap is clearly seen around $V = 1.4$ mV.

It is shown from these preliminary experiments for etched BSCCO surfaces by 0.01 % and 0.1 % Br in methanol that the chemical etching proceeds layer by layer on BSCCO single crystals and yields a passivated surface. Observations of the superconducting Pb gap ensure that the passivated layer is thin enough for vacuum tunneling, but the thickness might change from the etched sample to sample because of the difficulty in observing the Pb gap reproducibly for 0.01 % Br. As seen from the topography taken at low temperature in Figure 3-23, the surface looks more noisy compared with the room temperature image (Figure 3-20) as well as the fact that it is hard to obtain the images reproducibly at low temperature, this noise prevents us from identifying the topmost layer of the pancakes using surface topography and spectroscopic measurements. Since we need to handle Br under a fume hood because of its high volatility and toxic nature, and the etching process is done in air, it possibly results in

surface contamination although it still remains puzzling why the image is better (less noisy and reproducibly obtained) at room temperature than at low temperature.

In conclusion of this section, we have prepared the BSCCO surface by chemical etching for our superconducting STM study. The etched surface by 0.01 % Br consists of a pile up of "pancakes", which have a lateral dimension of 100 Å with step edges ranging from 5 Å to a few unit cell heights. We observed the DOS with a large gap and a suppression of the states near the Fermi energy instead of that typically observed on the BiO surface. The Pb gap is also observed with low success ratio. The etched BSCCO surface by 0.1 % Br in methanol gives more reproducible dI/dV spectra and it seems promising to carry out the extensive low R_N measurements to see whether the Josephson current is observed on the etched BSCCO surface. We need further quantitative studies of the etched surface to improve reproducibility and to see dI/dV curves with a better topography at low temperature.

Chapter 4 Future directions

4-1 Local Josephson measurements on underdoped $Bi_2Sr_2CaCu_2O_{8+\delta}$ single crystals

4-1-1 Motivation

We have shown that the *c*-axis Josephson coupling between the conventional superconducting tip and overdoped $Bi_2Sr_2CaCu_2O_{8+\delta}$ (BSCCO) single crystals was clearly observed. It was also revealed that there was not only inhomogeneity of the superconducting pair amplitude but also an anticorrelation between the energy gap Δ and the I_CR_N products as Δ becomes larger than 40 meV. This result was interpreted by the Emery-Kivelson model (Emery1995) with two assumptions (Kimura2008). From our studies of overdoped BSCCO single crystals, I_CR_N corresponding to $\Delta \geq 60$ meV tended to be small or zero (see Figure 3-16). If this is correct for heavily underdoped samples where the measured dI/dV spectra of the BSCCO density of states in most of the surface regions no longer shows the sharp coherence peaks (McElroy2005a, Gomes2007, Alldredge2008) , we are less likely to observe the finite I_CR_N products on the large gap region of this sample. However, it has also been reported that there are still small regions with coherence peaks and an energy gap Δ between 40 and 50 meV observed on the heavily underdoped samples (McElroy2005a, Alldredege2008) and if these regions have the same superconducting characteristics as those observed in the region of overdoped sample with the same gap values, we could possibly see finite I_CR_N products in the same region in this underdoped BSCCO. Then the local Josephson measurements can show how the finite I_CR_N regions are connected with the large Δ regions where I_CR_N is zero.

This could be a test to see if the Emery-Kivelson model and our interpretation appropriately describe the high-T_C superconducting cuprates.

4-1-2 Preliminary results

I present a preliminary result of the local Josephson measurements on underdoped BSCCO single crystal (T_C = 64 K). We first observed the dI/dV spectra along a line 30 nm long on this sample. The result is shown in Figure 4-1, indicating that the shape of dI/dV curves is different than those typically observed in the dI/dV spectra with coherence peaks on optimally-doped or overdoped samples (see Figure 3-11(c)). This is consistent with other results for similar doping samples (Lang2002, McElroy2005a, Gomes2007, Alldredge2008) in that most of the surface area shows larger gaps estimated from the dI/dV as shown in Figure 4-1. On the other hand, we also found a few regions on overdoped samples where the dI/dV spectra were similar to those in Figure 4-1 and $I_C R_N$ was zero or very small. Furthermore the dI/dV change affected by the high current density observed on overdoped samples (see Figure 3-17(b)) also looks similar to those in Figure 4-1. As discussed in the previous subsection, our primary goal for studying underdoped samples is to perform local Josephson measurements at a small gap region to compare with the measurements at larger gap regions to see the spatial variations of the superconducting pair amplitude. These are currently ongoing measurements and the preliminary results of local Josephson measurements on the larger gap regions are presented here.

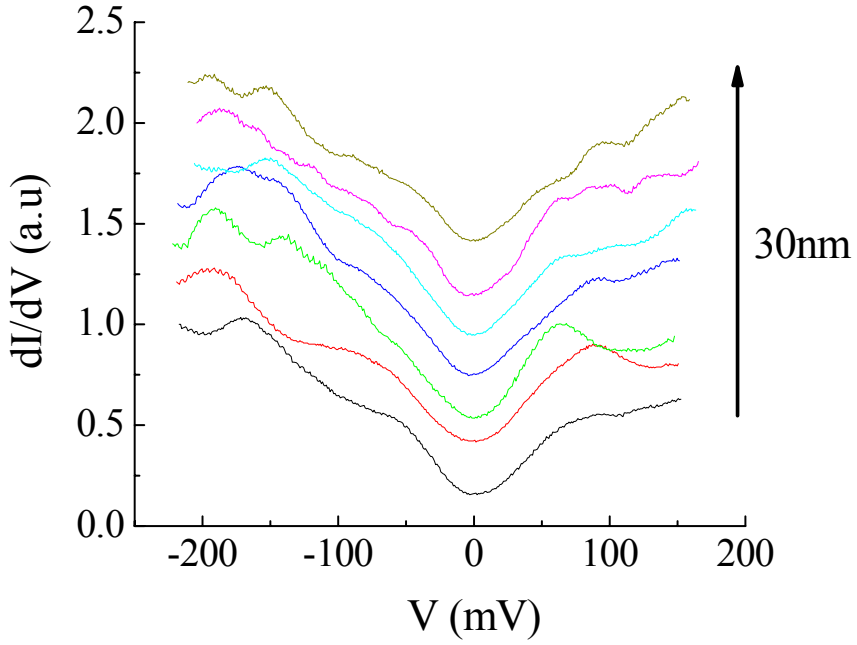

Figure 4-1 dI/dV spectra of underdoped BSCCO (T_C = 64 K) taken every 5 nm at T = 2.1 K (offset for clarity).

In Figure 4-2, we plot the *I-V* characteristics at a lower bias on a region where the BSCCO gap is very large, similar to those in Figure 4-1. As is the case of Pb/I/overdoped BSCCO STM junctions, we first checked the Pb gap around R_N = 3 MΩ. Then R_N was decreased until the contribution from the thermally fluctuated Josephson currents was seen. The lowest R_N achieved for Pb/I/underdoped BSCCO STM junctions measurements was R_N = 17 kΩ. Figure 4-3(a) displays a close-up view of one of the *I-V* characteristics near zero bias measured at R_N = 50 kΩ, showing the Josephson coupling between the superconducting Pb tip and the underdoped BSCCO. Figure 4-3(b) shows the contributions from the thermally fluctuated Josephson current after subtracting the quasiparticle background from the *I-V* curves of Figure 4-3(a). The data in Figure 4-3(b) is shown as line and the best fit to the equation (2-40) (Ivanchenko-Zil'berman formula)

is represented by the symbol. Although we clearly saw the Josephson contribution at R_N = 50 kΩ, we did not observe it at the lower R_N. It wouldn't be too surprising to see only one Josephson contribution on the *I-V* curve at the larger gap region because it is expected from our results described in chapter 3, that $I_C R_N$ tends to be smaller or zero at the "pseudogap" region. The lowest R_N = 17 kΩ is lower than the threshold value (~ 30 kΩ) below which the high current density effect changes the BSCCO electronic structure. This might cause the disappearance of I_C at R_N lower than 30 kΩ. Reproducibility of the Pb gap was checked after the *I-V* characteristic measurement at R_N = 17 kΩ, shown as the blue line in Figure 4-2. The reproducibility of the superconducting gap assures the Josephson contributions observed at the lower R_N was not an artifact.

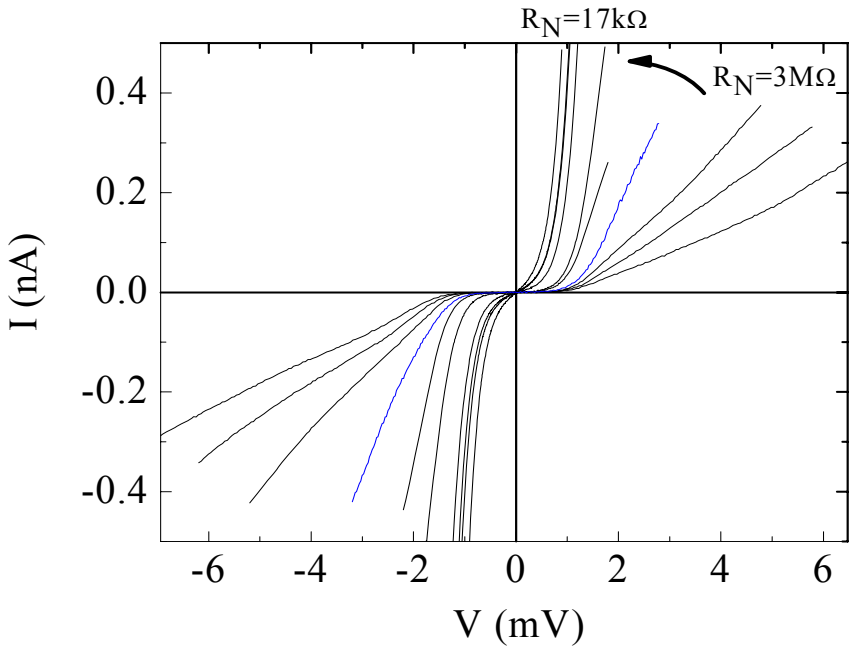

Figure 4-2 *I-V* characteristics of Pb/I/underdoped BSCCO (T_C = 64 K) STM junctions at T=2.1 K. The Pb gap is clearly seen around V = 1.4 mV. One of the *I-V* curve (blue line) was taken after the *I-V* curve was measured at the lowest R_N = 17 kΩ to check the superconducting tip.

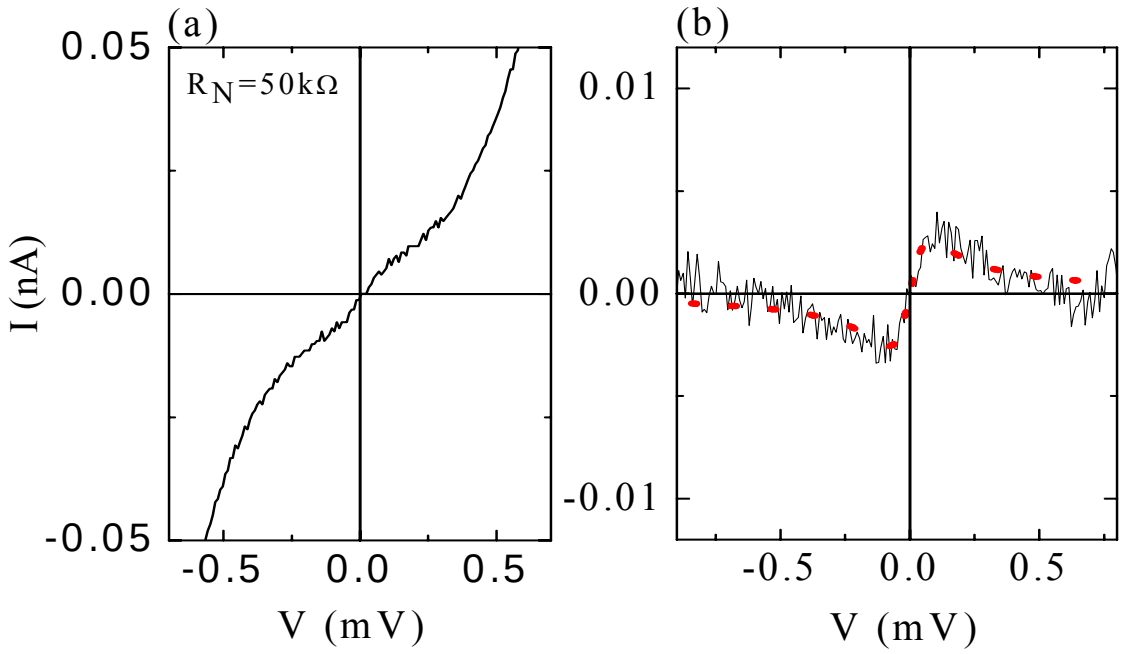

Figure 4-3 Low bias *I-V* characteristics of Pb/I/underdoped BSCCO (T_C = 64 K) STM junctions at T = 2.1 K. (a) A close-up view of the *I-V* curves with the Josephson contribution shown in Figure 4-2. (b) Thermally fluctuated Josephson current peaked at V_P as derived by subtracting quasiparticle background from the *I-V* curve (Figure 4-3a). The data is represented by the line and the symbol represents two-parameter fits to the phase diffusion model.

Although there was only one data point for the Josephson contribution observed at this surface point, it is interesting to estimate I_CR_N using the previously determined T_n for this experimental apparatus. Since $I_C \times \sqrt{e/k_BT_n} = 2.2$ at G_N = 20 μS (R_N = 50 kΩ) obtained from the fit in Figure 4-3(b), I_CR_N at this surface point is ~ 100 μV. This is consistent with the data observed in the larger gap region measured on overdoped samples shown in the I_CR_N vs. Δ plot in Figure 3-16. Further local Josephson studies on the smaller gap region with coherence peaks on underdoped BSCCO are required to discuss validity of the Emery-Kivelson model and our results for high-T_C superconducting cuprates.

4-2 Superconducting STM study of nano-particles deposited on $Bi_2Sr_2CaCu_2O_{8+\delta}$ single crystals

Superconductivity in a normal metal with a clean interface with a superconductor is induced by the proximity effect, which has been extensively studied for both practical and fundamental interest (Deutscher1969). STM enables us to measure the superconductivity induced in nanometer-size metallic particles deposited on conventional superconductors with short coherence length locally (Truscott1999). It is natural to ask about the proximity effect on metallic particles deposited on high-T_C superconducting cuprates. Previously, normal metal scanning tunneling spectroscopy has been performed on small gold grains deposited on BSCCO (Truscott thesis). For a thin deposition of gold on BSCCO, small particles resulted and for the thinnest average film thickness, the resultant grains were studied. The dI/dV spectra did not show a superconducting gap with coherence peaks, but a gap-like structure (no coherence peaks) at the same energy as the bare BSCCO gap. As the thickness of the film, and hence the size of the grain was increased, the size of the gap-like structure was diminished. Similar results were reported for a normal STM study of gold deposited on a (100) surface of YBCO, indicating that the gap measured from the dI/dV spectrum was exponentially decaying as tip was moved away from (100) facet toward the center of the gold grain (Sharoni2004). These results raise many questions: is the gold grain superconducting and what is the nature of the superconductivity induced in gold grains? A superconducting STM can directly probe the superconductivity on the gold particles via *c*-axis Josephson tunneling as well as the quasiparticle excitation spectra. It was also observed previously that the deposited particles tend to accumulate near a cleaved step edge (Truscott thesis). This is maybe due to the "smoothing effect" of the surface electronic distribution (electron delocalization)

occurs at the step edge, resulting in the larger dipole contribution there (Smoluchowski1941) and the enhanced surface electric field attracts the adsorbed atoms or molecules toward the step edge more than on the flat region (Lang1971, Besocke1977). It could also be that the Van der Waals bonding is so weak that the evaporated atoms have a high mobility on the surface because of their evaporation energy. When they hit a step edge, the bonding is more likely chemical and so binds the Au atoms. Using this configuration of accumulated gold particles near the step edge provides us the opportunity to study the Josephson coupling in the *a*(*b*)-axis via gold particles. A superconducting STM study of the proximity effect on BSCCO will give more information about the nature of the paring in this material.

4-3 Superconducting STM with quench condensed deposition

As stated in the Introduction (chapter 1), the superconductor-insulator transition in two dimension shows behavior similar to the high-T_C superconducting cuprates (Merchant2001). There have been several transport studies, fewer spectroscopic studies and only a few spatial studies for ultrathin disordered metallic films in this interesting transition region. In the latter case the study was primarily morphological, and spectroscopic techniques were not extensively used (Ekinci1999). In the granular regime (or phase fluctuation dominated regime) we have shown that the grains or clusters are probably superconducting (Barber1994), but that they are not phase coupled together for the thinnest samples. Hence, there is no long range superconductivity and no metallic behavior. An existence of the Cooper pairs in the insulating side of the film also has been verified by the observation of magnetoresistance oscillations with a period of $h/2e$ in the

ordered granular film (Stewart2007). Utilizing the superconducting STM, we should be able to study the pair amplitude as we go through this transition: both its existence and the spatial nature of the phase fluctuations. In contrast to studying separate samples, this technique of "*in situ*" film growth followed by transport and spectroscopic studies has been the most effective way to study this transition. Additional evaporations and measurement cycles allow us to step through the superconductor-insulator transition and perform studies at each step. We can also use this technique to study homogeneous films (deposited onto Ge or Sb underlayers). In this homogeneous preparation we observe an amplitude dominated superconductor-insulator transition. As we have mentioned already, the spatial resolution of the STM and its ability to measure Josephson coupling in the fluctuating regime positions us to elucidate the mechanisms of the superconductor-insulator transition in both the homogeneous and granular systems.

In order to realize this, a new superconducting STM has been constructed to add the experimental capability of low temperature evaporation (quench condensation). New design features are summarized as follows:

1. In order to reduce the noise temperature affecting the Josephson phase dynamics, the new microscope requires low temperature noise filtering on four additional transport leads as well as on the tunnel current and bias voltage leads. The apparatus has been built with a cluster of 6 cryogenic copper powder filters (4 transports, 1 bias, 1 tunneling current) installed below the STM stage of the system shown in the (5) of Figure 4-4. Because these filters have significant cross-sectional area, they are also utilized as thermal links for cooling the STM stage. Special care is also taken in the wiring for the STM. We use miniature stainless steel coaxial

cables and manganin 290 wires and these are connected with an interconnector glued on the copper powder filter housing. Two of the Beryllium Copper (BeCu) finger rings (larger diameter) are attached around the evaporation and the filter plates as well as one ring with a smaller diameter around the electrical contacts plate at the bottom for a good thermal link to the liquid He bath. The usage of the BeCu fingers also helps minimize a leakage of electromagnetic noise radiated from the room temperature part of the vacuum chamber.

2. The evaporation stage is designed to be removable. This feature partly accommodates the crowded overall design because of the small dewar bore (setting the sample and STM tip can be done before the evaporator stage is in place). The removable evaporator also makes the reloading of evaporation sources more convenient. Two tungsten baskets for evaporation sources can be loaded (see (3) of Figure 4-4). The basket is made by winding 0.005" tungsten wire around the tapered screw. Average thickness of evaporated materials is measured by a quartz crystal microbalance with the associated oscillator circuit located above the evaporation stage (see (1) of Figure 4-4).

3. The current superconducting STM utilizes a nested configuration for the piezo tubes. The scan piezo tube is contained inside the coarse piezo tube. Because such a configuration would force evaporations at grazing angles, the new system has the piezo tubes on opposite sides of the STM stage (see (8) of Figure 4-4). The original design used two 1" piezo tubes. This is not possible in the new configuration given the space available, so a design compromise is to shorten the coarse piezo tube while keeping the scan piezo tube the same. This modification is expected to

lengthen the approach time for coarse motion, but not affect the overall functioning of the system.

4. Thermal contact between the current superconducting STM and the liquid He bath is achieved by using He^4 exchange gas. We, however, can not use the exchange gas for the new quench condensed STM since it prevents vacuum evaporation. Moreover we need to use thick copper wires (Belden #83350) to feed high currents to the evaporator, but these cables at the same time convey a lot of heats from the room temperature part of the system so that they must be cooled. These cables will run through the liquid He bath surrounding the vacuum tail, at the bottom of which an additional feed through (Varian #954-5030) is installed to make electrical contact with the new STM insert via the spring contact probes (Interconnect devices #S5A16.4G) (see (6) of Figure 4-4). Since the thick copper wires also run from the spring contact probes to the evaporation stage above the STM plate in the ultra high vacuum region, this configuration is expected to function for absorbing the heat generated by thermal evaporations with the BeCu finger ring around the plate.

5. It is necessary for the substrate to accommodate pre-deposited electrodes for the transport measurements. One of the technical difficulties is how to make a connection between the electrodes and a thin, in-situ deposited film. We fabricated evaporation masks for the electrodes out of 0.005” thick stainless steel sheet using wire electro-discharge machining (EDM). This technique enables us to make four slits for the electrodes with a width of 0.010” each, facing diagonally each other without any intersection at the vertex (see (7) of Figure 4-4). Area of the vertex is about 0.010” × 0.010” where the evaporated film is to be deposited.

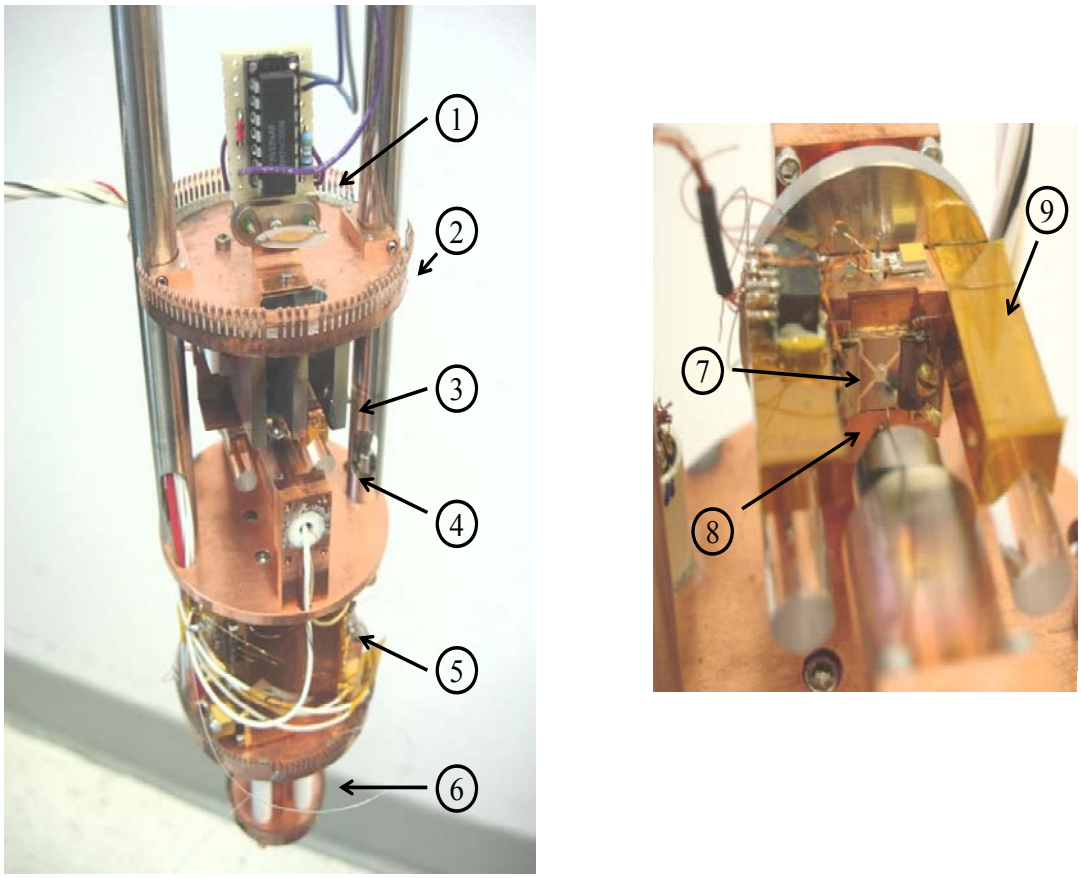

Figure 4-4 Newly designed superconducting STM with quench condensed deposition overview. (1) Quartz crystal microbalance associated with an oscillating circuit (2) BeCu finger for thermal contact to the liquid He bath (3) Thermal evaporator (baffle removed): two tungsten basket evaporation sources. (4) STM stage (5) Microwave copper powder filters for tunnel current, bias voltage and four leads for transport measurements (6) Electrical contacts for high current for thermal evaporations (7) Substrate with pre-deposited four electrical contacts (8) Superconducting STM tip attached on the top of scan piezo motor. (9) Sample holder which slides on quartz rods. Long arms protect the quartz rods from contamination due to the evaporation.

Once the new superconducting STM with quench condensed deposition is operating, many intriguing experiments can be undertaken. Local Josephson measurements as well as STM/S studies on the insulating side of the superconducting-insulator transition in granular films can be done in order to see how $I_C R_N$ varies spatially over the film compared with the morphology. We can study how the pair amplitude

correlates with the superconducting gap Δ in the strong phase fluctuation regime. These results can then be compared to the underdoped side of high-T_C superconducting cuprates. For uniform films, it has been reported that Δ as well as T_C collapse, keeping $2\Delta/k_BT_C$ constant as the superconductor-insulator transition is approached (Valles1989b). This indicates the existence of a quantum critical point. We are interested in exploring this film toward the superconductor-insulator transition by this new microscope to see how the superconducting pair amplitude collapses as Δ decreases over the film, and to study if there is a similarity in the physics of the overdoped side of high-T_C superconducting cuprates.

Chapter 5 Conclusion

A superconducting STM tip consisting of a Pb/Ag bilayer deposited on a Pt/Ir wire was shown to be a local probe of the superconducting pair wave function via Josephson tunneling. The Josephson phase dynamics in the STM Josephson junction formed between conventional superconductors was in the strong thermal fluctuation regime and we observed the voltage-dependent pair current near zero bias which was well explained by a classical phase diffusion model. Unlike conventional BCS superconductors, no comprehensive microscopic theory exists for high-T_C superconducting cuprates to link the superconducting ground state and the excited quasiparticle state. Our superconducting STM is a powerful tool to study the inhomogeneous material because it allows us to measure both the superconducting phase via the Josephson effect and the energy gap amplitude from the spectroscopic measurements.

In this thesis work of a scanning Josephson tunneling microscope study of overdoped BSCCO single crystals, we clearly observed, for the first time, the local *c*-axis Josephson coupling between a conventional *s*-wave superconducting tip and BSCCO single crystals, indicating that the symmetry of the order parameter of BSCCO is not pure *d*-wave. Moreover the superconducting pair wave function amplitude, the Josephson $I_C R_N$ products observed from the local Josephson measurements not only vary over the BSCCO surface on nanometer length scale, but also anticorrelate with the locally measured gap Δ as Δ increases beyond 40 meV. This is an unconventional result because

the amplitude of the superconducting order parameter, $|\Psi|$, $I_C R_N$, Δ and T_C all correlate in the BCS theory.

Our results have been interpreted using the phenomenological model for the phase diagram of the high-T_C superconducting cuprates proposed by Emery and Kivelson (Emery1995). Assuming a connection between hole doping δ_h used in their model and the energy gap Δ which we actually measured, and the local doping inhomogeneity, we showed that $I_C R_N$, the superconducting pair amplitude $|\Psi|$ and T_C became maxima around $\Delta = 40$ meV. Decreases of $I_C R_N$, $|\Psi|$ and T_C with increasing Δ from 40 meV (averaged gap value of optimally-doped BSCCO) are consistent with the phase fluctuation regime of the Emery-Kivelson model. This inverse relation is the central finding of this thesis work. Moreover, the $I_C R_N$ vs. Δ relation showed that $I_C R_N$ also decreases as Δ decreases below 40 meV, indicating that $I_C R_N$, $|\Psi|$, T_C and Δ all correlate. This region is consistent with the amplitude dominated regime of the model (Kimura2008).

A local density of states (LDOS) change of BSCCO due to the high current density of the STM was also observed. The effect of the low R_N measurements (and subsequent high current density) on the BSCCO LDOS was qualitatively studied and it was observed that there was a threshold junction normal state resistance near 30 kΩ below which the irreversible LDOS change occurred. Further investigation is required to study how the Josephson coupling is affected by the high current density as the LDOS of BSCCO is changed as along with the degradation of the surface topography.

Several independent observations of "gap inhomogeneities" raised an interesting question: whether the gap inhomogeneity routinely observed on cleaved surfaces is intrinsic to BSCCO or due to the cleaving. We prepared the BSCCO surface for STM

study by a chemical etching technique as an alternative. This is still an ongoing project and preliminary results were presented in this thesis. It was found that chemical etching removed a degraded surface layer and possibly produced a passivated layer. Surfaces of BSCCO etched by 0.1 % Bromine in methanol showed reproducible dI/dV spectra and this etchant seems to be promising for local Josephson and quasiparticle tunneling measurements.

In parallel with the local Josephson studies of overdoped BSCCO, a new type of STM with a capability of quenched condensed deposition was constructed and is ready to be tested in ultra high vacuum and low temperature condition. Pb/Ag quenched condensed bilayer granular films, which will be studied using this new microscope, have similar phase diagram (T_C vs. film thickness) to that of the high-T_C superconducting cuprates (T_C vs. δ_h). This study will help us understand not only the high-T_C superconducting cuprates but another intriguing subject, the quantum critical point at the superconductor-insulator transition.

This thesis work has demonstrated that the superconducting STM can be a valuable technique to study the high-T_C superconducting cuprates BSCCO and would be a powerful tool to investigate the strongly inhomogeneous system such as the disordered metallic thin film. Findings of this thesis work have deepened our understanding of BSCCO and will help in the formulation of a microscopic underlying theory for the high-T_C superconducting cuprates.

Bibliography

[Onnes1911] H. K. Onnes, Leiden Comm. **120b** (1911).

[Meissner1933] W. Meissner and R. Ochsenfeld, Naturwissenschaften **21**, 787 (1933).

[Ginzburg1950] V. L. Ginzburg and L. D. Landau, Zh. Eksperim. i Teor. Fiz. **20**, 1064 (1950).

[Cooper1956] L. N. Copper, Phys. Rev. **104**, 1189 (1956).

[BCS1957] J. Bardeen, L. N. Copper, and J. R. Schrieffer, Phys. Rev. **108**, 175 (1957).

[Dynes1994] R. C. Dynes, Solid State Commun. **92**, 53 (1994).

[Orenstein2000] J. Orenstein and A. J. Mills, Science **288**, 468 (2000).

[Bednorz1986] G. Bednorz and K. A. Müller, Z. Phys. B **64**, 189 (1986).

[Presland1991] M. R. Presland, J. L. Tallona, R. G. Buckleya, R. S. Liub, and N. E. Flower, Physica C **176**, 95 (1991).

[Wollman1993] D. A. Wollman, D. J. Van Harlingen, W. C. Lee, D. M. Ginsberg, and A. J. Leggett, Phys. Rev. Lett. **71**, 2134 (1993).

[Tsuei1994] C. C. Tsuei, J. R. Kirtley, C. C. Chi, L. S. Yu-Jahnes, A. Gupta, T. Shaw, J. Z. Sun, and M. B. Ketchen, Phys. Rev. Lett. **73**, 593 (1994).

[Monthoux1991] P. Monthoux, A. V. Balatsky, and D. Pines, Phys. Rev. Lett. **67**, 3448 (1991).

[Sun1994a] A. G. Sun, D. A. Gajewski, M. B. Maple, and R. C. Dynes, Phys. Rev. Lett. **72**, 2267 (1994).

[Mößle 1999] M. Mößle and R. Kleiner, Phys. Rev. B **59**, 4486 (1999).

[Valles1991] J. M. Valles, Jr., R. C. Dynes, A. M. Cucolo, M. Gurvitch, L. F. Schneemeyer, J. P. Garno, and J. V. Waszczak, Phys. Rev. B **44**, 11986 (1991).

[Dynes1992] R. C. Dynes, F. Sharifi, and J. M. Valles, Jr., in *Proc. of the Conference. Lattice effects in High-T_C Superconductors*, edited by Y. Bar-Yam, T. Egami, J. Mustre-Leon, and A. R. Bishop (World Scientific, Singapore, 1992), pp. 299-308.

[Ding1996a] H. Ding, M. R. Norman, J. C. Campuzano, M. Randeria, A. F. Bellman, T. Yokoya, T. Takahashi, T. Mochiku, and K. Kadowaki, Phys. Rev. B **54**, R9678 (1996).

[Hardy1993] W. N. Hardy, D. A. Bonn, D. C. Morgan, R. Liang, and K. Zhang, Phys. Rev. Lett. **70**, 3999 (1993).

[Anderson1959] P. W. Anderson, J. Phys. Chem. Solids **11**, 26 (1959).

[Campbell1966] C. K. Campbell, R. C. Dynes, and D. G. Walmsley, Can. J. Phys. **44**, 2601 (1966).

[Radtke1993] R. J. Radtke, K. Levin, H.-B. Schüttler, and M. R. Norman, Phys. Rev. B **48**, 653 (1993).

[Valles1989a] J. M. Valles, Jr., A. E. White, K. T. Short, R. C. Dynes, J. P. Garno, A. F. J. Levi, M. Anzlowar, and K. Baldwin, Phys. Rev. B **39**, 11599 (1989).

[Sun1994b] A. G. Sun, L. M. Paulius, D. A. Gajewski, M. B. Maple, and R. C. Dynes, Phys. Rev. B **50**, 3266 (1994).

[Yazdani1999] A. Yazdani, C. M. Howald, C. P. Lutz, A. Kapitulnik, and D. M. Eigler, Phys. Rev. Lett. **83**, 176 (1999).

[Hudson1999] E. W. Hudson, S. H. Pan, A. K. Gupta, K.-W. Ng, and J. C. Davis, Science **285**, 88 (1999).

[Pan2000a] S. H. Pan, E. W. Hudson, K. M. Lang, H. Eisaki, S. Uchida, and J. C. Davis, Nature (London) **403**, 746 (2000).

[Ding1996b] H. Ding, J. C. Yokoya, T.and Campuzano, T. Takahashi, M. Randeria, M. R. Norman, T. Mochiku, K. Kadowaki, and J. Giapintzakis, Nature (London) **382**, 51 (1996).

[Renner1998a] C. Renner, B. Revaz, J.-Y. Genoud, K. Kadowaki, and Ø. Fischer, Phys. Rev. Lett. **80**, 149 (1998).

[Tallon2001] J. L. Tallon and J. W. Loram, Physica C **349**, 53 (2001).

[Hüfner2008] S. Hüfner, M. A. Hossain, A. Damascelli, and G. A. Sawatzky, Rep. Prog. Phys. **71**, 062501 (2008).

[Lee2007] W. S. Lee, I. M. Vishik, K. Tanaka, D. H. Lu, T. Sasagawa, N. Nagaosa, T. P. Devereaux, Z. Hussain, and Z.-X. Shen, Nature (London) **450**, 81 (2007).

[Pan2001] S. H. Pan, J. P. O'Neal, R. L. Badzey, C. Chamon, H. Ding, J. R. Engelbrecht, Z. Wang, H. Eisaki, S. Uchida, A. K. Gupta, et al., Nature (London) **413**, 282 (2001).

[Howald2001] C. Howald, P. Fournier, and A. Kapitulnik, Phys. Rev. B **64**, 100504(R) (2001).

[Lang2002] K. M. Lang, V. Madhavan, J. E. Hoffman, E. W. Hudson, H. Eisaki, S. Uchida, and J. C. Davis, Nature (London) **415**, 412 (2002).

[Dynes1978a] R. C. Dynes, J. P. Garno, and J. M. Rowell, Phys. Rev. Lett. **40**, 479 (1978).

[Goldman1998] A. M. Goldman and N. Marković, Physics Today **51**, 39 (1998).

[Valles1989b] J. M. Valles, Jr., R. C. Dynes, and J. P. Garno, Phys. Rev. B **40**, 6680 (1989).

[Valles1992] J. M. Valles, Jr., R. C. Dynes, and J. P. Garno, Phys. Rev. Lett. **69**, 3567 (1992).

[Barber1994] R. P. Barber, Jr., L. M. Merchant, A. La Porta, and R. C. Dynes, Phys. Rev. B **49**, 3409 (1994).

[Cooper1961] L. N. Cooper, Phys. Rev. Lett. **6**, 689 (1961).

[Merchant2001] L. Merchant, J. Ostrick, R. P. Barber, Jr., and R. C. Dynes, Phys. Rev. B **63**, 134508 (2001).

[Deutscher1969] G. Deutscher and P. G. de Gennes, *Superconductivity*, edited by R. D. Parks (Marcell Dekker, New York, 1969).

[Binnig1982] G. Binnig, H. Rohrer, C. Gerber, and E. Weibel, Appl. Phys. Lett. **40**, 178 (1982).

[Binnig1983] G. Binnig, H. Rohrer, C. Gerber, and E. Weibel, Phys. Rev. Lett. **50**, 120 (1983).

[Eigler1990] D. M. Eigler and E. K. Schweizer, Nature (London) **344**, 524 (1990).

[Crommie1993a] M. F. Crommie, C. P. Lutz, and D. M. Eigler, Nature (London) **363**, 524 (1993).

[Crommie1993b] M. F. Crommie, C. P. Lutz, and D. M. Eigler, Science **262**, 218 (1993).

[Hess1989] H. F. Hess, R. B. Robinson, R. C. Dynes, J. M. Valles, Jr., and J. V. Waszczak, Phys. Rev. Lett. **62**, 214 (1989).

[Hess1990a] H. F. Hess, R. B. Robinson, and J. V. Waszczak, Phys. Rev. Lett. **64**, 2711 (1990).

[Maggio-Aprile1995] I. Maggio-Aprile, C. Renner, A. Erb, E. Walker, and Ø. Fischer, Phys. Rev. Lett. **75**, 2754 (1995).

[Renner1998b] C. Renner, B. Revaz, K. Kadowaki, I. Maggio-Aprile, and Ø. Fischer, Phys. Rev. Lett. **80**, 3606 (1998).

[Pan2000b] S. H. Pan, E. W. Hudson, A. K. Gupta, K.-W. Ng, H. Eisaki, S. Uchida, and J. C. Davis, Phys. Rev. Lett. **85**, 1536 (2000).

[Cren2000] T. Cren, D. Roditchev, W. Sacks, J. Klein, J.-B. Moussy, C. Deville-Cavellin, and M. Laguës, Phys. Rev. Lett. **84**, 147 (2000).

[Hoffman2002b] J. E. Hoffman, K. McElroy, D.-H. Lee, K. M. Lang, H. Eisaki, S. Uchida, and J. C. Davis, Science **297**, 1148 (2002).

[Howald2003] C. Howald, H. Eisaki, N. Kaneko, M. Greven, and A. Kapitulnik, Phys. Rev. B **67**, 014533 (2003).

[Hoffman2002a] J. E. Hoffman, E. W. Hudson, K. M. Lang, V. Madhavan, H. Eisaki, S. Uchida, and J. C. Davis, Science **295**, 466 (2002).

[Vershinin2004] M. Vershinin, S. Misra, S. Ono, Y. Abe, Y. Ando, and A. Yazdani, Science **303**, 1995 (2004).

[Gomes2007] K. K. Gomes, A. N. Pasupathy, A. Pushp, S. Ono, Y. Ando, and A. Yazdani, Nature (London) **447**, 569 (2007).

[Pasupathy2008] A. N. Pasupathy, A. Pushp, K. K. Gomes, C. V. Parker, J. Wen, Z. Xu, G. Gu, S. Ono, Y. Ando, and A. Yazdani, Science **320**, 196 (2008).

[Alldredge2008] J. W. Alldredge, J. Lee, K. McElroy, M. Wang, K. Fujita, Y. Kohsaka, C. Taylor, H. Eisaki, S. Uchida, P. J. Hirschfeld, *et al.*, Nature Phys. **4**, 319 (2008).

[McElroy2005a] K. McElroy, D.-H. Lee, J. E. Hoffman, K. M. Lang, J. Lee, E. W. Hudson, H. Eisaki, S. Uchida, and J. C. Davis, Phys. Rev. Lett. **94**, 197005 (2005).

[Josephson1962] B. D. Josephson, Phys. Lett. **1**, 251 (1962).

[Naaman2001b] O. Naaman, W. Teizer, and R. C. Dynes, Phys. Rev. Lett. **87**, 097004 (2001).

[Naaman2003] O. Naaman, R. C. Dynes, and E. Bucher, Int. J. Mod. Phys. B **17**, 3569 (2003).

[Kawayama1999] I. Kawayama, M. Kanai, M. Maruyama, A. Fujimaki, and H. Hayakawa, Physica C **325**, 49 (1999).

[Emery1995] V. J. Emery and S. A. Kivelson, Nature (London) **374**, 434 (1995).

[Esaki1969] L. Esaki, in *Tunneling Phenomena in Solids*, edited by E. Burstein and S. Lundqvist (Plenum, New York, 1969).

[Giaever1969] I. Giaever, in *Tunneling Phenomena in Solids*, edited by E. Burstein and S. Lundqvist (Plenum, New York, 1969).

[Chen Book] C. J. Chen, *Introduction to Scanning Tunneling Microscopy* (Oxford University Press, New York, 1993).

[Bardeen1961] J. Bardeen, Phys. Rev. Lett. **6**, 57 (1961).

[Cohen1962] M. H. Cohen, L. M. Falicov, and J. C. Phillips, Phys. Rev. Lett. **8**, 316 (1962).

[Kane1969] E. O. Kane, in *Tunneling Phenomena in Solids*, edited by E. Burstein and S. Lundqvist (Plenum, New York, 1969).

[Tinkham Book] M. Tinkham, *Introduction to Superconductivity* (McGraw-Hill, New York, 1996), 2nd ed.

[Dynes1978b] R. C. Dynes, V. Narayanamurti, and J. P. Garno, Phys. Rev. Lett. **41**, 1509 (1978).

[Giaever1962] I. Giaever, H. R. Hart, and K. Megerle, Phys. Rev. **126**, 941 (1962).

[Lee2006] J. Lee, K. Fujita, K. McElroy, J. A. Slezak, M. Wang, Y. Aiura, H. Bando, M. Ishikado, T. Masui, J.-X. Zhu, *et al.*, Nature (London) **442**, 546 (2006).

[Niestemski2007] F. C. Niestemski, S. Kunwar, S. Zhou, S. Li, H. Ding, Z. Wang, P. Dai, and V. Madhavan, Nature (London) **450**, 1058 (2007).

[Pilgram2006] S. Pilgram, T. M. Rice, and M. Sigrist, Phys. Rev. Lett. **97**, 117003 (2006).

[Scalapino2006] D. J. Scalapino, Nature Phys. **2**, 593 (2006).

[Meservey1988] R. Meservey, Physica Scripta **38**, 272 (1988).

[Pan1998] S. H. Pan, E. W. Hudson, and J. C. Davis, Appl. Phys. Lett. **73**, 2992 (1998).

[Naaman2001a] O. Naaman, W. Teizer, and R. C. Dynes, Rev. Sci. Instrum. **72**, 1688 (2001).

[Anderson1964] P. W. Anderson, in *Lectures on the Many-Body Problem, Ravello 1963, Vol. II*, edited by E. R. Caianello (Academic Press, New York, 1964), pp. 113-135.

[Anderson1967] P. W. Anderson, in *Progress in Low Temperature Physics, Vol. 5*, edited by C. J. Gorter (North-Holland Publishing Co., Amsterdam, 1967).

[Scalapino1969] D. J. Scalapino, *Tunneling Phenomena in Solids*, edited by E. Burstein and S. Lundqvist (Plenum, New York, 1969).

[Scott1969] A. C. Scott, Am. J. Phys. **37**, 52 (1969).

[Fulton1971] T. A. Fulton and R. C. Dynes, Solid State Commun. **9**, 1069 (1971).

[Stewart1968] W. C. Stewart, Appl. Phys. Lett. **12**, 277 (1968).

[McCumber1968] D. E. McCumber, J. Appl. Phys. **39**, 3113 (1968).

[Van Duzer Book] T. Van Duzer and C. W. Turner, *Principles of Superconductive Devices and Circuits* (Prentice Hall, N. J., 1999), 2nd ed.

[Ivanchenko1968] Y. M. Ivanchenko and L. A. Zil'berman, Zh. Ezperim. i Teor. Fiz. **55**, 2395 (1968), [Sov. Phys. JETP **28**, 1272 (1969)].

[Ingold1994] G.-L. Ingold, H. Grabert, and U. Eberhardt, Phys. Rev. B **50**, 395 (1994).

[Harada1996] Y. Harada, H. Takayanagi, and A. A. Odintsov, Phys. Rev. B **54**, 6608 (1996).

[Ono1987] R. Ono, M. Cromar, R. Kautz, R. Soulen, J. Colwell, and W. Fogle, IEEE Trans. Magn. **MAG-23**, 1670 (1987).

[Martinis1989] J. Martinis and R. Kautz, Phys. Rev. Lett. **63**, 1507 (1989).

[Kautz1990] R. Kautz and J. Martinis, Phys. Rev. B **42**, 9903 (1990).

[Ingold1992] G.-L. Ingold and Yu. V. Nazarov, in *Single Charge Tunneling*, edited by H. Grabert and M. Devoret (Plenum, New York, 1992).

[Naaman thesis] O. Naaman, Ph.D. thesis, University of California, San Diego (2003).

[Devoret1990] M. Devoret, D. Esteve, H. Grabert, G.-L. Ingold, H. Pothier, and C. Urbina, Phys. Rev. Lett. **64**, 1824 (1990).

[Fulton1968] T. A. Fulton and D. E. McCumber, Phys. Rev. **175**, 585 (1968).

[Naaman2004] O. Naaman and R. C. Dynes, Solid State Commun. **129**, 299 (2004).

[Hess1991] H. F. Hess, R. B. Robinson, and J. V. Waszczak, Physica B **169**, 422 (1991).

[Yokoya2001] T. Yokoya, T. Kiss, A. Chainani, S. Shin, M. Nohara, and H. Takagi, Science **294**, 2518 (2001).

[Annett1990] J. F. Annett, N. Goldenfeld, and S. R. Renn, in *Physical Properties of High Temperature Superconductors II*, edited by D. M. Ginsberg (World Scientific, Teaneck, NJ, 1990).

[Martinis1987] J. M. Martinis, M. H. Devoret, and J. Clarke, Phys. Rev. B **35**, 4682 (1987).

[Ono2003] S. Ono and Y. Ando, Phys. Rev. B **67**, 104512 (2003).

[Fischer2007] Ø. Fischer, M. Kugler, I. Maggio-Aprile, C. Berthod, and C. Renner, Rev. Mod. Phys. **79**, 353 (2007).

[Kimura2008] H. Kimura, R. P. Barber, Jr., S. Ono, Y. Ando, and R. C. Dynes, Phys. Rev. Lett. **101**, 037002 (2008).

[Wise2009] W. D. Wise, M. C. Boyer, K. Chatterjee, T. Kondo, T. Takeuchi, H. Ikuta, Y. Wang, and E. W. Hudson, Nature Phys. **5**, 213 (2009).

[Boyer2007] M. C. Boyer, W. D. Wise, K. Chatterjee, M. Yi, T. Kondo, T. Takeuchi, H. Ikuta, and E. W. Hudson, Nature Phys. **3**, 802 (2007).

[Vasquez1988] R. P. Vasquez, B. D. Hunt, and M. C. Foote, Appl. Phys. Lett. **53**, 2692 (1988).

[Gurvitch1989] M. Gurvitch, J. M. Valles, Jr., A. M. Cucolo, R. C. Dynes, J. P. Garno, L. F. Schneemeyer, and J. V. Waszczak, Phys. Rev. Lett. **63**, 1008 (1989).

[Sun1996] A. G. Sun, A. Truscott, A. S. Katz, and R. C. Dynes, Phys. Rev. B **54**, 6734 (1996).

[Truscott thesis] A. Truscott, Ph.D. thesis, University of California, San Diego (1999).

[Truscott1999] A. D. Truscott, R. C. Dynes, and L. F. Schneemeyer, Phys. Rev. Lett. **83**, 1014 (1999).

[Sharoni2004] A. Sharoni, I. Asulin, G. Koren, and O. Millo, Phys. Rev. Lett. **92**, 017003 (2004).

[Smoluchowski1941] R. Smoluchowski, Phys. Rev. **60**, 661 (1941).

[Lang1971] N. D. Lang and W. Kohn, Phys. Rev. B **3**, 1215 (1971).

[Besocke1977] K. Besocke, B. Krahl-Urban, and H. Wagner, Surface Science **68**, 39 (1977).

[Ekinci1999] K. L. Ekinci and J. M. Valles, Jr., Phys. Rev. Lett. **82**, 1518 (1999).

[Stewart2007] M. D. Stewart, Jr., A. Yin, J. M. Xu, and J. M. Valles, Jr., Science **318**, 1273 (2007).